UCRL-19533
c.2

WEAK INTERACTION STUDIES BY NUCLEAR ORIENTATION

William D. Brewer
(Ph. D. Thesis)

December 1969

AEC Contract No. W-7405-eng-48

LAWRENCE RADIATION LABORATORY
UNIVERSITY of CALIFORNIA BERKELEY

UCRL-19533
c.2

DISCLAIMER

UNIVERSITY OF CALIFORNIA

Lawrence Radiation Laboratory
Berkeley, California 94720

AEC Contract No. W-7405-eng-48

WEAK INTERACTION STUDIES BY NUCLEAR ORIENTATION

William D. Brewer

(Ph.D. Thesis)

December 1969

Weak Interaction Studies by Nuclear Orientation

By

William Dean Brewer

A.B. (University of Oregon) 1965

DISSERTATION

Submitted in partial satisfaction of the requirements for the degree of

DOCTOR OF PHILOSOPHY

in

Chemistry

in the

GRADUATE DIVISION

of the

UNIVERSITY OF CALIFORNIA, BERKELEY

Approved:

David R. Shirley

Norman F. Ramsey

Burton J. Moyer

Committee in Charge

Degree conferred.....

Date

TABLE OF CONTENTS

LIST OF FIGURES

WEAK INTERACTION STUDIES BY NUCLEAR ORIENTATION

William D. Brewer

Department of Chemistry
and
Lawrence Radiation Laboratory
University of California
Berkeley, California 94720

December 1969

ABSTRACT

The technique of low temperature nuclear orientation has been applied to two problems involving weak nuclear decays. Nuclei of ^{119}Sb were polarized in an iron lattice and the angular distribution of inner bremsstrahlung photons emitted during the electron capture decay was observed. The distribution fit the correlation function

$$W(\theta) = 1 + A_1 G_1 P_1(\cos \theta)$$

and the asymmetry coefficient had the theoretical value of +1.0 near the spectrum endpoint. However, some energy dependence of A_1 was observed, in contrast to theoretical expectations. Possible origins of the energy dependence are discussed. Nuclear orientation was also carried out with three isotopes which undergo 1st forbidden beta decays: ^{186}Re, ^{188}Re, and ^{194}Ir. The source nuclei were polarized in iron lattices and the angular distributions of both beta particles and gamma rays were observed. Lithium-drifted germanium counters were used to detect the beta particles. The beta particle angular distribution coefficients A_1 and A_2 are reported as functions of energy. The results are in general agreement with those of previous workers, although the experimental errors have been considerably reduced. The attenuation of the gamma ray anisotropies gives a measure of the relative size of the $\int B_{ij}$ matrix element in the preceeding $1^- \rightarrow 2^+$ beta decays and values for this attenuation are reported. The $\int B_{ij}$ matrix element was found to make a finite contribution in the decays of the two Re isotopes, but to be zero in the ^{194} Ir decay. The combined data may be used to determine the nuclear matrix elements entering the decays and to test the Conserved Vector Current hypothesis of weak interactions.

INTRODUCTION

Weak Interactions

In the present view of physiscs, the interactions which determine the transformations of matter and energy may be divided into four classes, according to their relative strengths:

1) Strong interactions, relative strength 10, which provide the nuclear binding force and cause certain elementary particle interactions. They are propagated by virtual pion exchange.

2) Electromagnetic interactions, relative strength 10^{-2}, which give rise to electric and magnetic forces, e.g. the binding of atomic electrons. They are propagated by virtual photon exchange.

3) Weak interactions, of relative strength 10^{-14}, which bring about a great variety of decays, among them nuclear $\beta^{\pm}$ and electron capture decays. They are thought to be propagated by the exchange of a virtual intermediate vector boson, although this particle has never been observed.

4) Gravitational interactions, which cause the gravitational attraction of matter. Relative strength 10^{-44}.

Unquestionably the best understood of the four is the electromagnetic interaction, which can be described rather completely by quantum electrodynamics. In contrast, the theoretical description of the gravitational interaction has yet to be accomplished. The strong and weak interactions are intermediate cases in current theoretical understanding, although considerable progress has been made in the general description

of the weak interaction in the past fifteen years, and the study of nuclear weak decays has contributed greatly to this advance. Some gaps in experimental confirmation have remained, however, and the following work is a contribution toward filling two of them, relating to the inner bremsstrahlung (IB) and the conserved vector current (CVC) hypothesis.

The IB is a weak continuous photon spectrum which accompanies beta and electron capture decays. (In general, bremsstrahlung accompanies any process in which charges are accelerated.) It results from a perturbation on the usual beta-decay interaction by the electromagnetic interaction. The IB was first described theoretically 30 years ago by Bloch [1], by Konopinski and Uhlenbeck [2], and by Morrison and Schiff [3]; several more recent papers have dealt with the subject in the light of parity non-conservation by weak interactions. Considerable work has been done on shapes and intensities of IB spectra, and some experiments on the circular polarization of IB accompanying beta decays have been performed [4], but the electron-capture IB has been neglected and no observations of IB from polarized nuclei have previously been reported. The first section of this thesis deals with an experiment on the IB accompanying the electron capture decay of polarized ^{119}Sb nuclei.

The CVC hypothesis was put forth in 1958 by R.P. Feynman and M. Gell-Mann.[5] It deals with the relation between the weak and electromagnetic interactions in the presence of strong interactions: since the nucleons involved in a nuclear weak decay are also subject to strong interactions, the properties of the weak decay might be expected to be

affected by the strong forces. According to the current-current formulation of weak interaction theory, the weak decay arises from the interaction of two currents,which in the case of nuclear weak decays are the lepton current due to the electron and neutrino, and the nucleon current. The lepton current can be explicitly given, but the nucleon current (or any current involving hadrons, or strongly interacting particles or states) contains undetermined form factors because the strong interaction is not well understood. In the weak interaction there are two types of current operators, which transform as vectors and as axial vectors. The corresponding currents are called the vector and axial vector currents.The CVC hypothesis states that the form factor for the vector current is unchanged in magnitude (unrenormalized) by the strong interaction. The hypothesis is supported by the analogy with electromagnetic theory: the isovector part of the electromagnetic current is also unrenormalized by the strong interaction. (As a consequence, the electric charge is unchanged in magnitude by strong interactions; e.g. the proton has the same magnitude charge as the electron.) Physically, CVC has several consequences and thus may be tested experimentally. Perhaps the most obvious test is to compare the interaction strength determined from a nonhadronic decay (muon beta decay) with that obtained from a purely vector hadronic decay (a $0^+ \rightarrow 0^+$ nuclear beta decay.) However, a number of corrections (finite nuclear size and screening corrections; radiative corrections; Coulomb distortion of nuclear wave functions) must be applied to the measured $0^+ \rightarrow 0^+$ transition rates before they can be compared with the muon decay rate and this reduces the accuracy of such a comparison.

A second experimental test of CVC was suggested by Gell-Mann. CVC implies that the isovector electromagnetic current between nucleon states, the vector weak current for neutron-β^- decay, and the vector current for proton-β^+ decay are the components of an "isobaric spin triplet" (they contain the three components of the isobaric spin operator τ_z, τ_+, and τ_- respectively); thus the form-factors in the weak currents are related to those in the electromagnetic current. This can be tested in the decays of the isospin triplet ^{12}B-$^{12}C^*$ (15.1 mev) -^{12}N. The three isotopes decay by β^-, γ, and β^+ emission to the ^{12}C ground state. The β decays are axial-vector to the first order but the vector current enters in 2nd forbidden corrections which affect the β-spectrum shapes. The size of the correction is related to the radiation width of the γ transition. Experimental results on the β spectra are in agreement with the CVC predictions. A similar situation exists at mass 8, and experiments on β-α angular correlations following the decays of ^8Li and ^8B are also in agreement with CVC. Also at mass 24 there is a usable isospin triplet in which $\beta^\pm$- γ correlations have been measured.

A third physical consequence of CVC is the existence of pion-pion weak decays. As mentioned previously, the strong interaction is believed to be mediated by virtual-pion exchange. A strongly-interacting particle such as a neutron is thus not a simple particle but consists of a core which at least some of the time is surrounded by a pion cloud. If the weak interaction strength for such a particle is the same as for a simple particle with no pion cloud, it must be that the pions also have the same weak-interaction strength as the bare nucleons; therefore purely

pionic weak decay (as oposed to pion-muon and pion-electron decays) should occur. Measurements of the branching ratio for pion-pion decay have yielded values within the range of the CVC prediction although the non-CVC theory is not excluded.[6] In general the experiments listed above have supported CVC but have not conclusively extablished it; they are in most cases difficult to perform and subject to various corrections and theoretical assumptions. In particular the comparison between the muon decay amplitude and that for vector nuclear decays shows a small discrepancy, which may, however, be due to the interference of the strangeness-changing current in the nuclear decays (Cabibbo hypothesis.)

There is an additional experimental consequence of CVC. This is that the relationships between certain nuclear matrix elements in forbidden beta decays may be altered from their values in the conventional theory.[24-28] In particular, the ratio of matrix elements $\int\alpha$ and $\int\chi$ is predicted by CVC. It is desirable to test this prediction not only as an additional check of CVC (which is reasonably well established by the experiments mentioned above), but also to establish the validity of the relationships between matrix elements, which can then be used to evaluate the matrix elements in complex decays. Eventual understanding of the nuclear force will undoubtedly depend on detailed experimental information on various nuclear matrix elements, and nuclear beta decay has the potential of being a powerful tool for acquiring this information.

In first forbidden beta decay, six matrix elements can in principle occur. (See Chap. II.) In decays of the type 2- →2+ all six are potentially allowed; however, matrix elements which are multiplied by the

coefficient $\xi(=\alpha Z/2R$, electron's Coulomb energy at the nuclear surface) dominate in these transitions, with the result that the relativistic and B_{ij} (tensor rank two) terms are suppressed and observable quantities have allowed behavior. Thus only the ratio of tensor rank zero and rank one terms can be determined. In $3^- \rightarrow 2^+$ transitions only the rank one and two matrix elements are allowed, and often the B_{ij} term seems to dominate (because of nuclear-state selection rules), so again, measurement of the other matrix elements is precluded. In $1^- \rightarrow 2^+$ transitions the same matrix elements are allowed and here no particular terms predominate in some cases. These transitions may be studied by β-γ angular correlations, β polarization and spectrum shape measurements, or by β- nuclear angular distribution measurements using polarized nuclei. The $1^- \rightarrow 0^+$ transitions are even simpler, lacking the B_{ij} matrix elements. They cannot, however, be studied by β-γ correlation techniques when the 0^+ state is the ground state in the daughter nucleus, as is often the case. In the second part of this thesis, measurements of β- nuclear angular distributions using polarized nuclei are described for the decays of ^{186}Re, ^{188}Re, and ^{194}Ir. All these nuclei exhibit transitions of both the last two types mentioned above--$1^- \rightarrow 2^+$ and $1^- \rightarrow 0^+$--and the first two have been studied previously by several workers by all of the above methods.[7,43-50] It is hoped that the present work will complement and perhaps improve upon the earlier results. As for ^{194}Ir, its decay has been studied only by spectrum shape measurements[51] and β-γ angular correlations,[52] and the present work will provide new information on this decay.

Nuclear Orientation

As the name implies, nuclear orientation is a means of determining the direction of a nucleus or assembly of nuclei, as defined by the nuclear spin $\vec{I}$, relative to some axis fixed in space. (Equivalently, one may select nuclei having a particular value of the magnetic quantum number M_I.) An assembly of oriented nuclei may be used to measure the directional correlation between the nucleus and an emitted radiation; or, conversely, one may use the angular distribution of the radiation and knowledge of the directional correlation to measure the degree of nuclear orientation and thereby gain information about the nuclear environment which produced orientation. The technique is thus useful in solid state physics and chemistry as well as in nuclear physics, although in the present work only the latter application is employed.

A number of techniques for achieving nuclear orientation have been developed in the past 20 years. In general these techniques fall into two classes: dynamic (steady-state) and static (equilibrium). In the former methods, energy is continuously fed into an assembly of atoms in order to maintain a non-equilibrium distribution of magnetic substate populations, as in optical and microwave pumping techniques, while the nuclei become oriented via the hyperfine interaction. Static methods, which were employed in the work to be described below, make use of low temperatures to produce thermal equilibrium population differences among nuclear magnetic substates.

Two types of nuclear orientation may be distinguished: alignment, in which the nuclei are arranged symmetrically with respect to a quanti-

zation axis (i.e. the substates denoted by $+M_I$ and $-M_I$ have equal populations); and polarization, in which an asymmetric distribution of populations is obtained. In order to produce energy splittings between the substates, a nuclear moment must interact with a field or charge distribution. Since the nuclear moments are rather small in magnitude, the energy splittings are typically of order 10^{-18} ergs, corresponding to about 10^{-2} °K., and thus the temperatures required to produce substantial population differences between the substates are very low. In practice only the magnetic dipole and electric quadrupole moments are large enough to be of use. (The electric monopole [charge Z] is symmetrical with respect to $\vec{I}$ and is therefore unable to produce energy splittings between M_I substates.)Magnetic fields of sufficient strength may be applied directly to the sample from an external magnet or may be hyperfine fields in paramagnetic or ferromagnetic crystals or in ferromagnetic host lattices or lattices in which a localized moment is present on the atoms of interest. For quadrupole alignment the electric field gradients in certain crystalline solids are employed.

In addition to the static and dynamic methods for producing nuclear orientation, techniques for selecting nuclei in particular substates such as angular correlation of successive nuclear radiations and Mössbauer effect are available and may yield similar information. Nuclear orientation may also be obtained as a result of a nuclear reaction or scattering process.

Production of low temperatures remains a major obstacle to the use of thermal equilibrium nuclear orientation. Recently several ingeneous

methods have been introduced, including ^{3}He-^{4}He dilution cooling, adiabatic compression of ^{3}He (Pomeranchuk effect), and rotational cooling of anisotropic crystals. The oldest and probably still the most generally applicable method, however, is adiabatic demagnetization of paramagnetic salts. Using this technique, one can cool a sample of ferromagnetic metal in contact with the paramagnetic salt to perhaps 4 mdeg. K. Since the nuclei of most atoms dissolved in a ferromagnetic lattice experience large hyperfine fields, nuclear orientation can be obtained with almost any nucleus having nonzero spin and moment. This is the so-called universal method of nuclear orientation and was first employed by Samoilov in 1959.[8]

Basically, the work to be described below consists of the application of the universal method -- which yields nuclear polarization -- to the two aspects of weak interactions previously discussed. The first two chapters contain brief outlines of the theory of nuclear orientation and of weak interactions as applicable to the present experiments. Following this in chapters III and VI are descriptions of the apparatus used -- cryostats, radiation detectors, magnets, and so forth -- for the IB and CVC experiments, respectively. In chapters IV and VII are detailed descriptions of the two sets of experiments, respectively, including source preparations, assembly and cooling of the apparatus, thermometry, data collection, and analysis of the data. Finally in chapters V and VIII are discussions of the conclusions drawn from the experiments and critiques of the experimental methods.

CHAPTER I

Nuclear Orientation Theory

As mentioned in the Introduction, there are three requirements for nuclear orientation by the universal method:

1) A nucleus with a sufficiently large magnetic dipole moment (ca. 1 nm.).

2) A reasonably large hyperfine field on the nucleus in the ferromagnetic host metal (ca. 100 koe.).

3) Temperatures low enough that the thermal energy is the same order as the magnetic interaction energy resulting from 1) and 2).

The hyperfine field in ferromagnets is assumed to arise through a hyperfine interaction of the form $A(\underset{\sim}{I}\cdot\underset{\sim}{S})$ where I is the nuclear spin and $\underset{\sim}{S}$ is an electronic spin vector. Since this is a contact interaction, the electrons producing $\underset{\sim}{S}$ must have a finite probability density within the nucleus; i.e. they must be s (or possibly d) electrons. The spin polarization giving rise to $\underset{\sim}{S}$ may arise by direct interaction of s or d conduction electrons with the exchange field in the ferromagnetic host (conduction electron polarization); or it may result from a secondary exchange between the core s electrons and polarized d electrons (core polarization.) The former mechanism produces a hf field parallel to the exchange field, while the latter may give an antiparallel hf field. A recent tabulation[9] shows hf fields of order 100 koe. for 45 elements in common ferromagnetic metals and others remain to be measured, so satisfying condition 2) is not difficult.

Given conditions 1) and 2), a magnetic interaction energy of the

form $E = -\underset{\sim}{\mu}\cdot\underset{\sim}{H}_{hf}$ will result. Specifically, the nuclear level with spin I will split into 2I+1 magnetic substates labeled by the magnetic quantum number M_I and having interaction energies $E_M = -\mu_n \beta_n H_{hf} M_I / I$ where μ is the magnetic moment of the level in nuclear magnetons, and β_n is the nuclear magneton. We assume thermal equilibrium between the nuclei and the host lattice. (This requires that the nuclear spin-lattice relaxation rate $\propto 1/T_1$ is large compared to the rate of change of the lattice temperature. Typical values[10] of $1/T_1$ are of the order of $10^{-1}\,\mathrm{sec}^{-1}$ while sample temperatures change at rates of ~ 1 mdeg./hr., so equilibrium is a good assumption.) In thermal equilibrium, the relative populations of the magnetic substates are given by a Boltzmann distribution:

$$\text{Eq. 1} \qquad a_M \propto \frac{\exp\,[-E_M/kT]}{\sum_M \exp[-E_M/kT]} \qquad -I \leq M \leq I$$

where a_M is the population of state M and k is the Boltzmann constant. For nuclear orientation, a_M must be a strong function of M, so that $\beta = E_M/kT$ should be of order 1. This is condition 3).

Assuming the above three conditions are satisfied, one requires a description of the nuclear orientation in terms of a variable which can be observed in the laboratory. The observable usually employed is the angular distribution of a nuclear radiation relative to an axis fixed in the laboratory. (If a hamiltonian of the form $A(\underset{\sim}{I}\cdot\underset{\sim}{S})$ is obeyed, the nuclear orientation has axial symmetry around the direction defined by $\underset{\sim}{S}$, so a single quantization axis suffices to define the distribution.)

The problem may be divided into three parts: the description of the directional correlation between the nucleus $\underset{\sim}{I}$ and the quantization axis $\underset{\sim}{z}$; description of the correlation between the radiation propagation vector $\underset{\sim}{k}$ and the nuclear axis $\underset{\sim}{I}$; and geometrical considerations relating the radiation detector placement to $\underset{\sim}{k}$. These correlations have been worked out in detail by several authors[11,12] and the derivations will not be repeated here. The resulting correlation function $W(\theta)$, giving the relative radiation intensity to be observed by a detector at angle θ to the $\underset{\sim}{z}$ axis, has the following form:

$$\text{Eq. 2} \qquad W(\theta) = 1 + \sum_{k} B_k U_k b_k F_k Q_k P_k (\cos\theta).$$

Here the index k runs from 1 to $\min.\{2I_0, 2L\}$ where I_0 is the smallest nuclear spin preceeding the observed transition and L is the angular momentum of the radiation observed; the B_k are spherical tensors of rank k (diagonal components only for axial symmetry) which describe the $\underset{\sim}{I}$ - $\underset{\sim}{z}$ correlation (they are functions of μ_n, H_{hf}, and T); the U_k are reorientation parameters which modify the B_k to allow for reorientation effects during nuclear transitions preceeding the observed one; the b_k and F_k are angular momentum coefficients giving the correlation between $\underset{\sim}{k}$ and $\underset{\sim}{I}$ (the b_k are all 1 for gamma radiation but usually differ from 1 for particles); and the Q_k and P_k are geometrical factors, Q_k giving the correction for the fact that usable radiation detectors subtend a finite solid angle around θ, and P_k being Legendre polynomials of rank k (spherical harmonics Y_k^m in the general case of non-axial symmetry.) If the observed

radiation arises from a parity conserving interaction (strong or EM interaction) only the even values of k appear in the sum. No correction for change in nuclear orientation during the lifetime of the intermediate state, if any, was included here, since the intermediate state lifetimes are usually less than 10^{-3} sec. and therefore much shorter than nuclear spin-lattice relaxation times in ferromagnetic metals.

The functions B_k have been tabulated as functions of I and $\beta = E_M/kT$.[11] The U_k's are just Racah coefficients with a special normalization.[11] The F_k's are tabulated functions of I_i, I_f, and L, and the b_k's have been given by various authors for particular cases.[12] The Q_k's are tabulated for on-axis scintillation counters[13] and may be calculated for other cases.[14] Thus if the hf field, nuclear moment, temperature, decay scheme, and particle parameters b_k are fixed, the correlation function $W(\theta)$ is completely determined; measurement of $W(\theta)$ allows investigation of one or more of these items if some of the others are known.

Weak Interaction Theory

The hamiltonian energy density for the electromagnetic interaction may be represented in four-vector notation as

$$h_\gamma = \sum_\alpha -j_\alpha \cdot A_\alpha / c \qquad \alpha = 1,4$$

where j_α is the charge-current density given by $\bar{\Psi}\gamma_\alpha\Psi$, γ_α being the four Dirac matrices;* and A_α is the four-vector potential of the electromagnetic field.[15] The weak interaction can be analogously described by

Eq. 3 $$h_\beta = \frac{G}{\sqrt{2}} \sum_\alpha J_\alpha \cdot J_\alpha^\dagger \qquad \alpha = 1,4$$

where G is the weak interaction constant and J_α is the weak four-vector current.** The current J_α is the sum of terms $\bar{\Psi}O_\alpha\Psi$ which are of four types: the electron-neutrino current, the muon-neutrino current, the baryon-baryon strangeness conserving current, and the baryon-baryon strangeness changing current. Thus h_β has sixteen terms. The diagonal terms are self-current processes such as electron-neutrino scattering and the nucleon-nucleon weak interaction which is presumed to give rise to parity impurities in nuclear states. The twelve cross terms describe processes such as muon decay, nuclear beta decay, nuclear muon capture, and various strangeness-changing processes including kaon and lambda decays. There are actually only six unique cross terms, since the others describe inverse processes (e.g. negatron decay vs. positron decay).

Only nuclear beta decay is of interest here, and it will be considered in more detail. Nuclear beta decay arises from the interaction of the nucleon-nucleon current with the electron-neutrino current ("lepton

---

* See Appendix II for definitions of Dirac matrices.

** The universal current-current interaction was suggested by Feynman and Gell-Mann,[5] although it is similar in form to the original interaction given by Fermi.[16]

field"). The completely general beta-decay interaction may be represented as follows:

$$\text{Eq. 4} \qquad h_\beta = \frac{G}{\sqrt{2}} \sum_{i,j} C_i (\bar{\psi}_{p_j} O_i^j \psi_{n_j}) \cdot \{ (\bar{\psi}_e [O_i \, D(I+\gamma_5)/2] \psi_\nu) + (\bar{\psi}_e [O_i \, D'(I-\gamma_5)/2] \psi_\nu) \}_j + \text{h.c.}$$

$$+ \frac{G}{\sqrt{2}} \sum_{i,j} C_i' (\bar{\psi}_{p_j} O_i^j \psi_{n_j}) \cdot \{ (\bar{\psi}_e [O_i \, D'(I+\gamma_5)/2] \psi_{\bar{\nu}} + (\bar{\psi}_e [O_i \, D(I-\gamma_5)/2] \psi_{\bar{\nu}}) \}_j + \text{h.c.}$$

The subscript j runs over all the relevant nucleons in the nucleus. The current operators O have five possible forms, classified according to their transformation properties: scalar, pseudoscalar, vector, axial vector, and tensor. The subscript i runs over the five, S,P,V,A,T; the corresponding operators have the forms $O_S = I$, $O_P = \gamma_5$, $O_V = \gamma_\alpha$, $O_A = \gamma_\alpha \gamma_5$, and $O_T = i/2 \, (\gamma_\alpha \gamma_\beta - \gamma_\beta \gamma_\alpha) = \sigma_{\alpha\beta}$. The C_i's are the form factors mentioned in the introduction, which in the case of beta decay (small momentum transfer) reduce to constants.

Fermions such as the electron and neutrino are represented by four-component spinors in the Dirac theory; two components correspond to spin parallel to velocity (positive helicity or right-handedness) and two correspond to spin and velocity anitparallel (negative helicity). The operators $a = (I+\gamma_5)/2$ and $\bar{a} = (I-\gamma_5)/2$ project out the left-handed and right-handed parts of the wavefunction, respectively. If the interaction were strictly parity-conserving, it could not distinguish "handedness" and the coefficients D and D' in Eq. 4 would be equal, so the projection operators a and $\bar{a}$ would cancel each other and leave only a constant. In this case, both helicity states of the neutrino would enter equally into the decay. On the other hand, if the interaction were to exhibit maximal parity violation, one of the coefficients D or D' would

be zero, so that only one helicity state of the neutrino would occur. This is called the two-component theory of the neutrino. For a zero mass particle like the neutrino, the Dirac equation can be decoupled into two equations, each satisfied by a two component spinor having opposite helicities. In the two-component theory of the neutrino, the two spinors correspond to neutrinos (left-handed) and to antineutrinos (right-handed). Experiments have shown that only left handed neutrinos occur in nature, so the coefficients D' in Eq. 4 are zero (and the D's can be absorbed into the C_i's.)

Experiments have also indicated that only antineutrinos are emitted in negatron decay, so the C_i' are all zero and the second line of Eq. 4 may be dropped. This is referred to as lepton conservation. Also, it may be shown that invariance with respect to time reversal requires the constants C_i to be real; thus out of the original forty constants implicit in Eq. 4, only five remain. Finally, experimental evidence indicates that only the V and A interactions actually occur,* and the beta interaction assumes the form:

$$\text{Eq. 5} \qquad h_\beta = \sqrt{2}G \sum_j [\bar{\Psi}_f \gamma_\alpha (C_V - C_A\gamma_5)\tau_+^j \Psi_i] \cdot [\bar{\Psi}_e \gamma_\alpha (I+\gamma_5) \Psi_{\bar{\nu}}]_j$$

Here the neutron and proton wavefunctions have been replaced by a generalized nucleon wavefunction which is changed from neutron to proton by the isospin ladder operator τ_+, and the commutation relations of the γ matrices have been used to simplify the lepton term. Using the fact that the Dirac conjugate $\bar{\Psi} = \Psi^\dagger \gamma_4$ and the definitions of the operators $\underset{\sim}{\alpha}$, γ_5, and $\underset{\sim}{\sigma}$, gives:

---

* A universal V - A interaction was suggested by several theorists.[5,17,18]

Eq. 6 $$h_\beta = \sqrt{2}G \sum_j \{\Psi_f^\dagger [C_V(-i\underset{\sim}{\alpha}, 1) + C_A(i\underset{\sim}{\sigma}, \gamma_5)]\tau_+^j \Psi_i\} \cdot J_{e\nu}^j$$

where $\underset{\sim}{\alpha}$ is the relativistic velocity operator, $\underset{\sim}{\sigma}$ is the spin operator, and γ_5 is the helicity operator ($\gamma_5 = -\alpha_i \sigma_i$). The lepton current term has been abbreviated as $J_{e\nu}$.

Using this expression for the interaction, it should be possible to calculate physical quantities which can be measured, for example the decay rate dW/dt. Using the Golden Rule,

Eq. 7 $$dW/dt = (2\pi/\hbar)\, \rho_e\, \rho_\nu |\int h_\beta|^2$$

where ρ_e and ρ_ν are the densities of final states for the electron and neutrino. To simplify the calculation, several assumptions are usually made, resulting in a series of approximations:

1) Allowed Approximation

The lepton functions are expanded in powers of the radial variable r. In the allowed approximation, two assumptions are made: since the beta interaction is short range and since the nuclear radius R is small compared to the lepton wavelengths, only the zero-order term in the expansion in r (r = 0) is kept; and since the nucleon masses are large compared to their energies in beta decay, the relativistic nuclear terms (of order v/c) are neglected. In Eq. 6, the operators γ_5 and $\underset{\sim}{\alpha}$ are relativistic; thus in the allowed approximation, Eq. 6 reduces to:

$$h_\beta = \sqrt{2}G \sum_j \Psi_f^\dagger [C_V - C_A(i\underset{\sim}{\sigma})]\tau_+^j \Psi_i \cdot J_{e\nu}(0)$$

and the integrals in Eq. 7 become $C_V \int \Psi_f^\dagger \tau_+ \Psi_i \, dV_n + C_A i \int \Psi_f^\dagger \underset{\sim}{\sigma} \tau_+ \Psi_i dV_n$. The lepton part is constant and was factored out of the integrals, while the Wigner-Eckart theorem may be applied to simplify the angular parts.

The remaining radial integrals (reduced matrix elements) are usually denoted by $C_V \int 1$ and $C_A \int \underset{\sim}{\sigma}$ (although a more general tensor notation is also available [19]), and are called the Fermi and Gamow-Teller matrix elements, respectively. Both matrix elements vanish if the parities of Ψ_f and Ψ_i are opposite. The operator $\underset{\sim}{\sigma}$ is a tensor of rank one and connects states with $\Delta I = 1$ or 0 (except $0 \not\to 0$). Here I = nuclear spin.

A simple physical explanation for the foregoing is as follows: in the allowed approximation, (r = 0) the leptons have zero orbital angular momentum ($\underset{\sim}{L} = \underset{\sim}{r} \times \underset{\sim}{p}$) and thus can carry off only spin angular momentum. The electron and neutrino each has spin 1/2 and can couple at most to total angular momentum = 1. In the Fermi coupling, their spins are anti-parallel so they carry off zero angular momentum; in the G-T coupling they are parallel and carry off one unit of angular momentum. Fig. 2a shows a "finger physics" diagram for the case of G-T decay with $I_f = I_i - 1$. In allowed decays the beta spectrum shape is determined by the phase-space factors ρ_e and ρ_ν in Eq. 7 (statistical shape). Corrections for the Coulomb attraction or repulsion of the nuclear charge for the $\beta^{\pm}$ particles are made by multiplying by the Fermi function F(Z,E).

2) First Forbidden Approximation

In this approximation, the terms of order r in the expansion of the lepton functions are kept, as are the nucleon relativistic terms. Six matrix elements are obtained: $C_V \int \underset{\sim}{r}$, $C_V \int \underset{\sim}{\alpha}$, $C_A \int \gamma_5$, $C_A \int \underset{\sim}{\sigma} \cdot \underset{\sim}{r}$, $C_A \int \underset{\sim}{\sigma} \times \underset{\sim}{r}$, and $C_A \int (\sigma_i r_j + \sigma_j r_i - 2/3 \underset{\sim}{\sigma} \cdot \underset{\sim}{r}) = C_A \int B_{ij}$. The third and fourth matrix elements contain tensor operators of rank zero and connect states of $\Delta I^{(\Delta\pi)} = 0^-$; the first, second, and fifth contain operators of rank one

and connect states with $\Delta I^{(\Delta\pi)} = 1$ or 0^- (no $0 \rightarrow 0$); and the sixth matrix element has a tensor operator of rank two and connects states having $\Delta I^{(\Delta\pi)} = 2^-$, 1^- (no $1 \leftrightarrow 0$), and 0^- (no $1/2 \rightarrow 1/2$ or $0 \rightarrow 0$). A decay of the type $\Delta I^{(\Delta\pi)} = 2^-$ thus has only the $\int B_{ij}$ term and is called unique forbidden.

In general, nth forbidden decays contain matrix elements of the types $\int Y_n r^n \; r\{\underset{\sim}{1}_{\sigma}\}$ and $\int Y_{n-1} r^{n-1} \{\underset{\sim}{\gamma}_{5\alpha}\}$ where Y_n is a spherical harmonic of rank n.[20]

Inner Bremsstrahlung

The IB is a second-order process whose decay rate is given by

Eq. 8 $$dW/dt = (2\pi/\hbar)\rho_e \rho_\nu \rho_\gamma \; |\int h_\beta|^2 \; |\int h_\gamma|^2$$

where h_γ is the electromagnetic interaction mentioned earlier. A diagram for the process is shown in Fig. 1. Since the EM interaction is of order $\alpha = 1/137$, IB emission is a much weaker process than beta decay. Shortly after the publication of the Fermi theory, several authors[1,2] calculated the IB intensity, spectrum shape, and electron-photon directional correlation for IB accompanying negatron decay. Somewhat later a similar calculation was made for K-electron capture IB.[3] In the electron capture radiative decay, the decay energy is shared between only two particles, the neutrino and the photon; thus this case is equivalent to nonradiative positron emission (with the positrons replaced by photons and thus having zero mass). The IB spectrum then has the statistical shape (from allowed K captures) with no Fermi function correction necessary. In allowed particle emission decays, the particles only have maximum polarization and directional asymmetry in the extreme relativistic limit ($v/c \simeq 1$), i.e. at high energies. In IB accompanying K capture, however, the photons are totally relativistic at all energies and so their polarization and

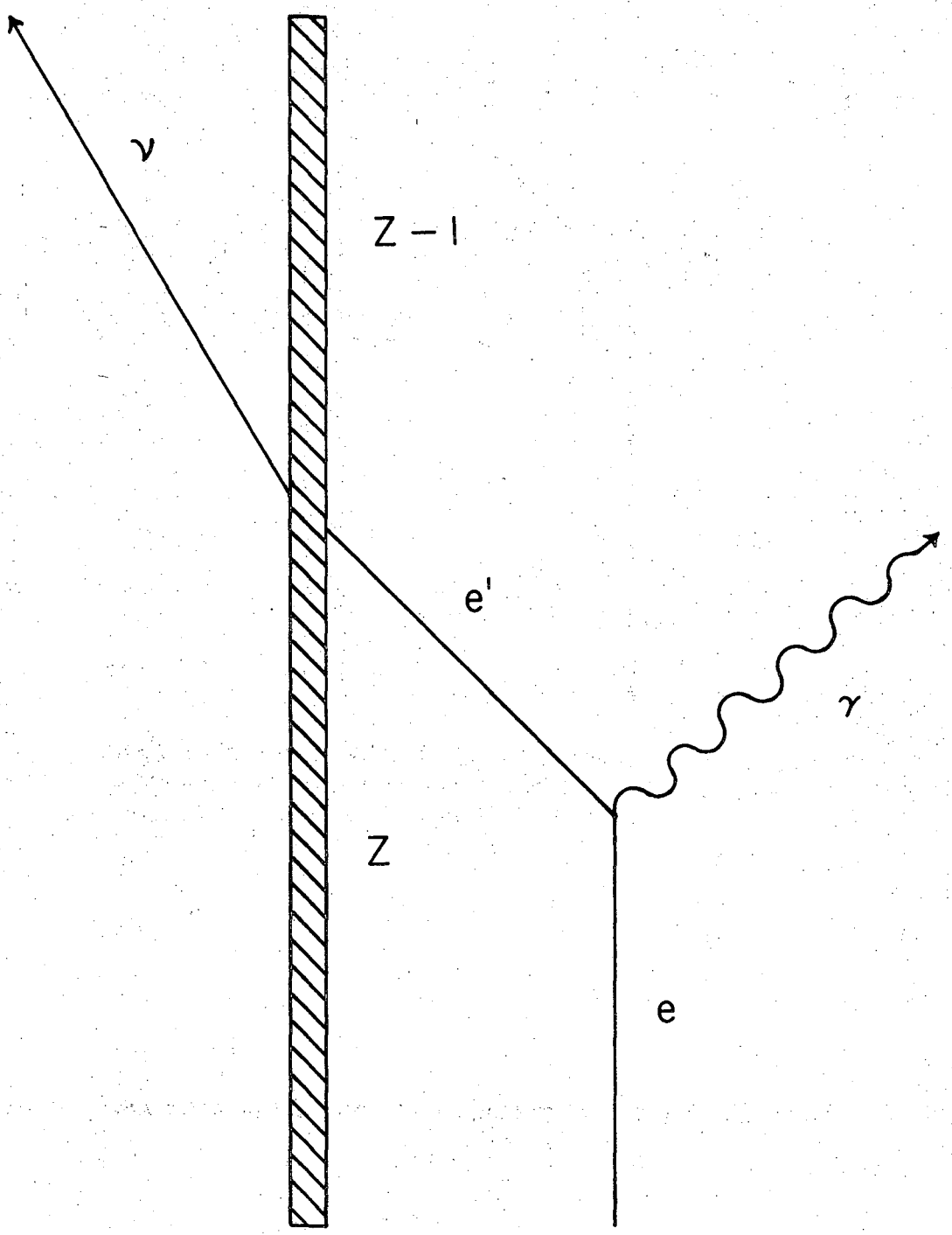

XBL 682-163

Fig. 1 Diagram for radiative K capture. The s electron e emits a photon and enters an intermediate virtual state e', from which it is captured by the nucleus at the weak vertex.

asymmetry are, to first order, independent of photon energy. The angular distribution of IB photons is given by the usual correlation function $W(\theta) = 1 + A_1 G_1(T)\ P_1(\cos\theta)$. The function G_1 describes the degree of nuclear polarization and is related to the B_1 of Chap. I by a normalization factor; the series is terminated at k = 1 because the IB asymmetry is like that of a positron, which carries 1/2 unit of angular momentum in an allowed decay and therefore has $k_{max} = 1$. The asymmetry parameter A_1 for the simple case of allowed G-T decay with $I_f = I_i - 1$ may be determined by momentum conservation considerations as shown in Fig. 2b. For other spin sequences or for mixed Fermi and Gamow-Teller transitions, A_1 is given by the usual forms for positrons: $I_f = I_i + 1$, $A_1 = -I_i/(I_i+1)$; $I_f = I_i$, $A_1 = 1/(I+1)$ (pure G-T) and a more complex expression involving C_A/C_V for mixed transitions.[21,22] For pure Fermi decays, $A_1 \equiv 0$.

The above remarks apply to K capture IB; other orbital electrons may also be captured. Capture of 2s electrons leads to results similar to 1s capture. Capture of p electrons, however, leads to isotropic and unpolarized IB.[23] 2p capture may be considered to be a two step process producing IB which is essentially virtual X-radiation. (See diagram in Fig. 3). The branching ratio for radiative decay $\frac{(W_{\text{IB decay}})}{(W_{\text{tot. K capt.}})}$ has the form [3,23] $\alpha/\pi(mc^2)^2 \int_0^{E_o} k(1-k/E_o)\ R_{1s}\ dk \simeq \alpha\ /12\pi(E_o/mc^2)^2$. R_{1s} is a relativistic correction which was neglected in the second expression; E_o is the endpoint energy. It can be seen that IB is strongly favored by large endpoint energies. However, if $E_o \geq 2mc^2$, positron emission is also allowed, and this interferes with the observation of IB by giving rise to

Fig. 2a. Allowed negatron decay for $I_f = I_i - 1$. The spins of the e^- and the $\bar{\nu}$ must be parallel to each other and to the nuclear spins to conserve angular momentum. The antineutrino is right handed and therefore emerges parallel to I; the negatron must emerge in the opposite direction since it is left handed.

Fig. 2b. A similar case for radiative K capture. Capture of the intermediate virtual negatron is equivalent to emission of a positron so the negatron must be in a positive helicity state (as is an emitted positron). Since its spin must be antiparallel to the initial nuclear spin, its momentum p must also be antiparallel and the photon must be emitted parallel to the nuclear spin to conserve linear momentum. Thus $A_1 = +1$ (maximum asymmetry, parallel emission).

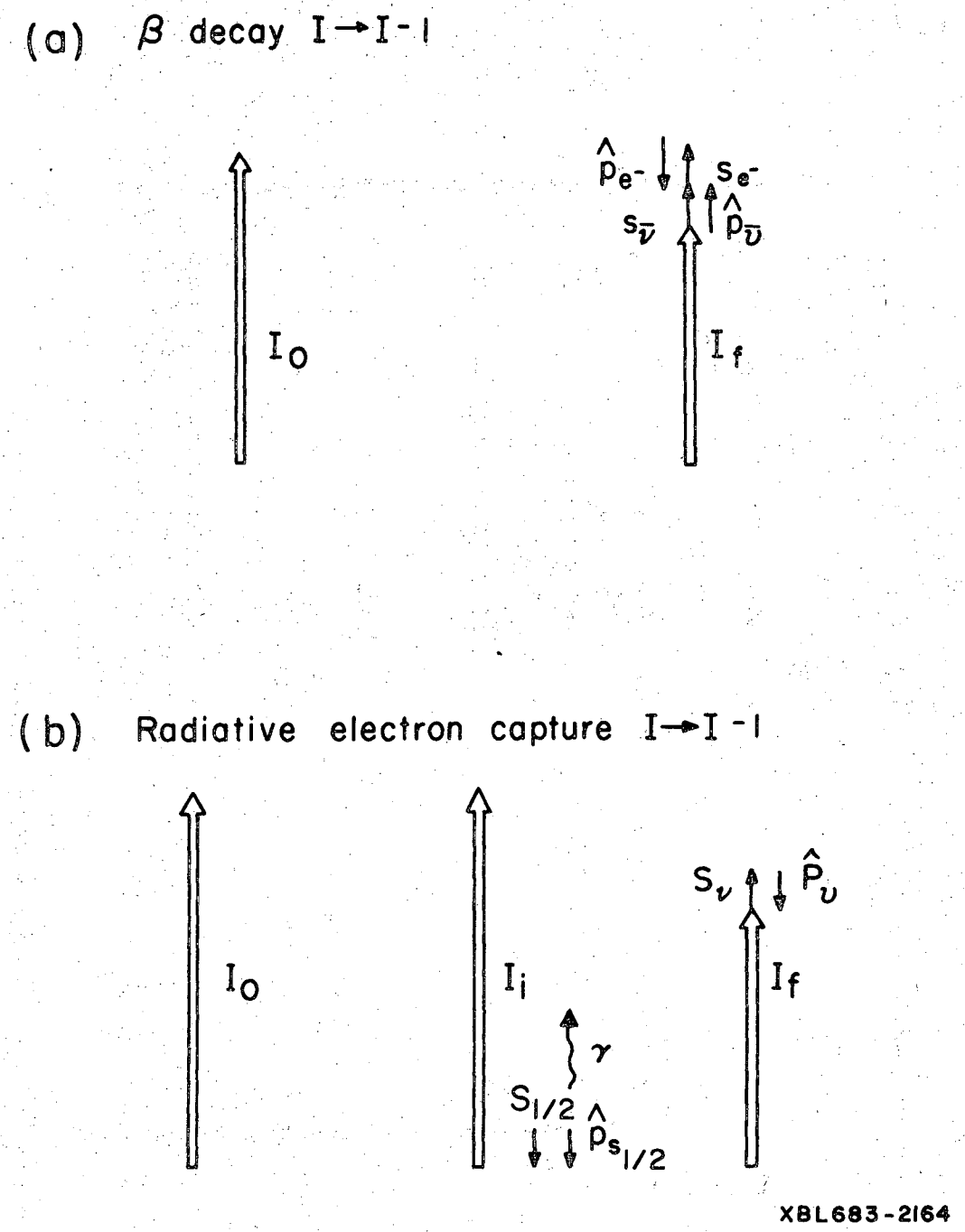
(a) β decay I→I-1
I_0
$\hat{p}_{e^-}$
s_{e^-}
$s_{\bar{\nu}}$
$\hat{p}_{\bar{\upsilon}}$
I_f
(b) Radiative electron capture I→I-1
I_0
I_i
γ
$S_{1/2}$
$\hat{p}_{s_{1/2}}$
S_ν
$\hat{P}_\upsilon$
I_f
XBL683-2164

Fig. 2

Fig. 3. Radiative 2p electron capture. 3a.: A p electron emits a photon and enters a virtual state, from which it is captured. 3b.: A 1s electron is captured, leaving a 1s hole, while a p electron emits a photon and enters a virtual state from which it occupies the hole. No condition on the helicity of the p electron exists, so the photon may be emitted in any direction.

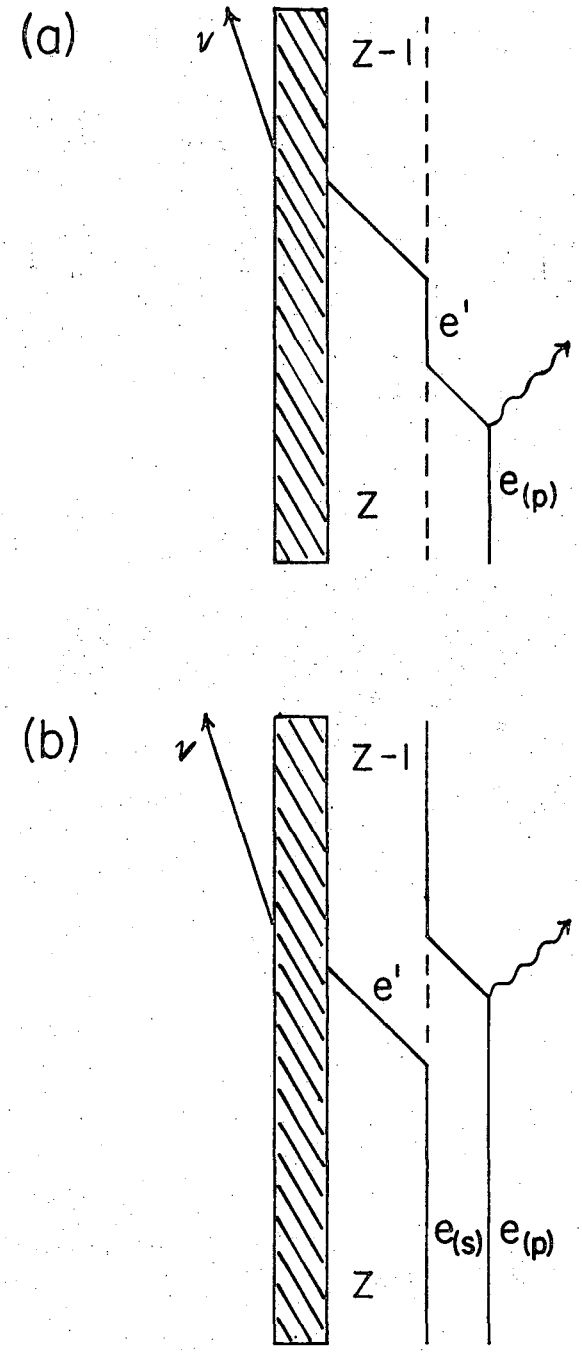

XBL 6912-6711

Fig. 3

external bremsstrahlung (EB). Thus an ideal case from an observational point of view is a decay with E_o large but less than 1 Mev.

Conserved Vector Current

As explained in the introduction, CVC extends the analogy between the weak interaction and the electromagnetic interaction. The electromagnetic current has two parts, the isovector and the isoscalar parts. In the general case of arbitrary momentum transfer, the isovector nucleonic EM current is

Eq. 9 $$J_\alpha^z = \bar{\Psi}'[(F_V(q^2)\gamma_\alpha - iM_V(q^2)\sigma_{\alpha\beta}q_\beta)\tau_z]\,\Psi$$

where F_V and M_V are form factors which are functions of the momentum transfer q. Because of charge conservation, $F_V(0)$ = const., i.e. F_V is unrenormalized by the strong interaction. The second term on the right hand side of Eq. 9 produces the anomalous magnetic moments of the proton and the neutron. Similarly, the general weak vector nucleonic current may be written

Eq. 10 $$J_\alpha^\pm = \bar{\Psi}'[(f_V(q^2)\gamma_\alpha - if'_V(q^2)\sigma_{\alpha\beta}q_\beta + f''_V(q^2)\,q_\alpha)\tau_\pm]\,\Psi$$

which is similar to J_α^z except for the last term. This term corresponds to one which would appear in J_α^z except for conservation of the EM current (div.J^z = 0), which requires it to be identically zero. If we assume that the weak vector current is likewise conserved, $f''_V(q) = 0$ and the currents J_α^z and $J_\alpha^\pm$ have the same form and contain the three components of the isospin operator τ. Thus they form an isovector triplet and we have $f'_V(q)/f_V(q) = M_V(q)/F_V(q)$. The $f'_V(q)$ term is called the weak magnetism term. The weak form factors have now been related to the EM form factors, which are well known. We have $f'_V(0)/f_V(0) = (\mu_p - \mu_n)/2M$

where μ_p and μ_n are the proton and neutron magnetic moments and M is the nucleon mass.

As pointed out by Fujita[24] and Eichler[25], div. $J^{\pm}$ is not exactly zero, due to the fact that the nuclear force is not precisely charge-independent: the weak current is a "charged" current, containing the charge-changing operator $\tau_{\pm}$; it cannot be strictly independent of the nuclear force because of the neutron-proton mass difference and the Coulomb term in the nuclear energy. The above authorscalculated the residual divergence of $J^{\pm}$.

In EM theory, the Siegert theorem[26] can be used to obtain relationships between certain EM matrix elements involving currents and matrix elements involving only charge densities. The expansion of the lepton functions in beta decay theory and the resulting series of approximations (allowed, 1st forbidden, etc.) may be likened to the multipole expansion of EM transition matrix elements (allowed beta decays correspond to E0 and M1 transitions). By extending the analogy between EM interactions and vector beta interactions, one could use the Siegert theorem to derive relationships between various vector ("electric") beta matrix elements, e.g. between $\int \underset{\sim}{\alpha}$ (the "E1"matrix element) and $\int \underset{\sim}{r}$. This would reduce the number of parameters to be measured in determining nuclear matrix elements from beta-decay measurements, as pointed out in the introduction. The Siegert theorem cannot be applied directly, however, because of the non-vanishing divergence of the weak vector current mentioned above. Fujita and Eichler used the calculated residual divergence to correct the Siegert-theorem relationships for application to beta decays, and derived the following relationship:

Eq. 11 $\int \underset{\sim}{\alpha} / i \int \underset{\sim}{r} = -[2.4\alpha Z/2R + (E_o - 2.5)m_e]$

here $\alpha Z/2R = \xi$ is the electron's Coulomb energy at the nuclear surface (α = fine structure constant) and E_o is the decay energy, in mc^2 units. This formula assumed a uniform spherical nuclear charge distribution and the Ahrens-Feenberg approximation.[27] It was later suggested by Damgaard and Winther[28] that the latter approximation is not sufficiently good to apply to cases of interest indiscriminately. It has also been pointed out that even if Eq. 11 were exact, its being fulfilled in actual decays is a necessary, but not a sufficient condition for establishing CVC, since the non-CVC theory could give approximately the same ratio.[25]

Beta-Nuclear Angular Distributions from 1st Forbidden Decays

In decays of the type $1^- \rightarrow 0^+$ or $1^- \rightarrow 2^+$, the angular distribution of the beta particles emitted by polarized initial nuclei is as follows:[29]

$$\text{Eq. 12} \quad W(\theta) = 1 + \sum_k B_k P_k(\cos\theta) \frac{\sum_{L \leq L'} b^{(k)}_{L,L'} W(I_i I_i LL'; kI_f) (-1)^{L+L'+k}}{\sum_{L'' \leq L'''} b^{(0)}_{L'',L'''} W(I_i I_i L''L'''; 0I_f)}$$

The sum on k terminates at k = 2 when $I_i = 1$. L and L' have maximum values of 2 in 1st forbidden beta decays and must couple to k. The b's are tabulated[20, 29] functions of the nuclear matrix elements and the lepton functions and are the parameters to be determined. In general, one measures the b's and then calculates the lepton functions and assumes a set of nuclear matrix elements; from these a set of trial calculated b's can be obtained, and the trial matrix elements adjusted as necessary to improve the fit to the measured b's. When convergence is obtained, the matrix

element trial values used are the correct ones. More elaborate analyses may also be performed, using all available data and attempting to minimize the χ^2 for a trial set of matrix elements in the fit to the data.

In the ξ approximation, only the P_0 and P_1 terms remain in Eq. 12. In the B_{ij} approximation the P_3 term is large.

Inner Bremsstrahlung Experiments, Introduction

Selection of an isotope suitable for measurements of the angular distribution of IB photons from polarized nuclei poses several requirements: the parent state must be capable of being polarized to an appreciable degree by available methods; the half-life of the decay must be reasonably long (>24 hrs.) to permit working with the source for the necessary time; and the IB spectrum must be observable without interference from other radiations. A number of isotopes meet these criteria.

Some preliminary experiments were performed with ^{147}Pm, which can be polarized by inclusion in a paramagnetic crystal (e.g. cerium magnesium nitrate) by the magnetic hf polarization method. This isotope decays by negatron emission, however, and the beta particles must be stopped in an absorber, which then gives rise to EB which has about the same intensity as the IB. The IB spectrum was observed, and corrected for EB by using several absorbers of differing atomic number and extrapolating to zero absorber Z, but it was felt that this procedure was of uncertain value in the restricted geometry of a nuclear polarization cryostat.

The EB problem can be avoided by using nuclei which decay only by electron capture. Here the only possible interfering radiations are x-rays and gamma rays from the daughter nucleus. Considering only decay scheme, one finds a number of candidates, including ^{55}Fe, ^{71}Ge, ^{73}As, ^{119}Sb, ^{125}I, ^{131}Cs, ^{134}Ce, ^{166}Yb, and ^{179}Ta, all having pure allowed Gamow-Teller decays (^{57}Co should also be included in this group, although it has a weak gamma ray just above the IB endpoint). There are two mixed F-G.T. decays, those of ^{37}Ar and ^{49}V. Several forbidden decays also appear, notably those of ^{53}Mn, ^{59}Ni, ^{91}Nb, and ^{93}Mo. The last isotope decays by

a mixture of unique and second forbidden electron captures. In the foregoing list, several isotopes are unsuitable for polarization by the "universal" method: Ar, Nb and I as well as the rare earths can be put into an iron lattice only by ion implantation or recoil techniques; and the magnetic dipole moment of ^{55}Fe is probably too small.

The first IB experiments with polarized nuclei were performed using a ^{49}V:Fe source. No photon asymmetry was observed in these experiments. Since the ^{49}V decay is mixed F-G.T., it is quite possible that the asymmetry is small or zero due to interference of the two multipolarities; in fact, a measurement of the asymmetry gives the mixing ratio. However, the ^{49}V results must be regarded as inconclusive and further work is necessary to establish its correct IB asymmetry.

For an unambiguous test of the IB asymmetry theory, a pure G.-T. decay is desirable. Of those listed above, only the ^{119}Sb was an isotope of an element which had previously been polarized by the universal method (except ^{57}Co, which has interference from the gamma ray at 706.4 kev.). Since ^{119}Sb has a reasonably large magnetic dipole moment and can be readily placed in an iron lattice by melting, and since its preparation is not too difficult, this isotope was chosen for further IB asymmetry experiments despite its relatively short half-life of 37 hrs. These experiments are described in detail in the following pages.

Nuclear Orientation Apparatus for ^{119}Sb Experiments

The cryostat used in the ^{119}Sb polarization experiments (Fig. 4) was similar to the one described by Westenbarger.[30] It employed two glass dewar vessels about four feet long, with constricted tails at the bottoms. During an experiment, the outer dewar was filled with liquid

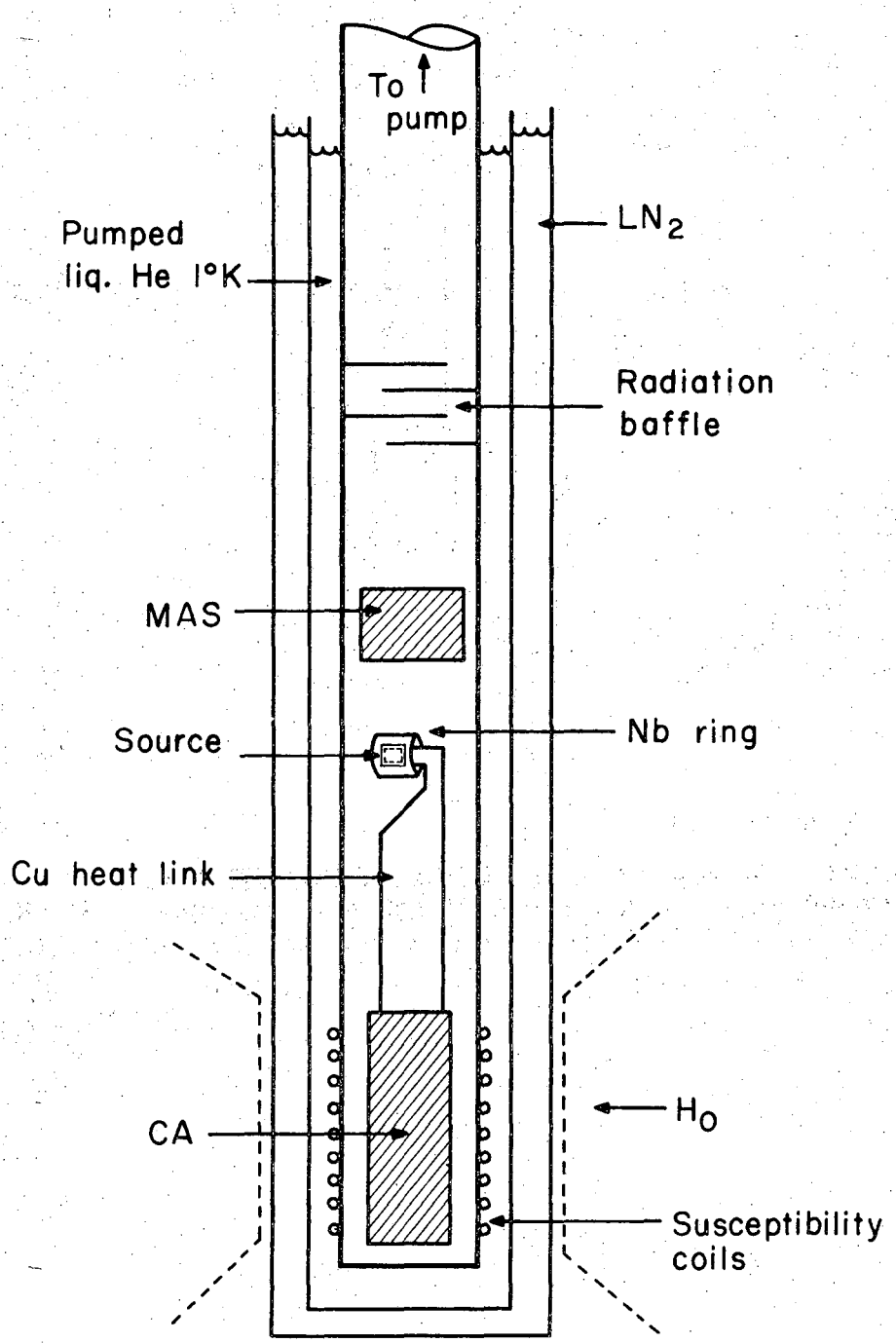

Fig. 4. Schematic diagram of apparatus used to polarize ^{119}Sb nuclei. The dotted lines represent the magnet pole pieces. After demagnetization, the gamma counters occupied similar positions on the axis of the Nb ring.

nitrogen, while the inner dewar was filled with liquid helium pumped to a temperature of about 1° K. The dewar tails fitted into the pole gap of a 23 koe. iron yoke magnet, which could be rolled on rails up to the apparatus. The experimental chamber was a glass tube about 12" long and 1-1/4" diameter, which was attached by means of a copper-glass housekeeper seal and a gutter seal to a stainless steel pumping tube; the latter was suspended in the center of the inner dewar from the top. Inside the experimental chamber was a brass support cage, from which the glass container holding the cooling salt slurry (potassium chromium sulfate or chrome alum = CA, in glycerin) was suspended by three .005" nylon monofilaments. Above and below the cooling salt were pressed pills of manganous ammonium sulfate (MAS) which served as radiation guards and as cryopumps for residual exchange gas. Thermal contact to the sample was obtained with a set of twenty copper fins immersed in the CA slurry. At the top, the fins were soldered together and cut to form a horizontal arm to which the sample foils were soldered. Around this arm was a niobium flux-trapping ring which maintained a magnetic field of about 2 koe. on the sample foil after demagnetization.[30] Samples could be cooled to about 14 mdeg. K. with this apparatus and warmup to 75 mdeg. required about an hour. Around the cooling salt and (empty) portion of the experimental chamber were two matched mutual inductance coils with primary and secondary windings, which were used in conjunction with a mutual inductance (ac) bridge to measure the magnetic susceptibility of the CA during a run.

Radiation Detectors

the gamma radiation detectors used for the ^{119}Sb experiments were 3×3" Na(Tl)I crystals commercially mounted on photomultiplier tubes. The resolutions (FWHM at 662 kev.) were about 7% for each detector. Because of the need to reduce room background when counting the IB, the detectors were enclosed in 8" dia. lead shields; they were also magnetically shielded with μ-metal and with soft iron tubes surrounding the entire photomultipliers and the entire counter assemblies, respectively. Each counter and its attendant shielding (weighing 235 lbs.) was mounted on a small carriage which could be rolled along a track attached to a counting table. The table ran on the same track as the magnet, and after a demagnetization, the table was rolled up to a position below the dewar tails and the two counters were brought together on each side of the dewar by means of a screw drive. The lead shields were notched to admit the dewar tails and when the counters were in the closed position the only opening in the shielding was the one through which the dewar tails emerged.

The photomultiplier outputs were connected to charge-sensitive solid state preamplifiers, whose outputs were in turn fed to linear-amplifier pulse shapers and then to single-channel analyzers. The IB spectrum could be recorded directly on a multichannel analyzer while at the same time a gated portion of the spectrum was summed by a single-channel scalar through the SCA. In some of the experiments, an on-line PDP-7 computer equipped with analog-digital converters was used to analyze the spectra and store them on magnetic tape.

^{119}Sb Experimental Procedures

A sample of 38 hr. ^{119}Sb was made by the sequence $Sn(\alpha,3n)^{119}Te \xrightarrow{\varepsilon} {}^{119}Sb$.[31] Natural tin foils of .005" thickness were irradiated with 55 Mev. alpha particles at the Berkeley 88" cyclotron, using integrated beam currents of 75-100 μamp hrs. A high degree of separation of the ^{119}Sb from gamma-emitting impurities was necessary, because of the low intensity of the IB spectrum. The following scheme proved satisfactory:

The target foil was dissolved in conc. HNO_3 + HF. The solution was evaporated and small amounts of Sb and Te (5-10 mg.) natural carriers were added. The residue was dissolved in HBr and evaporated two times to vaporize Sb impurities resulting from α,d reactions and target impurities; it was then dissolved in HCl and made up to 50 ml. volume and 4 M. HCl. The solution was heated to near the boiling point and saturated with SO_2 gas for five minutes, causing precipitation of metallic Te. The precipitate was centrifuged down, washed with hot water and re-centrifuged, and then dissolved in a minimum of conc. HNO_3. This solution was diluted with HCl and boiled to remove nitrate, and the Te precipitation was repeated. In all, the precipitation was done five times; after the third time, a few mg. of Fe carrier were added to the HCl solution, and then precipitated by addition of NH_4OH. The $Fe(OH)_3$ precipitate scavenges impurities while leaving the Te in solution. After the final Te precipitation the precipitate was dissolved in HNO_3 as before, diluted with HCl and concentrated, and then stored for 4-1/2 days to allow the ^{119}Sb daughter to grow. (The only potential contaminant is the 5 hr. ^{118}Sb isomer; however, the ^{118}Te decay feeds only the 3.5 min. ground state of ^{118}Sb, which rapidly decays

away. The other Te isotopes produced in the reaction all give stable iodine isotopes or very short-lived antimony isotopes.)

After the ^{119}Sb had reached its maximum concentration (about 20% of the original ^{119}Te), a second set of purifications had to be performed to separate the Sb from its Te parent. To the solution resulting from the initial separation was added a small amount (about 50 µg.) of Sb carrier.* The solution was then heated and saturated with SO_2 as before to precipitate Te. After removal of the precipitate the SO_2 was driven off by heating, 5 more mg. of Te carrier were added, and the precipitation was repeated. After each precipitation the solution was filtered through a freshly cleaned fine sintered glass funnel to remove all traces of the precipitate. The procedure was repeated about six times, with checking for purity by gamma counting each time after the fourth precipitation. When the desired purity was reached, the solution was concentrated to a small volume and diluted with water to make it about 2 M. in HCl; a piece of .001" thick x 5 mm square 99.99% Fe foil was then stirred in the solution for about 1/2 hr. Because of the difference in electrode potentials between Fe and Sb, the Sb is reduced at the surface of the iron and plates onto the foil. When the plating was complete, the foil was folded into a small square and wrapped in a second piece of iron foil, and then melted by being lowered in an Ar-filled quartz tube into a resistance furnace preheated to 1600° C. After about two minutes (long heating times resulted in loss of Sb by vaporization) the sample was withdrawn, cooled, and pounded with an electromechanical hammer to a thickness of .002".

---

* Carrier-free separations, including carrying the Sb on precipitated Sn and then separating the Sb and Sn by electrodeposition, and solvent extraction of $SbBr_5$, were tried, but gave insufficient purification.

The sources were then annealed at 900° C. in quartz bulbs containing 1/4 atm. of Ar for 2-3 hrs. and cooled slowly over a 3 hr. period. Counting of pieces of the foils showed no inhomogeneities in activity; Sb concentrations were about 0.5 at.%.

Spectrum and Background Corrections

The decay scheme of ^{119}Sb is shown in Fig. 5. As can be seen, there are no interfering radiations in the IB spectrum except for the 23.8 kev. gamma ray and the Sn x-rays.

The energy response of the gamma ray detectors was measured in the experimental geometry by using several monoenergetic gamma sources with energies from 60 kev. to 662 kev. The pulse height spectra obtained were approximated analytically by three gaussian and two fermi functions which represented the photopeak, iodine x-ray escape peak, backscatter peak, and Compton distributions. The spectrum data were then interpolated by a computer program to calculate the response matrix R (defined so that R_{ij} is the probability that a gamma photon in energy interval j will produce a count in pulse-height channel i). If an arbitrary gamma-ray spectrum is then represented by a vector I_j with components giving the intensity in energy interval j, the vector $H_i = \sum_j R_{ij} \cdot I_j$ gives the pulse height spectrum in channel numbers i. The matrix R can be inverted to allow the computation of true gamma-ray spectra from observed pulse-height spectra. In the present case, R was used to convert the known IB spectrum of ^{119}Sb [31] to a pulse-height spectrum corresponding to the detectors and geometry used in these experiments; the resulting spectrum is compared with the observed one in Fig. 6. Since the agreement is reasonably good, no background corrections were initially made to the data.

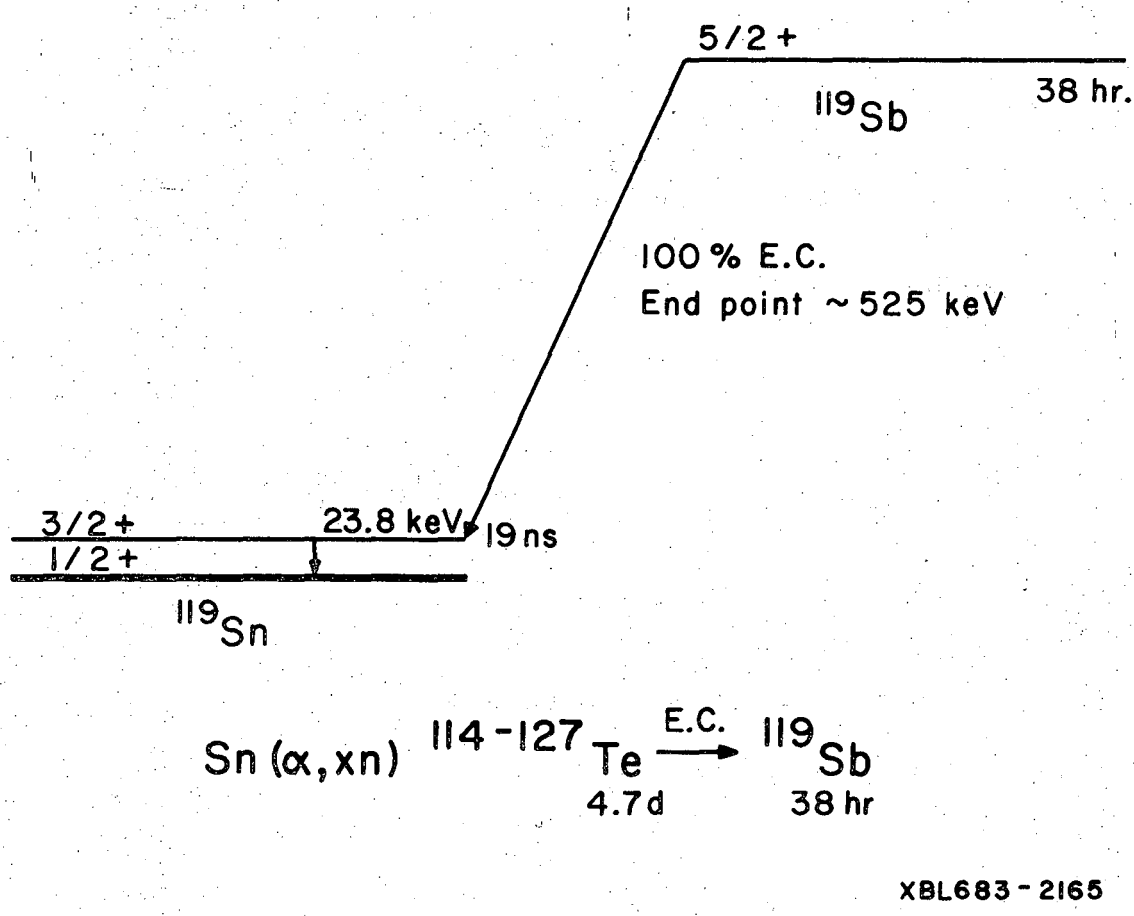

Fig. 5 Decay scheme and preparation method for ^{119}Sb.

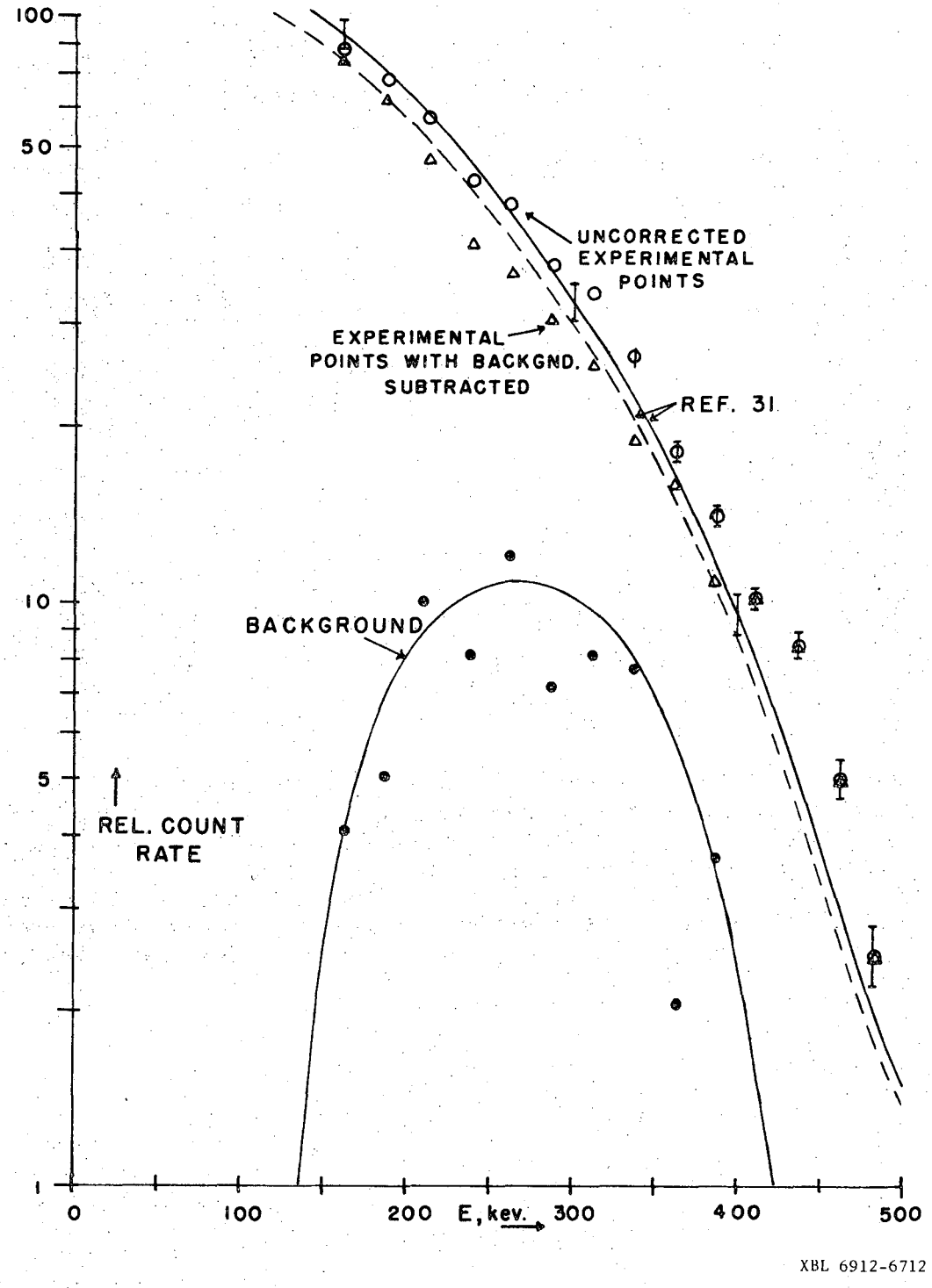

Fig. 6. Comparison of IB spectrum measured in this work with that of Ref. 31. The solid line has been corrected to the response of the present counting system. The errors on the experimental points are statistical only; Ref. 31 errors include uncertainties in the response functions. The triangular points have had the background shown below subtracted, and the dashed curve is the Ref. 31 spectrum renormalized to match the triangular points. (See Chap. V.)

Thermometry

A comparison with theory requires that the IB asymmetry be measured as a function of the degree of nuclear polarization, which in turn is a function of the temperature of the source. Two methods were employed for determining the source temperature: internal and external radioactive thermometry. In the internal method, a small amount of ^{60}Co was diffused into the ^{119}Sb:Fe alloy during the annealing step. Since the hyperfine parameters and decay scheme of ^{60}Co are well known, a measurement of the gamma ray anisotropy from a source of oriented ^{60}Co nuclei allows determination of the temperature to the statistical accuracy of the counting. Unfortunately, the Compton distribution from the high energy ^{60}Co gamma rays underlies the IB spectrum from ^{119}Sb, requiring a correction for a temperature-dependent background in the IB asymmetry data. This could be done precisely if the exact ratio of IB to background and the anisotropy of the background were known; the former can be obtained from the known response of the detectors and the latter can be measured in a separate experiment using a pure ^{60}Co:Fe source. However, the accuracy of the IB asymmetry measurements suffers from the propagation of errors in such a procedure. Thus the relative intensity of the ^{60}Co must be kept low, which makes the thermometry statistics poor.

To circumvent this difficulty, the external thermometry method was used: a source of ^{60}Co:Fe was soldered to the heat link and the apparatus cooled as usual. A correlation was measured between the actual sample temperature determined from the ^{60}Co gamma ray anisotropy and the "magnetic temperature" of the CA slurry as determined from the susceptibility.

Subsequently the ^{119}Sb:Fe alloy was soldered to the fin system, replacing the ^{60}Co alloy, and the cooling was repeated. Measurement of the magnetic temperature then allowed determination of the true sample temperature. The consistency of the results and their agreement with the internal thermometry runs gives confidence in the usefulness of the method. (It should be noted that the temperatures reached in these experiments were not extremely low, so that small variations in the condition of the heat link, the solder joint to the source, radioactive heating, etc. should not have had too large an effect on the temperature. The initial temperature and warmup rates seemed to be determined by the external heat leaks, which presumably were constant throughout the experiments.)

In all, four alloys were cooled and the IB asymmetry determined. Consistent results were obtained in all cases. The combined data in the energy range from 125-500 kev., fitted to the function $W(\theta) = 1 + G_1 Q_1 A_1 P_1$ (See Chap. II) are shown in Fig. 7.

Data Analysis and Scattering Corrections

The theoretical value of the asymmetry parameter A_1 was shown in Chap. II to be +1.0. The value of A_1 obtained from the data in Fig. 7 is $+0.506 \pm 026$. Several considerations may explain the discrepancy. First, no correction has been made to the data in Fig. 7 for the p-capture part of the IB spectrum, which underlies the s-capture part at low energies. (The Fig. 7 data were corrected only for decay during experiments, solid angle of the detectors, and background where applicable.) As pointed out in Chap. II, the p-capture IB is expected to be isotropic. The ratio of p- to s-capture IB measured in Ref. 31 (and in good agreement with the

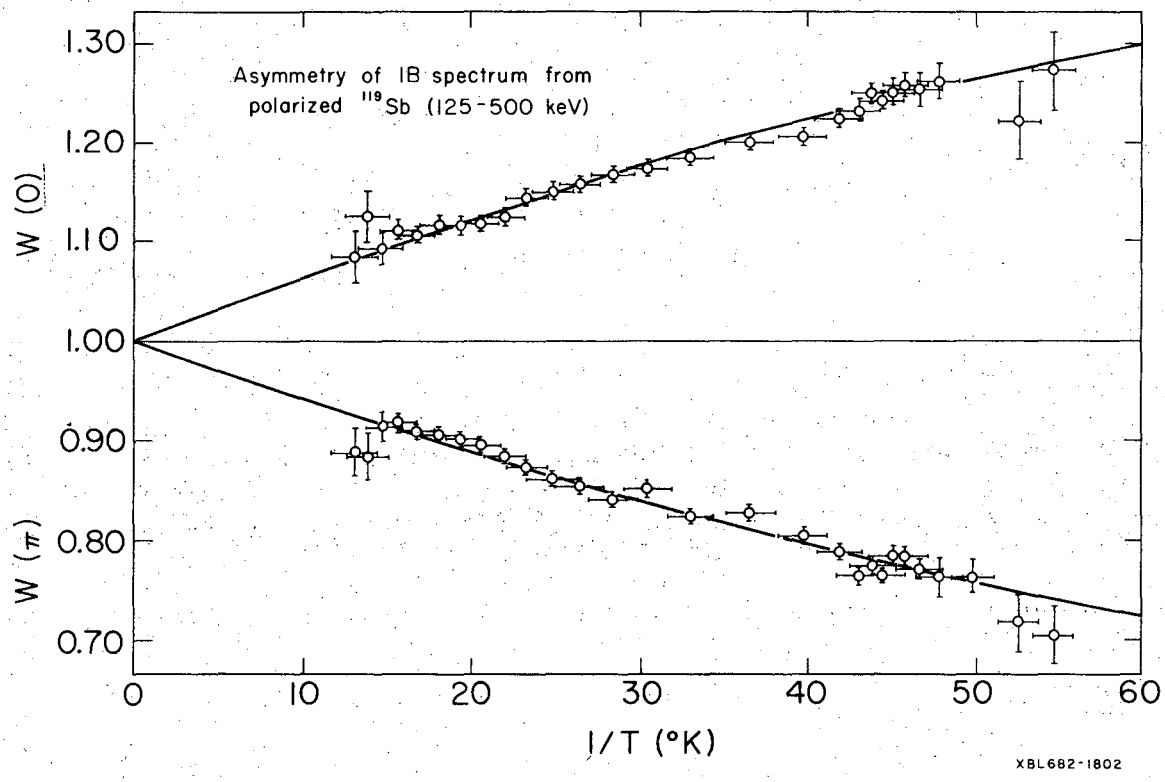

Fig. 7. Asymmetry of the ^{119}Sb IB spectrum at two angles as a function of sample temperature. The solid curves are fits to the function $W(\theta) = 1 + A_1 G_1(T)\, Q_1 P_1(\cos\theta)$. The parameter Q_1 is a solid angle correction; G_1 describes the degree of nuclear polarization and is given by $G_1 = [\sum_m m \cdot \exp(-\beta m)]/[I \cdot \sum_m \exp(-\beta m)]$. G_1 is related to the orientation parameter B_1 by a normalization factor.

calculation of Ref. 23) was used to correct the expected asymmetry at low energies. Some of the data plotted as asymmetry vs. energy at a constant temperature are shown in Fig. 8. The upper dashed curve shows the theoretical asymmetry corrected for the p-capture part of the spectrum. As can be seen, the experimental values still deviate from theory, especially at low energies. This suggests a second consideration, corrections for scattering.

The IB photons emitted by the source were scattered by the source foil, the heat link, the flux-trapping ring, the apparatus walls and the detector shielding. However, the source foil was rather thin, the apparatus walls were glass and therefore did not contribute heavily to scattering, and the shielding was outside the detectors and thus contributed mostly backscatter, which falls at energies below 125 kev. for the most part. This leaves the heat link and the flux-trapping ring. The heat link was asymmetric in shape and thus should give an asymmetric scattering pattern which would cause the observed asymmetry of the IB to deviate in one direction in the $\theta = 0$ counter and in the other direction in the $\theta = \pi$ counter. From Fig. 7 it may be seen that no such effect is present outside statistics. Thus it may be concluded that the flux-trapping ring was the principal cause of any scattering which occurred. This is not surprising since it was fairly thick and subtended a large solid angle around the source. Accordingly, calculation of the amount of scattering to be expected from the flux-trapping ring and the consequent effect on the observed IB asymmetry was undertaken.

The geometry of source, ring, and detectors was well known. The

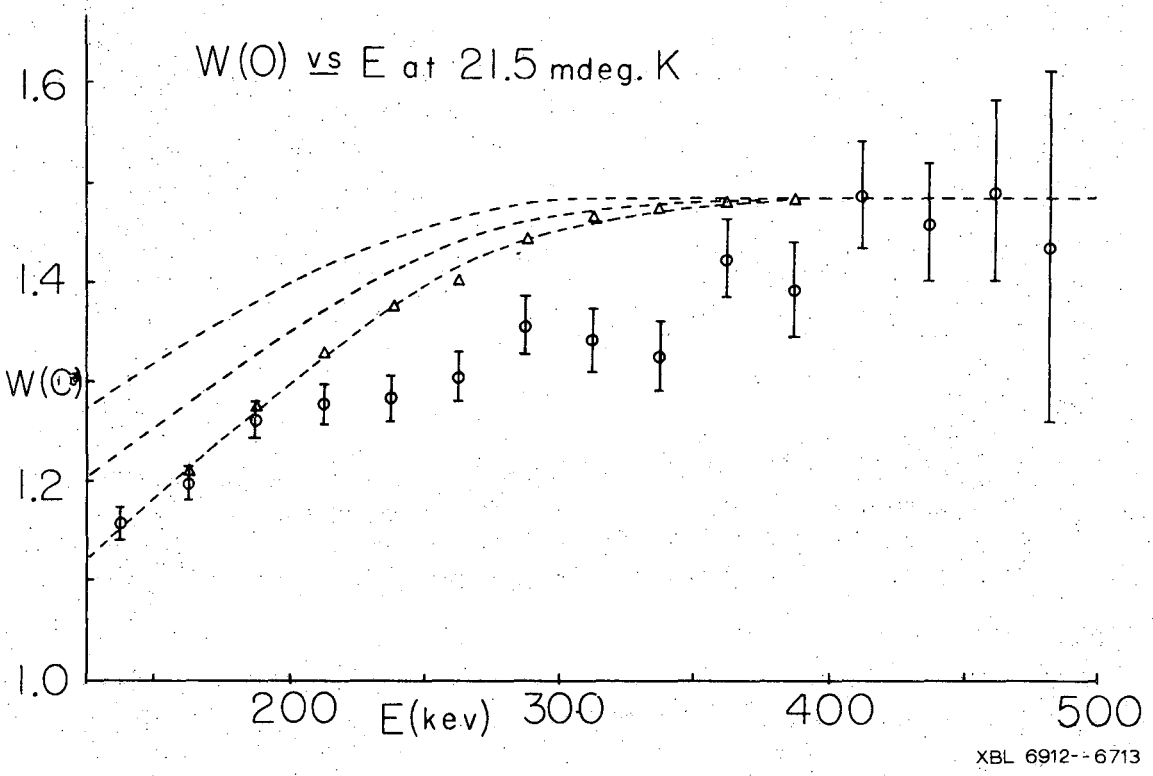

Fig. 8. Asymmetry of IB at one temperature as a function of photon energy. The dashed lines are explained in the text. The triangles are points corrected for the background shown in Fig. 6.

calculation assumed Klein-Nishina scattering.[32] A computer program was written to calculate the probability that a photon emitted at energy E and angle θ to the quantization axis, and thus having asymmetry proportional to cos θ, would be scattered into a detector and be observed as a count in channel i. The scattering probability was multiplied by the spectrum shape S(E) from Ref. 31, corrected for the response of the detectors used in these experiments. The result was an attenuation factor as a function of channel number i to be multiplied by the expected asymmetry parameter A_1. The middle dashed curve in Fig. 8 includes this attenuation as well as the p-capture attenuation. As expected, scattering is more important at low energies, since the scattering cross section is larger at low energies and since radiation from higher energies is scattered to low energies. Final interpretation of the data shown in Fig. 8 is discussed in Chap. V.

Interpretation and Summary of ^{119}Sb IB Experiments

After corrections for p-capture IB and for scattering have been applied, the asymmetry data still deviate from the theoretical curve, especially at intermediate and low energies. Several possible explanations for this may be advanced:

1] The thermometry might have been inaccurate or the alloy preparation might have given the wrong internal field. This would not explain the energy dependence of the asymmetry. Furthermore, the consistency of the results among four different alloys with Sb concentrations varying by a factor of five argues strongly against bad alloys (which would give incorrect and variable hyperfine fields). The hf field for Sb in Fe has been measured in several laboratories[33-35] with consistent results. The nuclear dipole moment of ^{119}Sb has also been measured with good accuracy.[36] Finally, the fit of the data to a temperature-dependence curve of the correct form indicates that the temperature scale is accurate to within experimental statistics. (Fig. 7)

2] Scattering corrections might have been greater than those allowed for. This is possible, since scattering in the heat link and apparatus walls was neglected. Most of the deviation from scattering would be expected to occur at rather low energies, however, as a comparison of the upper and middle dashed curves in Fig. 8 shows. As can be seen, the deviation of the asymmetry from theory is largest at intermediate energies where scattering should be small. However, if we assume that the attenuation due to scattering is about 50% greater than was calculated taking only the flux-trapping ring into consideration, we obtain the

bottom dashed curve in Fig. 8, which is in good agreement with the three lowest-energy experimental points.

3] Background corrections might have been significant. This hypothesis must invoke background radiation of intensity of the order of 30% of the IB in the total range from 200-350 kev. Also the relatively good agreement of the observed spectrum shape with that obtained by previous workers (Fig. 6) suggests that no large background radiation is present within the source. There is some evidence of deviation near 325 kev., which might explain the particularly low point at that energy in Fig. 8. If a sufficient isotropic background is subtracted from the intermediate energy region to give overall agreement with the bottom theoretical curve in Fig. 8 (triangular data points), the new spectrum given by the triangular points in Fig. 6 results. This can be compared with the dashed spectrum in Fig. 6, which is the spectrum of Ref. 31 renormalized to the new 150 and 175 kev. data points. The subtracted background is shown below in Fig. 6. The agreement of the spectrum shapes in this case is not materially worse than in the uncorrected case; in fact, in the 300-400 kev. region it is improved. The subtracted background is about the right magnitude to be attributable to backscatter from the 1.4 Mev. ^{40}K line which is always present in the room; the energy, however, seems too high since the ^{40}K backscatter peak usually is centered around 100 kev. (It might be pointed out that a temperature dependent background, i.e. a background gamma ray from an impurity source which was polarized along with the ^{119}Sb, could not be invoked to explain the deviation in Fig. 8, since such a gamma ray would show an anisotropy which was symmetric

backward and forward, due to parity conservation; this would enhance the IB asymmetry in one counter and attenuate it in the other. The observed deviation, in contrast, is an attenuation in both counters.)

4] Gain shifts or other systematic effects might have been present in the counting system. This possibility can be ruled out on two grounds: first, such an effect should be largest at the high energy end of the spectrum where the intensity is lowest--a slight shift there would make much more difference than in the 250 kev. region where the spectrum is flatter and gain shifts are relatively smaller. Second, the roles of the counters were reversed by magnetizing alternately in opposite directions. The data at $\theta = 0$ and π with the field in both directions agreed well, which implies that systematic counter effects were probably small, since they would not be expected to be identical in the two counters and thus would show up upon reversal of the roles of the counters.

5] The actual energy dependence of the IB asymmetry might be larger than expected theoretically. Several authors [37, 38, 23] have pointed out that the K-capture IB asymmetry should be energy independent. On the other hand, Martin and Glauber in Ref. 23 mention that the polarization (and hence the asymmetry) of K-capture IB is somewhat reduced by relativistic effects (the mixing of p(1/2) states into the s-state wavefunction) and that this effect is energy dependent. An evaluation of their formula for the case of ^{119}Sb shows that this reduction in polarization is of the order of 1% at energies above 75 kev. and becomes significant only at rather low energies (below 50 kev.). The present experiments do not include those energies (because of interference from the tail of the

24 kev. gamma ray of ^{119}Sn) and their sensitivity is not sufficient to detect the ca. 1% reduction of the asymmetry at higher energies. Thus it may be concluded that unless the theory is grossly in error (which seems unlikely in view of its success in predicting spectrum shapes and branching ratios), this explanation cannot account for the observed deviations.

In summary, it seems likely that a combination of 2] and 3] is responsible for the observed energy dependence of A_1 and for the reduction of the value of A_1 below the theoretical prediction in the integral-energy measurements. If only the four highest-energy points are used to calculate the value of A_1, we obtain[39]

$$A_1 = +1.001 \pm .093$$

in agreement with the predicted value.

First Forbidden Beta Decay Experiments, Introduction

In order to measure nuclear matrix elements in a first forbidden decay, one requires a nucleus for which neither the ξ approximation nor the B_{ij} (unique) approximation holds. This may be determined by measurement of the electron spectrum shape. In the $1^- \rightarrow 0^+$ and $1^- \rightarrow 2^+$ decays of ^{170}Tm, ^{186}Re, ^{188}Re, and ^{210}Bi, departures from the statistical shape (but not the unique shape) have been observed in the beta spectra.[40-44] A number of experiments have been performed on these four isotopes with the intention of determining the nuclear matrix elements, both to test the CVC theory and for the intrinsic interest of the matrix elements themselves. Experiments performed on the two Re nuclei include spectrum shape measurements,[43,44] beta-gamma directional correlations,[45,46] beta-gamma circular polarization correlations,[47] and angular distributions from polarized initial nuclei.[48,49] Electron polarization measurements have also been made.[50]

Another nucleus which exhibits decays of the $1^- \rightarrow 0^+$ and $1^- \rightarrow 2^+$ types and which has favorable properties for nuclear polarization is ^{194}Ir. These decays have not been as thoroughly studied as the Re decays, although spectrum shapes have been measured[51] and beta-gamma angular correlations observed.[52] The statistical shape was found for both principal beta branches in Ref. 51, indicating that the ξ approximation holds for these decays. However, because of the well-known lack of sensitivity of shape measurements and the general lack of experimental work on this isotope, it seems that angular distribution measurements from polarized nuclei of ^{194}Ir are justified. In the following chapters, experiments on the angular distri-

butions of beta particles from the decays of ^{186}Re, ^{188}Re, and ^{194}Ir polarized in iron at low temperatures are described.

Experimental Cryostat

The cryostat used for the beta decay experiments was similar to one described by Barclay.[53] (See Fig. 9.) The outer liquid helium dewar was made from 10" dia. aluminum tubing, with a fibreglass inner wall and mylar "superinsulation" between. No liquid nitrogen heat shield was used. The dewar held about 15 l. of liquid when filled and boiloff rates were approximately 1 l./hr. A 46 koe. superconducting solenoid was suspended in the outer helium space. The 1° helium bath was made from thinwall stainless steel tubing, 4-1/2" O.D., and was insulated with a copper and stainless steel vacuum jacket. Using a 1200 l./min. Kinney booster pump, one could reduce the bath pressure to 50-60 microns Hg, or about 0.95° K.

The experimental chamber was made from stainless steel tubing. A large (4" O.D.) section contained the cooling salt pills while the source and the beta particle detectors were in a 2" O.D. tail section. Around the source chamber was the polarizing magnet, a superconducting helmholtz pair with a coil constant of 200 oe./amp. and a maximum current of 25 amp. The polarizing magnet was in the 1° helium bath. The cooling salt pills consisted of two chrome alum slurries which cooled the heat shield, and a main cerium magnesium nitrate(CMN) slurry for cooling the sample. (See Appendix III). A bundle of several thousand #40 copper wires potted in epoxy formed the heat link from the source foil to the CMN slurry; at the upper end the wires were left free of epoxy and were mixed into the slurry, while at the lower end the bundle was soldered with Bi-Cd eutectic to a

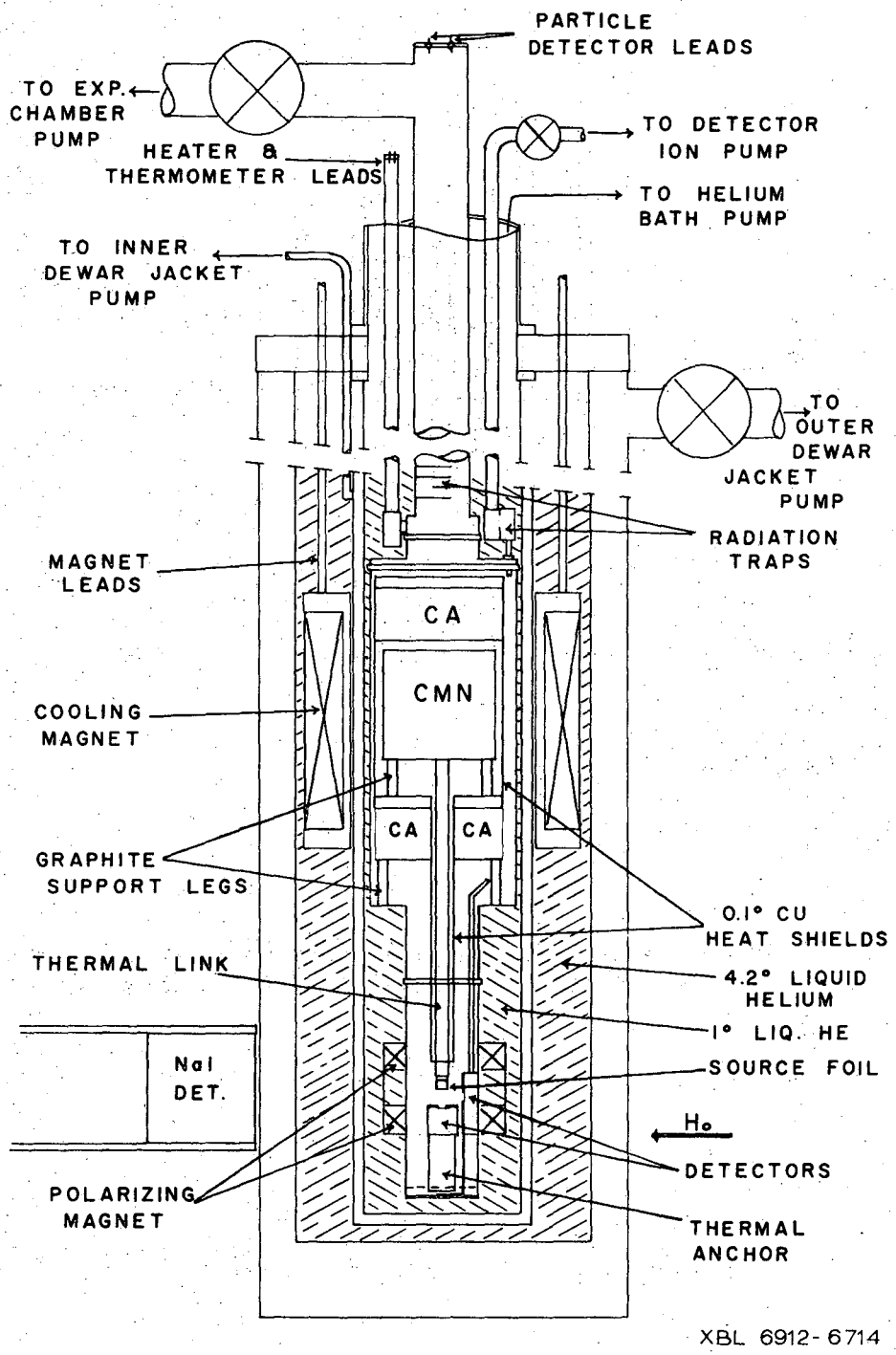

Fig. 9. Schematic diagram of the cryostat used for the first forbidden beta decay nuclear polarization experiments.

small copper plate to which the wire source holder was attached. The volume of CMN slurry was 375 cc. with about 60% filling factor. The copper-to-slurry contact area was approximately 1600 cm^2 and the heat link was 9" long outside the slurry container. The entire assembly of heat link and CMN pill was surrounded by a copper heat shield cooled by CA slurries, with only the source holder projecting out. The lowest temperatures obtained with this apparatus were about 4.2 mdeg. K., and typical warmup rates were ~ 1 mdeg./hr.

Source Holder

Since scattering of the beta particles in the source foil and source mount is a serious problem in these experiments, an effort was made to reduce the mass of both and to design them in such a way as to minimize scattering of the particles into the detectors. The source foils were rolled to thicknesses of 2-3 microns, which was about five times thinner than those used by previous workers.[48,49] The sources were supported on two edges by #20 copper wires, which formed a support frame and thermal contact to the main heat link. In order to insure uniform heat distribution, the backs of the source foils were coated with 10 microns of copper by vapor deposition prior to attachment to the wire supports by Bi-Cd solder. Finally, the activity was confined to a central rectangle of 3x3 mm (the source foils were 10x6 mm overall) so that the particles which were scattered by the support system would have to be scattered at angles near 90° to reach the detectors, since backscatter cross sections are small at right angles to the incident electron's path. Fig. 10 shows a full size view of the source and beta counters.

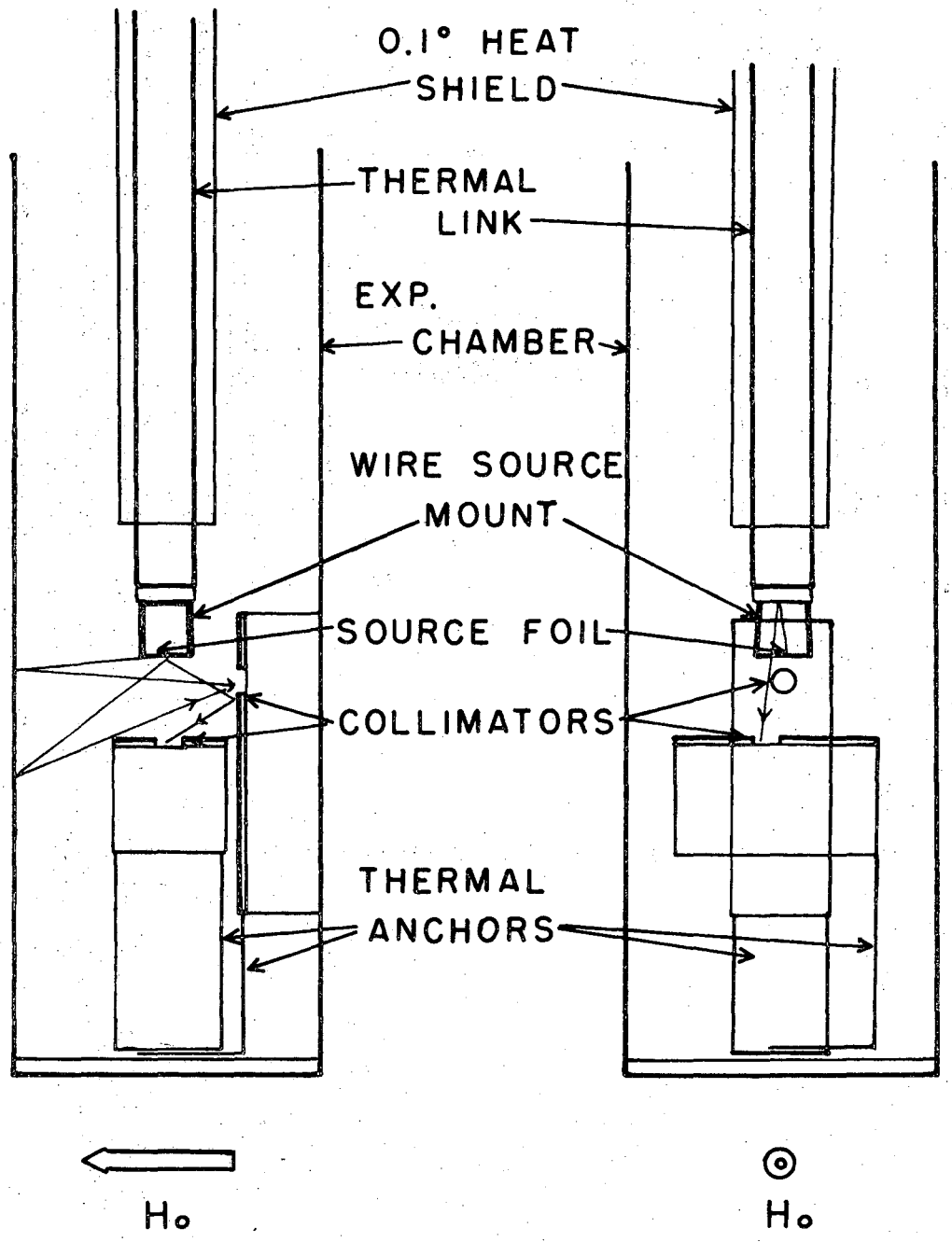

Fig. 10. Full-scale views of experimental chamber, front and side.

Radiation Detectors

The gamma radiation detectors used in these experiments were similar to those described in Chap. III, except that the lead background shields were omitted.

The beta particle detectors were believed to be of primary importance to the results of these experiments. Obtaining counters with good efficiency, good energy resolution and linearity, and stability was thus to be desired not only for the immediate ends of the present work but also for general future use. Accordingly, considerable effort was expended in a counter development program, which was conducted with the cooperation and assistance of the LRL semiconductor development group.

Particle detectors used in previous experiments on beta particles from polarized nuclei have been either scintillators (usually anthracene)[48] or semiconductor surface barrier detectors.[7,49] Anthracene scintillators have the disadvantage of requiring a light piper from the exterior of the cryostat where the photomultiplier is located to the detector inside the experimental chamber. This introduces mechanical and vacuum problems, heat leaks, and poor resolution. For these reasons anthracene scintillators were not considered for the present experiments.

Surface barrier detectors have much better resolution and require only a single wire connection to the outside of the cryostat. They are able to operate at temperatures down to 1° K., although their operation at such temperatures is not well understood and consequently unreliable. Basically, the detector consists of a block of silicon or germanium with electrodes (usually a deposited film of gold or aluminum) on the front and

back surfaces. A barrier layer exists between the front electrode and the bulk material, either because of oxidation of the surface layers during construction of the detector, or because an impurity such as phosphorous was diffused into the front of the block (diffused junction detector). The barrier has very high resistance (it may have the properties of a diode in which case it is reverse-biased) so that when a voltage is applied between the two electrodes, most of the voltage drop appears across the barrier layer, producing an intense electric field which sweeps charge carriers out of the region around the layer and creates a "depletion zone". It is this zone which detects particles: when an ionizing radiation enters the zone, it loses energy by creating electron-hole pairs which are swept out rapidly by the field and produce pulses of current at the electrodes. If the thickness of the depletion zone is equal to the average stopping range in the material for a particle of energy E, the detector is said to have a sensitive depth of E for particles of that type. The sensitive depth may be increased by increasing the applied bias voltage and thus the thickness of the depletion zone, until surface conduction or avalanche breakdown begins at some limiting bias voltage. For heavy particles such as alpha particles or protons the stopping ranges are short and several-or-many-Mev. sensitive depths are obtainable. Electrons, however, have much longer stopping ranges (2.4 mm/Mev. in Si, 1.3 mm/Mev. in Ge) so that application of sufficiently high bias voltages to give even one Mev. sensitive depth is usually not possible. To be sure, particles of energies exceeding the sensitive depth are detected,[54] but with reduced efficiency and resolution and with a complex response function.

No experiments have been done at low temperatures with monoenergetic electron sources to determine the exact detection characteristics for particles exceeding the sensitive depth of the detector.

The effective thickness of the depletion zone can be increased by drifting lithium into the semiconducting material under the influence of an electric field.[55] The lithium ions move in such a way as to electrically compensate for the impurity charge carriers present in the material and allow the production of deep depletion zones by relatively small applied bias voltages. Trapping of the charge carriers produced by an ionizing radiation can occur, however, and when a thick depletion zone exists, it may become a serious problem. The trapping increases at low temperatures and causes a pratical low temperature limit to the operation of the detector; thus thick detectors and low temperature operation are in some measure incompatible goals. Furthermore, the drifted lithium in germanium is unstable at room temperature, and such detectors must be kept below -50° C. most of the time. Lithium drifted germanium detectors are also very sensitive to surface contamination and must be kept in high vacuum to avoid breakdown problems. Lithium drifted silicon detectors are not suitable for work of the present type for two reasons: because of the lower density of silicon, the detector would have to be much thicker to have the same sensitive depth; and secondly, the practical low-temperature limit to Li-Si detector operation is rather high (~40° K.) compared to that for Li-Ge.(<17° K.; see Ref. 57.)

Numerous experiments were tried on both n- and p-type silicon and germanium surface barrier detectors. In general, both types of silicon

gave usable detectors but only the n-type germanium could be used. All the detectors would detect particles at 1° K. and some had fairly good resolution for alpha particles. Germanium would in general support much smaller bias voltages (typically less than 10 v. compared to more than 100 v. for silicon). However, none of the surface barrier detectors tested had very good resolution for ^{137}Cs conversion electrons (624 and 656 kev.) and many detected only a broad hump for the ^{137}Cs spectrum. Lithium drifted germanium detectors were also tried and found to give excellent resolution for all ^{207}Bi conversion electrons, even out to 1.68 Mev. The latter detectors would support over 600 v. bias if kept clean. However, they would not operate satisfactorily below about 16° K. Thus for operation in a cryostat they would require enclosure in a vacuum tight container in which they could be thermally isolated from the low-temperature components of the experiment.

In spite of the more difficult operation, it was felt that the advantages of 2.5 Mev. sensitive depth, 5 kev. resolution at 1 Mev., good energy linearity and long term stability were sufficient to justify the use of lithium drifted detectors. A set of holders was constructed to meet the requirements outlined above.

Detector and Holder Construction

The lithium drifted detectors used in these experiments (Fig. 11) were of the $P^+I\ N$ type. A block of germanium cut from a single-crystal ingot with a diamond saw is polished and a lithium (N) electrode is diffused into one surface. Lithium is then drifted in an electric field to the opposite face of the block. The lithium compensates the impurities

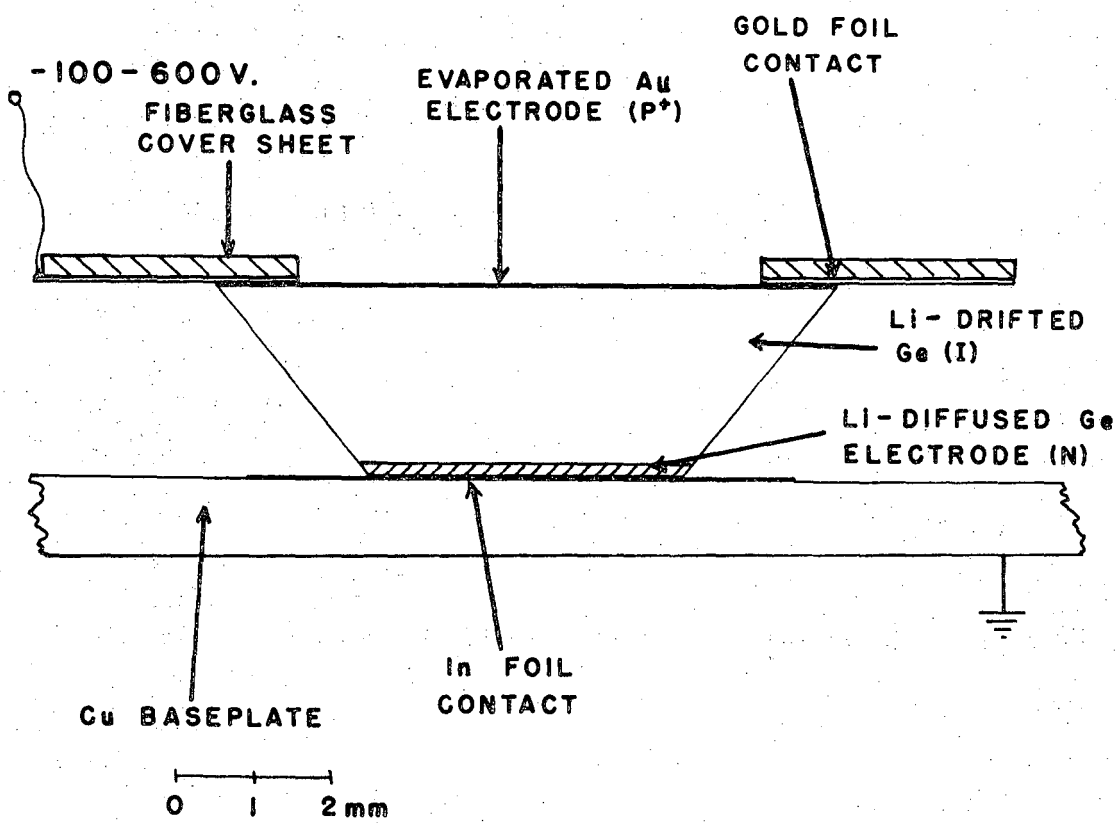

XBL 6912-6716

Fig. 11. Cross section of Li-Ge beta detector mounted on base.

in the germanium to give the equivalent of very pure semiconducting material (I). A gold (P^+) electrode is vapor deposited on the front surface of the block. At this stage the detectors may be stored at dry ice temperature for months without apparent deterioration. The above steps were carried out by the LRL semiconductor development group. When the detectors are to be used, they are etched to remove surface impurities and damaged material as follows: a piece of plastic electrical tape is applied to the gold surface and pressed down carefully. The other end of the tape is attached to a plastic stirring rod which serves as a handle. The etch consists of 1 part conc. HF, 1 part fuming HNO_3, and 7 parts conc. HNO_3 by weight and is used at room temperature. The detector is gently agitated in the etch for 1-2 min. and then removed and quickly washed in high purity methanol. After several rinses in methanol, the detector is separated from the tape, given a final rinse, and dried in a stream of N_2 gas. It is then mounted immediately in the holder. After assembly of the holder, detectors have been kept in an evacuated dessicator for up to one hour without requiring re-etching.

The holder (Fig. 12) serves several purposes: as a support and electrical contact for the detector, as a vacuum chamber allowing the detector to be protected from surface contamination at all times, and as a thermal shield which allows the detector to be heated to its operating temperature without warming its surroundings. The outer housing was made of .025" sheet copper with silver soldered joints; over the detector it had a 6 mm dia. hole which was covered with a 1 mg/cm^2 thick sheet of aluminized mylar glued in place with Epon 826 epoxy. The removable end plate was of

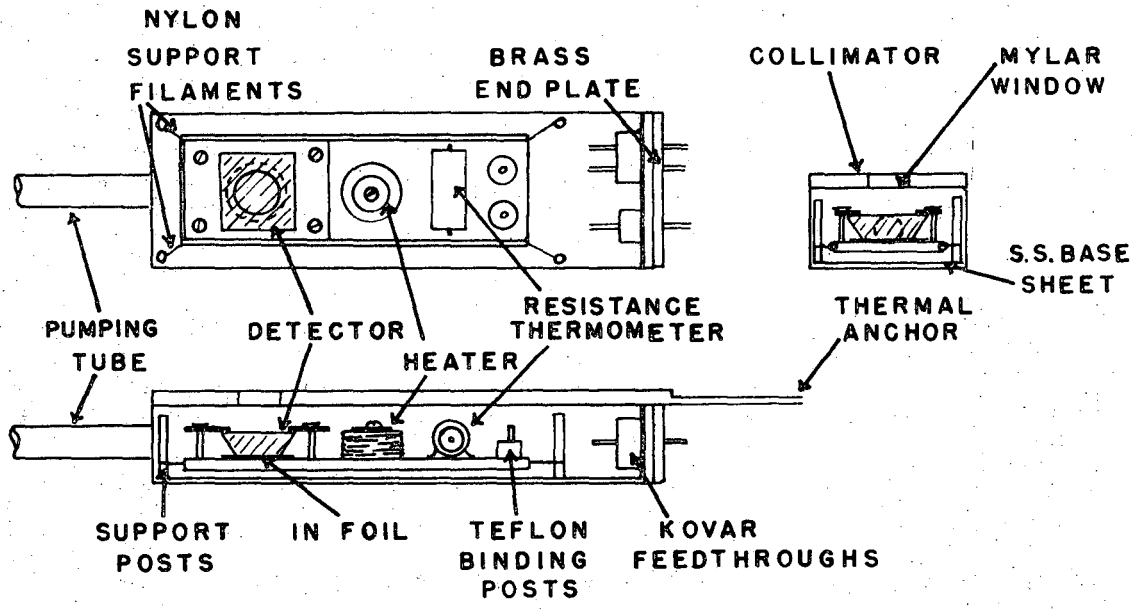

Fig. 12. Top, end, and side views of axial beta detector holder, about 1.2x actual size. The lead wires are omitted for clarity.

.065" thick brass and was silver soldered to the .020" stainless steel base sheet. The end plate contained the kovar-ceramic feedthroughs which carried the electrical leads; these were soldered into the plate with Pb-Sn solder. The end plate was soldered into the housing with Wood's alloy for final closure of the assembly. Attached to the base sheet were four .040" dia. stainless steel posts which served to anchor the .005" nylon monofilaments which supported the detector base itself. The base was of .040" copper and carried a heater (6' of #40 formvar insulated manganin wire wound in a coil and potted in epoxy, resistance 175 Ω) and a copper sleeve into which the resistance thermometer was glued. The detector was held in place by a sheet of 1/64" thick fibreglass with a sheet of .002" gold foil on the underside, which made contact with the gold electrode on the detector surface. The cover sheet had a 6 mm dia. hole over the center of the detector and was held down by four 0-80 brass screws tapped into the base plate. Electrical leads to the detector, thermometer, heater, and ground were made of .002" thick x .020" wide niobium ribbon, spotwelded at the ends to short lengths of gold wire. The niobium was presumably superconducting during detector operation and thus minimized heat leaks from the detector base to the housing. The housing was evacuated through a 1/8" dia. thinwall stainless steel tube silver soldered into one end. Over the front of the holder was a 1.5 mm thick copper plate which had a 4 mm dia. circular collimator opening above the window in the holder. The collimator was soldered with low-melting In-Sn solder to the housing, and an extension made of .025" copper reached to the bottom of the experimental chamber where it was Ga-soldered to a

baseplate in contact with the 1° helium bath. Experiments with externally mounted resistance thermometers showed that the detector base could be heated to 20° without warming the housing to more than 1.2°. Heating rates were about 1.5 mw and thermal equilibrium was established in about 5 min. The temperature of the detector base was then constant to ±0.2° over 12 hrs. or more as indicated by the detector thermometer, which was a 131 Ω 1/4 w. Allen-Bradley carbon resistor. Power was supplied to the detector heaters from 1.35v. mercury batteries equipped with digital voltage dividers and standard resistors for monitoring the heater current. No increase in 1° helium bath operating pressure could be attributed to the detector heaters.

Particle Detector Leads and Electronics

Since the system of detector and leads behaves towards the external circuit like a capacitor, the voltage of pulses produced by a particle of energy E is given by $V = qE/(C_d+C_x) \cdot \eta/\varepsilon$ where C_d is the detector capacitance, C_x is the stray capacitance in the leads and external circuit, η is the charge collection efficiency for pairs of charge q, and ε is the energy required to produce a charged pair in the material. Clearly in the interest of maximum pulse height one wishes to minimize C_x. In the present apparatus, the detector leads were .002" dia. stainless steel wires streched down the central (1-1/2" dia.) pumping tube between two kovar-glass feedthroughs. Connections to the preamplifiers at the top were by means of BNC connectors. At the bottom, #50 copper wires sandwiched between two pieces of mylar tape were used to connect the detector holder leads to the lower ends of the stainless steel wires.

A transistor socket was used as a connector to allow disconnection of the leads from the detector holders. The total lead length was about 50" and the lead capacitance was 35 pf.

The pulses from the detectors were preamplified by charge-sensitive FET preamplifiers operated at room temperature. Second stage amplification was by high-rate linear amplifiers. Output pulses from the gamma-detector preamplifiers were amplified by linear amplifier systems like the one described by Goulding and Landis.[56] Pulses from the two beta detectors and the two gamma detectors were fed into a four-input router which was connected to a Scipp 1600 channel analyzer. Each spectrum occupied 400 channels. Counts were timed using the Scipp internal live timer, and the data were recorded on magnetic tape at the end of each count. The counts were 5 or 10 minutes long.

Particle Detector Response

The response of the particle detectors to both beta particles and gamma rays was determined by using a ^{207}Bi calibration source. Since these detectors have a thick depletion zone, their efficiency for detecting gamma rays is relatively higher than that of surface barrier detectors, for example. The apparent efficiency for gamma rays is further increased by two factors: the collimators used for the beta particles are virtually transparent to gamma rays of > 500 kev. energy, so the effective counter area is larger for gamma rays; and also, a large fraction (ca. 30%) of the incident beta particles is backscattered from the detector, which reduces the apparent efficiency for these particles. The net effect is that at 1 Mev. energy, the apparent efficiency for gamma rays is about half that

for beta particles. Most of the gamma ray pulses occur in the Compton background, since the Compton cross section of germanium in the 1 Mev. region is much greater than the photoelectric and pair production cross sections. A typical ^{207}Bi spectrum is shown in Fig. 13. The expected and observed relative intensities of the conversion electron lines are shown in the table. The relatively high gamma ray detection efficiency is unimportant unless background gamma rays are present in the beta spectrum. This question is considered in Chap. VII under Background Corrections.

The pulse height and resolution of the detectors were measured as functions of applied bias voltage and temperature (See Fig. 14). At low temperatures the trapping of charged pairs by impurities (probably the Li and Ga dopants added to the germanium in the detector) becomes significant and the pulses produced become very long and low as a consequence. When this occurs, the pulse height and resolution of the detector deteriorate rapidly. Four of these detectors were tested, and all had critical temperatures near 16° K. with bias voltage in the range of 75-300 v. (corresponding to fields of 300-1200 v/cm). Above this temperature the pulse height and resolution were constant within a few percent (resolution of the whole system was 5 kev. at 1 Mev., corrected for scattering in the source foil and detector windows.). Below the critical temperature the pulse height and resolution became rather poor in spite of increased bias voltages up to 600 v. In general, the detector characteristics were approximately constant above about 75 v. bias, so they were usually operated at 100-150 v. to minimize the possibility of breakdown, although they

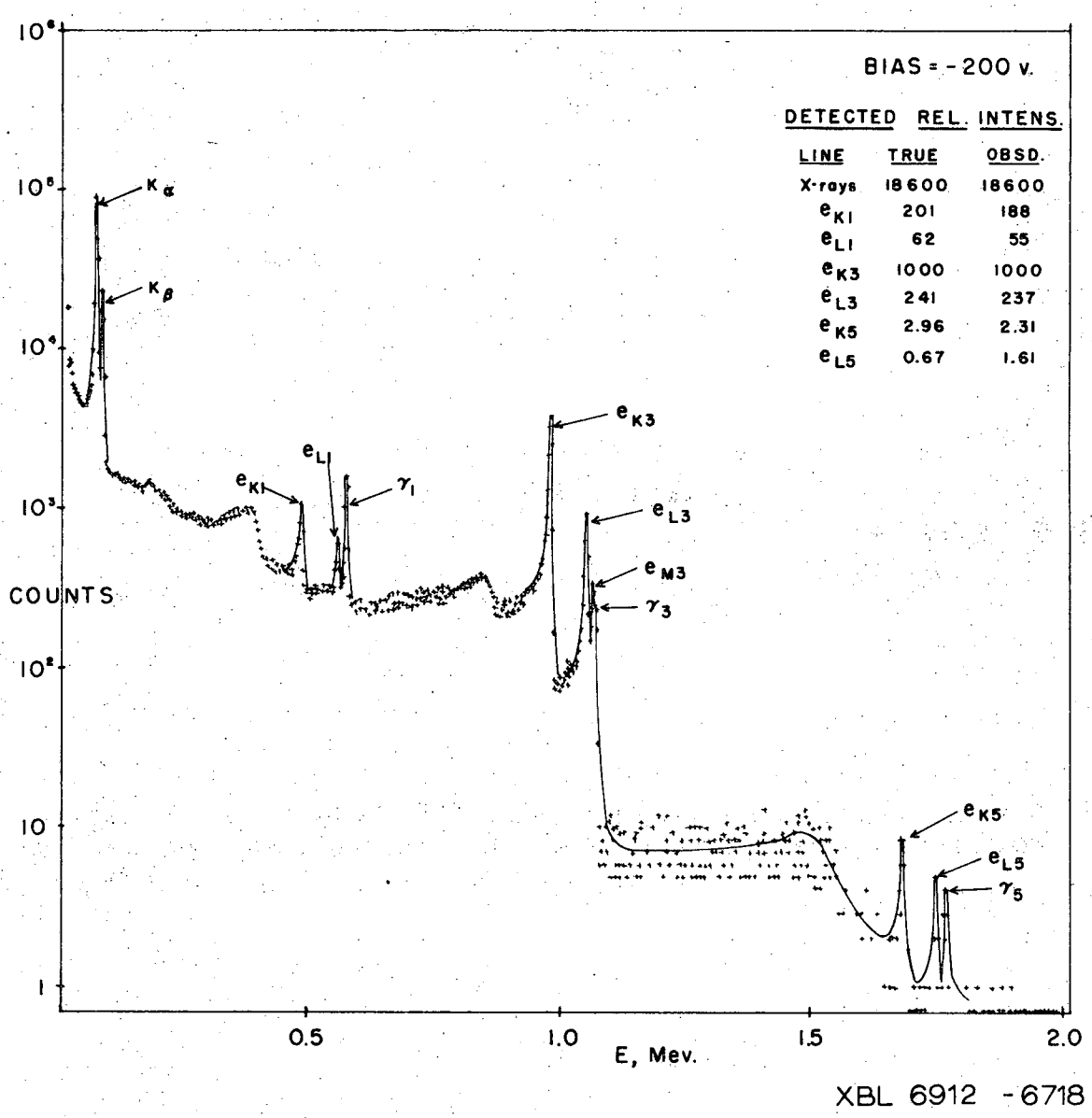

Fig. 13. Spectrum of ^{207}Bi taken with axial beta counter at 16.5° K. Polarizing magnetic field off. The table shows expected and observed intensities for the electron lines and x-rays.

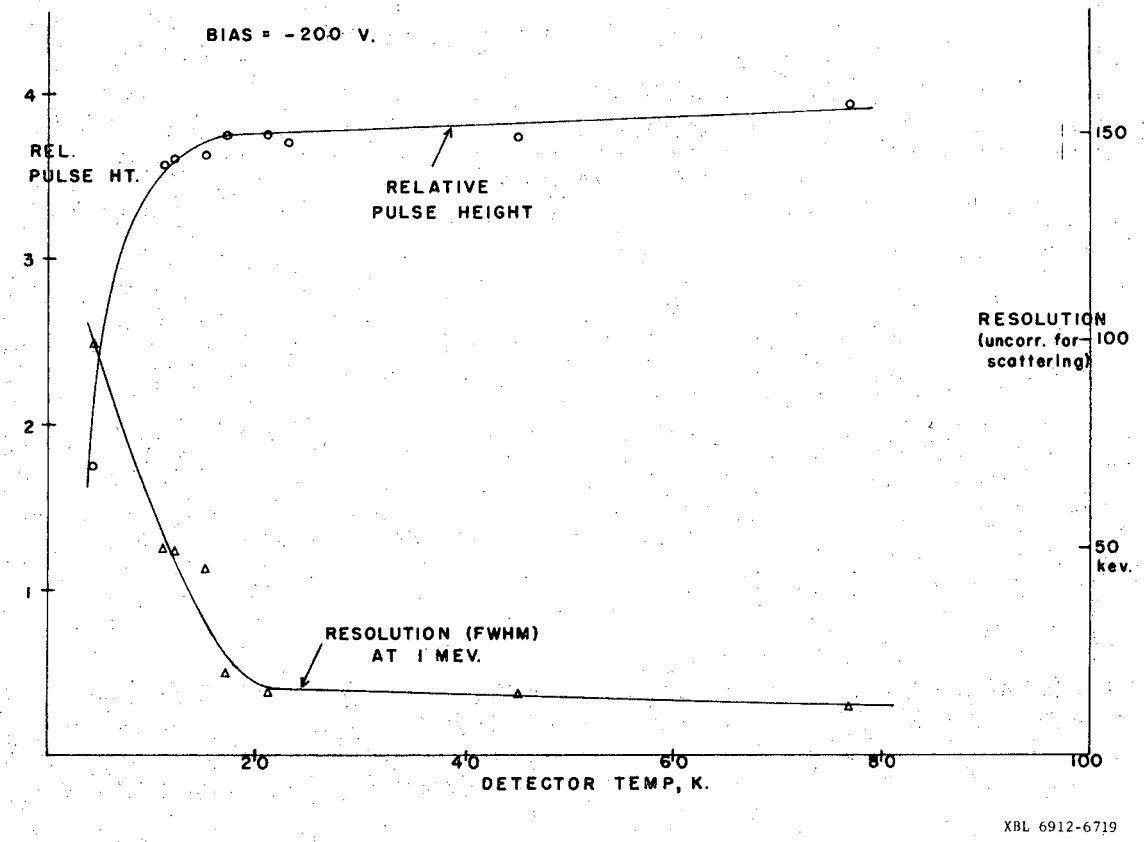

Fig. 14. Pulse-height and resolution of the axial beta detector as functions of detector temperature. Measured using the 975.6 kev. conversion line of ^{207}Bi. (Resolution values are uncorrected for scattering and are only approximate.)

would actually support more than 600 v.

Recent work at Chalk River[57] has shown similar behavior for Li-Ge detectors counting gamma rays. Two differences exist between the present findings and those of Ref. 57: in Ref. 57, the detectors tested had much thicker P layers than those used in this work; and in Ref. 57, a considerable dependence of detector characteristics on bias voltage, up to fields of 3000 v/cm (corresponding to 750 v. applied bias for the detectors used in this work) was found. In fact, by applying voltages giving fields of this magnitude, the authors of Ref. 57 were able to operate their detectors successfully at temperatures down to 8° K. and suggest that even lower-temperature operation may be possible. No such large dependence of characteristics on bias voltage was found for the present detectors, although the experiments were not exhaustive. Clearly, operation at lower temperatures is desirable if possible for this type of work.

Beta Decay: Experimental Procedures and Data Analysis

Source Preparation

Fig. 15 shows the decay schemes of the three isotopes used in these experiments. All three parent states may be prepared by neutron capture from the corresponding stable nuclei. Enriched samples of ^{185}Re, ^{187}Re, and ^{193}Ir were obtained as powdered metal from Oak Ridge. Their purities were as follows: ^{185}Re, 96.66% (+3.34% ^{187}Re); ^{187}Re, 99.22% (+0.78% ^{185}Re); ^{193}Ir, 97.29% (+2.71% ^{191}Ir). In each case a weighed amount of the isotope was placed in a small iron crucible which was then melted in H_2 atmosphere in a quartz tube. The cooled ingots were hammered to about 30 microns thickness and annealed for two hours at 900° C. in H_2, then rolled to a final thickness of about 2.5 microns (2 mg/cm^2). Two alloys of each of the Re isotopes were prepared, one each using 99.9% Armco iron (spectrographic analysis showed the principal impurities to be nickel and copper), and one each using 99.99% iron having as principal impurities Co, Si, Ni, and Sn. One alloy of the ^{193}Ir was prepared using the Armco iron. Pieces of each foil 10 x 6 mm were cut and sandwiched between pieces of .005" Cd foil having 3 x 3 mm square holes in the centers. The sandwiches were sealed in quartz bulbs with a partial atmosphere of H_2 and were irradiated 1 hr. each in a flux of 2.5 x 10^{14} thermal neutrons/sec-cm^2. Because of the relatively small cross sections for neutron capture by iron isotopes and because ^{55}Fe decays by electron capture and thus has only low energy x-rays and weak IB, no problem of interference from activation of the iron arises. The major iron radiations are from ^{59}Fe, which emits gamma rays at 1.1 and 1.3 Mev. and beta particles below 500 kev. (except

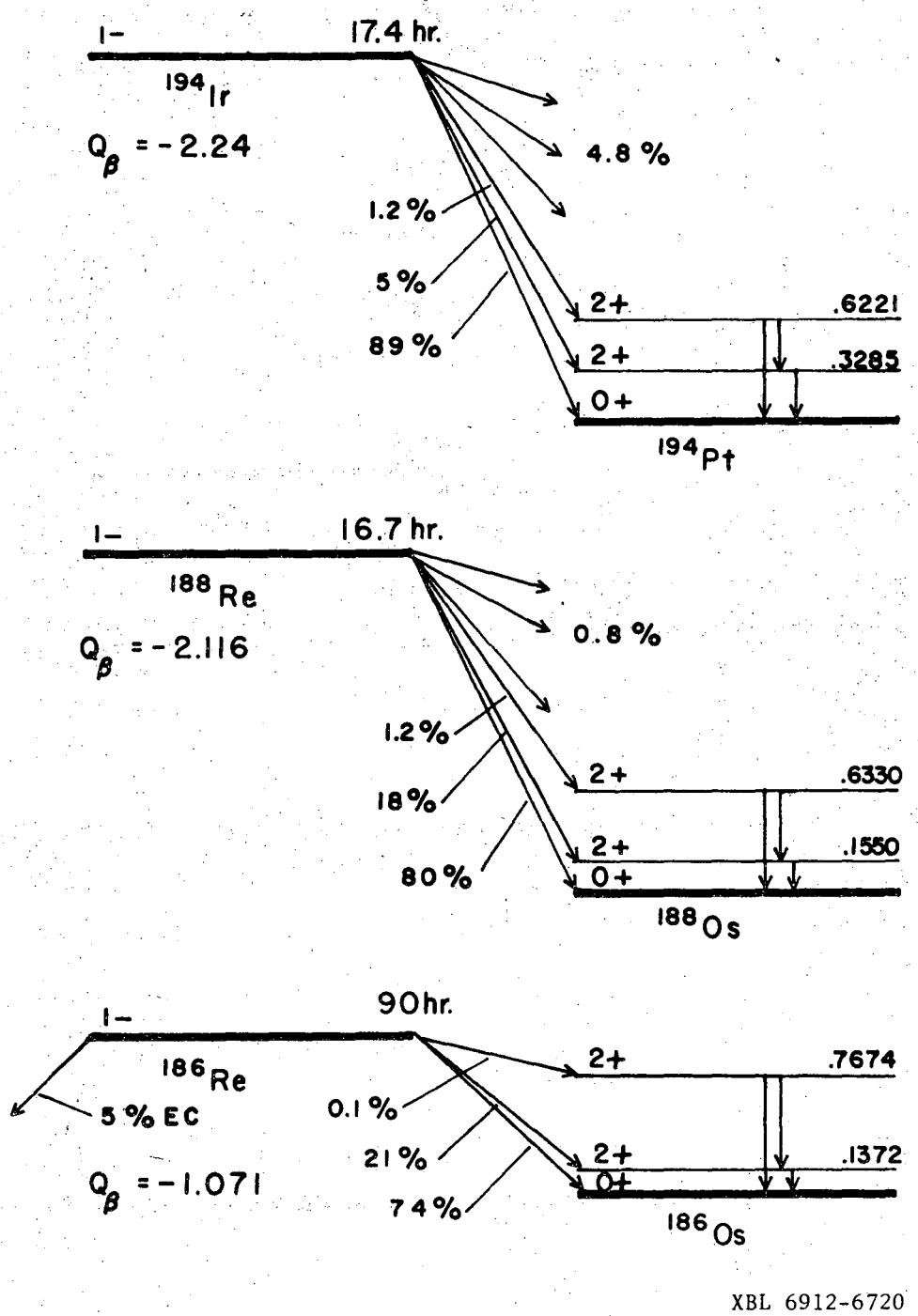

Fig. 15. Relevant parts of the decay schemes of the isotopes used in the first forbidden beta decay experiments.

for a very weak beta branch with 1.57 Mev. endpoint). This activity presents no potential interference with the ^{188}Re and ^{194}Ir high energy beta branches which were observed in this work. The iron gamma rays might give some background under the ^{186}Re beta spectrum, but it would be very weak since the decay rate ratio (^{186}Re/^{59}Fe) was greater than 500:1 in all cases. This question is discussed later under Background Corrections.

The purpose of the Cd foil sandwich during irradiation was to permit neutrons to enter the alloy foil only in the central 3 x 3 mm spot. Thus no activity would be generated near the source foil mounting wires which were soldered to the edges of the foils. Because of neutron diffusion, a certain amount of activation occurred outside the central spot. After the foils were used for the nuclear polarization experiments, autoradiographs were made using x-ray film. These showed a well defined square of high intensity in the center of each foil, surrounded by an area of less activity, as expected. Fig. 16 shows a profile of one of the autoradiographs made with a microdensitometer (transverse and longitudinal sections). The relative activity of the central spot and the surrounding area can be determined from such a profile; this information was needed to calculate the solid angle corrections.

After irradiation, the foils were removed from the quartz bulbs and the Cd foil sandwiches and were washed several times in dilute HF to remove surface oxidation and activity. They were then annealed at 900° C. for six-ten hours and cooled slowly over an eight hour period. Before mounting in the nuclear polarization apparatus, each foil was coated on one side with about 10 microns of copper by vapor deposition. The copper

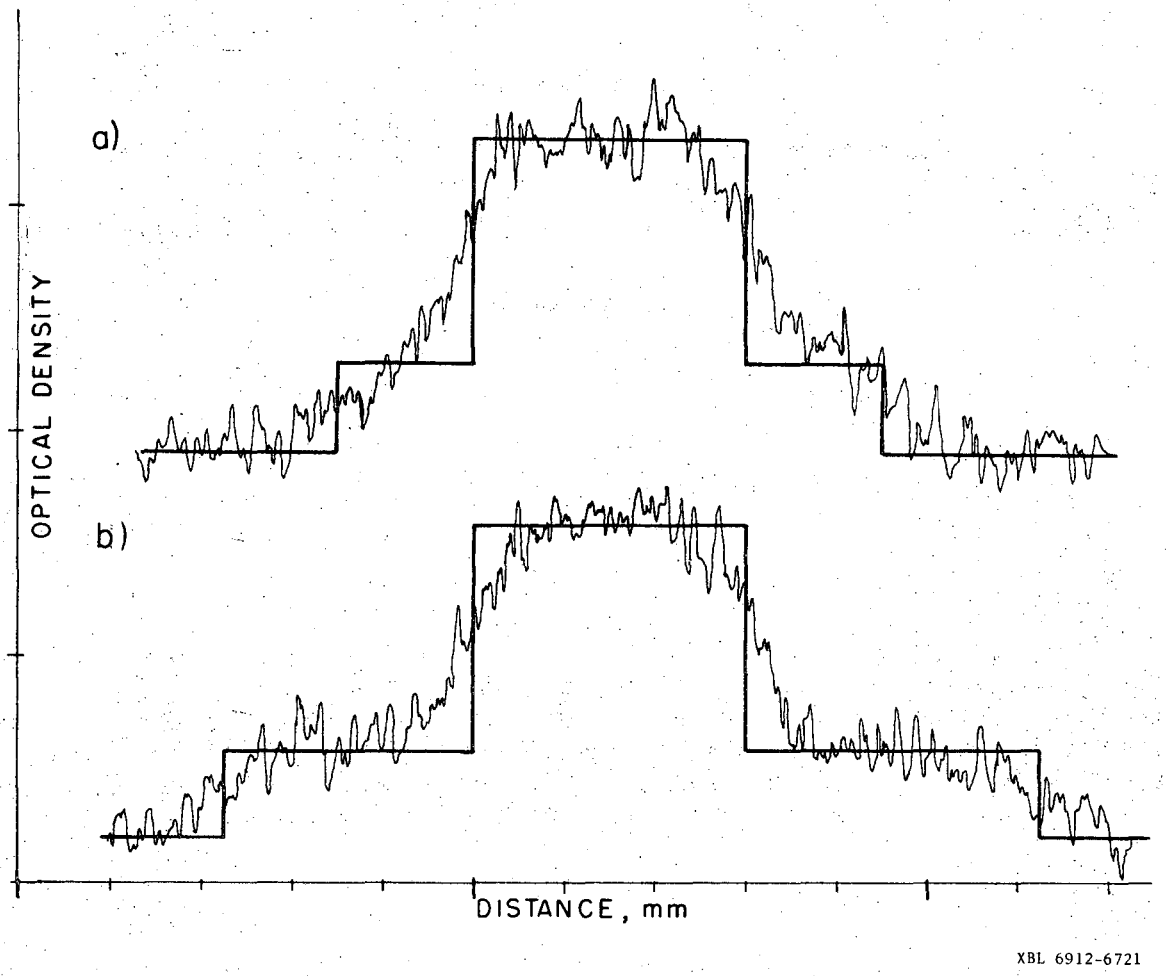

Fig. 16. Densitometer tracings, a) transverse, b) longitudinal, of the autoradiograph of source #8. The irregularities are due to granularity of the x-ray film. The heavy lines show idealized profiles used for solid angle calculations. Some smearing of the measured profiles occurs because of the finite thickness of the film emulsion and film-source separation.

layer was soldered at the edges to the support wires and helped to maintain a uniform temperature over the source foil. (See Thermometry section.)

Table I gives a summary of the details of source preparation.

Table I: Source Preparation

Solute	Concentration	Host	Sources Produced
^{185}Re	0.165 at. %	99.9% Fe	#1,2,3
^{187}Re	0.325 at. %	99.9% Fe	#4,5
^{193}Ir	0.192 at. %	99.9% Fe	#8
^{185}Re	0.50 at. %	99.99% Fe	#6
^{187}Re	0.77 at. %	99.99% Fe	#7

Treatment of Data and Corrections Applied

A number of corrections may be applied to the raw electron angular distribution data before the desired angular distribution coefficients are obtained. In this section, the analysis of the corrected data for these coefficients will be described. In the sections which follow, certain of the corrections will be discussed in more detail.

The angular distribution of the electrons from a first forbidden beta decay is given by Eq. 12, Chapter II. The anisotropy, or relative counting rate as a function of angle theta between the detector and the Z-axis, is given as a series in Legendre polynomials of argument cos θ

and having coefficients given by the orientation parameters B_k and by sums of Racah coefficients and particle parameters $b^{(k)}_{L,L'}$. It is the particle parameters which one desires to determine. Eq. 12 may be rewritten for the cases of $1^- \to 0^+$ and $1^- \to 2^+$ decays which are of interest here:

Eq. 13a
$$W(1\to 0,\theta) = 1 - B_1P_1(\cos\theta)\{b^{(1)}_{1,1}/b^{(0)}_{1,1}\} + B_2P_2(\cos\theta)\{b^{(2)}_{1,1}/b^{(0)}_{1,1}\}$$
$$= 1 + B_1P_1A_1(0) + B_2P_2A_2(0)$$

Eq. 13b
$$W(1\to 2,\theta) = 1 + B_1P_1(\cos\theta)\frac{\{b^{(1)}_{1,1} - 3/\sqrt{5}\, b^{(1)}_{1,2} + 1/\sqrt{5}\, b^{(1)}_{2,2}\}}{2[b^{(0)}_{1,1} - \sqrt{3/5}\, b^{(0)}_{2,2}]}$$
$$+ B_2P_2(\cos\theta)\frac{\{b^{(2)}_{1,1} - 3\, b^{(2)}_{1,2} + \sqrt{21}\, b^{(2)}_{2,2}\}}{10[b^{(0)}_{1,1} - \sqrt{3/5}\, b^{(0)}_{2,2}]}$$
$$= 1 + B_1P_1A_1(2) + B_2P_2A_2(2)$$

In the actual experiments the two transitions are mixed and cannot be separated except at energies higher than the $1^- \to 2^+$ transition endpoints. Thus the measured correlation function will be a combination of Eqs. 13a and 13b and will contain the ratio r of the $1^- \to 2^+$ branch intensity to the $1^- \to 0^+$ branch intensity at a given energy. Then we have

Eq. 14
$$W(\theta) = 1 + B_1P_1A_1(r) + B_2P_2A_2(r) = \frac{W(1\to 0,\theta) + r\cdot W(1\to 2,\theta)}{[1 + r]}$$

where $A_k(r) = \dfrac{A_k(0) + r\cdot A_k(2)}{[1 + r]}$.

From Eq. 14 it can be seen that the angular distribution contains two terms which differ in angular dependence (P_k) and in temperature dependence (B_k).

These terms can be separated so that a measurement of $W(\theta)$ at two angles or at several temperatures allows the determination of the two coefficients $A_1(r)$ and $A_2(r)$. Since r is a known function of energy the remaining problem is that of extracting the particle parameters. $A_1(0)$ and $A_2(0)$ are functions of the same three particle parameters and therefore two ratios can be determined by measuring these coefficients. $A_1(2)$ and $A_2(2)$ are functions of eight particle parameters. This is the case because the matrix element $\int B_{ij}$ is allowed in the $1^- \rightarrow 2^+$ transition and thus particle parameters having a subindex 2 enter the expression; these particle parameters are all functions of $\int B_{ij}$. As in Ref. 7, one may assume that the first-rank particle parameters $b_{1,1}^{(k)}$ (k = 0,1,2) are identical for the two decay branches: this is equivalent to assuming that the 2^+ and 0^+ levels in ^{186}Os, ^{188}Os, and ^{194}Pt are similar in character for the purpose of determining nuclear matrix elements.[58] If this assumption is made, the total number of particle parameters is eight for both decay branches. Five of these involve L = 2, i.e. the $\int B_{ij}$ term. Clearly some additional information about the relative size of this matrix element is needed for a complete analysis of the angular distribution data. Fortunately the $1^- \rightarrow 2^+$ transition is followed by a gamma ray in each case. One can determine the gamma ray anisotropy of these transitions concurrently with the beta particle measurements.[59] The gamma ray correlation function is given by Eq. 2, Chap. I, which may be simplified to:

$$\text{Eq. 15} \qquad W(\theta) = 1 + B_2 U_2 F_2 P_2(\cos\theta)$$

where the B_2 and P_2 are the same as in Eq. 14, F_2 is a known function of the decay scheme, and U_2 is a function of spins and multipolarities of

levels and transitions preceeding the observed gamma ray in the decay scheme. In the present case only two multipolarities are possible in the preceeding beta decay: L = 1 and 2. One finds that U_2 has the same magnitude but opposite signs for the two possibilities. Therefore a measurement of $W(\theta)$ for the gamma transition should give an average value of U_2 which in turn gives a measure of the relative amounts of $L = 2$ ($\int B_{ij}$) to L = 1 intensities in the $1^- \rightarrow 2^+$ beta decay. Combining this knowledge with $A_1(r)$ and $A_2(r)$ from the beta angular distribution measurements makes it possible to determine ratios of the particle parameters (or, more precisely, ratios of the nuclear matrix elements $\int \underset{\sim}{r}$, $\int \underset{\sim}{\alpha}$, $\int \underset{\sim}{\sigma} \times \underset{\sim}{r}$, and $\int B_{ij}$.).

Specifically, let us denote by I(1) the part of the $1^- \rightarrow 2^+$ beta decay intensity which is due to L = 1 matrix elements. For this part of the decay, U_2 has a positive sign ($U_2 = 0.5916$). The L= 2 part of the transition is then I(2) and for this part of the decay $U_2 = -0.5916$. In the actual decay both parts may occur: the total intensity for a $1^- \rightarrow 2^+$ transition is given by

$$I = I(1) + I(2) = -S(E) \cdot \{(1/\sqrt{3}) b^{(0)}_{1,1} - (1/\sqrt{5}) b^{(0)}_{2,2}\}$$

where S(E) is the statistical spectrum shape factor.[29] Thus for the average value of U_2 observed in measuring $W(\theta)$ we have

$$\text{Eq. 16} \qquad \bar{U}_2 = \frac{I(1)(0.5916) + I(2)(-0.5916)}{I(1) + I(2)} \quad \text{or} \quad \bar{U}_2/0.5916 = \frac{[1 - R]}{[1 + R]}$$

with $R = I(2)/I(1) = -\sqrt{3/5}\{ b^{(0)}_{2,2}/b^{(0)}_{1,1} \}$

Eq. 16 assumes that the 2^+ state is populated only by the $1^- \rightarrow 2^+$ beta decay. This is a good approximation in the decay of ^{186}Re (99.7% of the 2^+ population is via the beta decay directly to that level) but not in the ^{188}Re

or ^{194}Ir decays, where beta-gamma cascades through higher excited states feed the 2^+ levels significantly. In these cases, allowance must be made for attenuation of the gamma anisotropy by preceeding transitions other than the beta decay of interest. This was done using the decay scheme from Ref. 61 for the ^{188}Re decay, and the simplified decay scheme used by Reid et al (Ref. 59) for the ^{194}Ir decay. The results are included in Table IIIB.

Since the $b^{(k)}_{L,L'}$ are all functions of the same four matrix elements, measurement of the three quantities R, $A_1(r)$, and $A_2(r)$ in principle determines the ratios $\int\underset{\sim}{\alpha}/\int\underset{\sim}{r}$, $\int\underset{\sim}{\sigma}\times\underset{\sim}{r}/\int\underset{\sim}{r}$, and $\int B_{ij}/\int\underset{\sim}{r}$. The analysis for the nuclear matrix element ratios will be mentioned further in Chap. VIII.

The two coefficients A_1 and A_2 must be separated in the analysis of the beta angular distribution. As mentioned previously, they differ both in temperature dependence and in angular dependence of their coefficients in the correlation function. To separate them on the basis of temperature dependence requires not only fitting of temperature dependence curves, but also accurate determination of the sample temperature over a wide range. The difficulties associated with this method are described in the section entitled Thermometry. The angular dependence appears in the Legendre polynomials. In these experiments, two beta detectors were used, in axial and equatorial positions relative to the quantization axis (magnetic field $\vec{H}_o$). The role of the axial counter can be changed from "0°" to "180°" by reversing $\vec{H}_o$. By combining data from positive and negative field directions one can separate the A_1 and A_2 terms. A second method of separation is the combination of data with a given field direction from the axial and the equatorial counters. The two methods can be compared to give a check

on the internal consistency of the data. Explicit formulas for A_1 and A_2 may be derived using Eq. 14. Noting that A_k always occurs in combination with P_k we can define $C_k = A_k(r) \cdot P_k(\cos\theta)$. It is also notable that in deriving Eq. 14, the implicit assumption was made that the intensity at angle θ is normalized by the intensity from unpolarized nuclei ("warm" counting rate) at the same angle. In the actual experiments the normalization counts were recorded at the temperature of the pumped 1° helium bath. At this temperature a finite nuclear polarization remains for the nuclei studied in these experiments, and this must be taken into account in the data analysis. The B_2 term at the bath temperature is about 0.0006 and may be neglected, but the B_1 term is of order 0.04 for the Re nuclei and 0.017 for ^{194}Ir and it should be retained. Eq. 14 suitably modified becomes:

Eq. 17 $$W(\theta) = [1 + B_1C_1 + B_2C_2]/[1 + B_1'C_1].$$

Here B_1' is the orientation parameter at the bath temperature. At a second angle θ' we have $W'(\theta') = [1 + B_1C_1' + B_2C_2']/[1 + B_1'C_1']$

with $C_k' = [P_k(\cos\theta')/P_k(\cos\theta)] \cdot C_k = G_kC_k$. Inserting the latter definition of C_k' and combining the two anisotropy equations and rearranging, we get expressions for C_1 and C_2 in terms of the anisotropies measured at θ and θ':

Eq. 18a $$C_1 = [1 + G_2(W-1) - W']/D$$

Eq. 18b $$C_2 = [(G_1-1) \cdot (WW'B_1'+B_1) + B_1(W'-WG_1)]/B_2D$$

where $D = B_1'(G_1W' - G_2W) + B_1(G_2 - G_1)$. The angles θ and θ' may represent a given counter with + and - field directions, or the axial and

the equatorial counters at a given field direction. In the former case, G_k has the simple form $G_k = (-1)^k$ assuming the counter positions to be unchanged during the field reversal. Thus four types of anisotropies are measured: from the axial counter with + field direction ($\theta = \pi$) one gets $W_+(Ax.)$; from the axial counter with - field ($\theta = 0$), $W_-(Ax.)$; from the equatorial counter with + or - fields ($\theta = \pi/2$), $W_\pm(Eq.)$. These anisotropies can be combined in various combinations in Eqs. 18 to give values of C_1 and C_2. Four such combinations were used and will be distinguished as follows:

Case I, $W = W_+(Ax.)$, $W' = W_-(Ax.)$, $G_1 = -1$, $G_2 = 1$

Case II, $W = W_+(Eq.)$, $W' = W_-(Eq.)$, $G_1 = -1$, $G_2 = 1$

Case III, $W = W_+(Ax.)$, $W' = W_+(Eq.)$, $G_k = P_k^+(E)/P_k^+(A)$

Case IV, $W = W_-(Ax.)$, $W' = W_-(Eq.)$, $G_k = P_k^-(E)/P_k^-(A)$

A sample calculation showing the details of the actual data analysis procedure is given in the next chapter.

Thermometry

The orientation parameters B_k are strong functions of $\beta (= \mu_n H_{hf}/Ik_BT)$ in some region of values of β. For $\beta \to 0$, the B_k are vanishingly small, while for values of β above some limit, the B_k become virtually constant (saturated). The value of β at which saturation occurs depends on I and k. Of course, the B_k's are never really constant at a finite temperature, since complete nuclear orientation is obtained only at absolute zero. However, for I = 1, and values of β above 7, B_1 differs from its zero-temperature value by less than 0.1%, while B_2 is saturated to similar

accuracy when β is greater than 8. To an accuracy of a few percent, B_1 and B_2 are saturated above $\beta = 4$ and 5, respectively.

In the cases of ^{186}Re and ^{188}Re, μ_n is about 1.75nm, and H_{hf} in iron is 760 koe.[9,60]; thus $\beta \simeq 48$ mdeg./T. In the case of ^{194}Ir, μ_n is 0.37 nm and H_{hf} in iron is 1520 koe.,[59] giving $\beta \simeq 20$ mdeg./T.

Most low-temperature nuclear orientation experiments are performed in the region of temperatures in which the B_k are varying rapidly with temperature; therefore it is important to have an accurate measure of the sample temperature throughout the experiment. The usual method of temperature measurement is to monitor the anisotropy of some radiation from the nuclei under study or from other solute nuclei whose hyperfine parameters and decay scheme are well known. This type of thermometry has several limitations: the accuracy is limited by the statistical accuracy of the counting, which is in turn limited by radioactive heating and interference with other radiations of interest; the temperature is known only as accurately as the product $\mu_n H_{hf}$; and since the quantity measured is an ensemble average over a large assembly of nuclei, it is subject to inaccuracies from local variations in temperature or H_{hf} which might give erroneous results for the true sample temperature. For these reasons it would be preferable to perform the experiment entirely in the temperature region where β is above the saturation value so that the observed nuclear orientation is independent of the exact sample temperature.

The warming curve of the sample in the cryostat used in this work was measured prior to the beta decay experiments by using foils of ^{60}Co in Fe prepared in a manner similar to the beta decay foils. These experiments

were done to determine the effects of using thin foils attached only at the edges to the thermal link, and of heating the detectors in proximity to the source foils. It was found that the sources could be cooled to about 5 mdeg.K. and would warm to 10 mdeg. in about 5 hrs. under these conditions. The samples remained below 50 mdeg. for about 12 hrs. at which time the CA guard salts and heat shield had warmed sufficiently to start releasing adsorbed residual exchange gas in quantity. Warmup then proceeded rapidly and in a few minutes the sample was at the temperature of the liquid helium pumped bath. Referring to the values for β given above, one can see that for the first 4 or 5 hours of an experiment the nuclear orientation of the two Re isotopes would be saturated. Thus no thermometry was required and all of the first few hours of counts could be averaged together to produce a measured anisotropy with good statistical accuracy.

The case of ^{194}Ir is somewhat different. Because of the smaller values of β at a given temperature, the ^{194}Ir nuclear orientation was saturated only at the beginning of an experiment, perhaps for about an hour. Again no additional thermometry was required, however, since the data could be analyzed in such a way as not to require knowledge of the foil temperature. Using Eqs. 18, the measured anisotropies from the beginning of each experimental run could be combined to determine the product $A_1(r)\ B_1$. Inserting $B_1(sat.)$ for B_1 then gives A_1. The only assumption made is that B_1 was saturated during the counts analyzed in this way, and this can be assured by using only those counts for which the observed anisotropies were constant within statistical errors. Later

counts can then be analyzed for A_1B_1, and, using the previously determined value of A_1, the ratio $B_1/B_1(\text{sat.})$ can be found for all later counts. This ratio uniquely determines β, from which B_2 can be calculated. Using B_2 one can then analyze for $A_2(r)$, and, using the gamma ray anisotropies, for $\overline{U}_2$. This method clearly is not as accurate as that used for the Re isotopes, since the results depend on the analysis of only the first hour or so of counts; but the method is probably still superior to using a separate gamma ray thermometer.

Some mention should be made of the separation of A_1 and A_2 using temperature dependence. For this method one needs to fit the anisotropy to temperature dependence curves to determine the relative sizes of the coefficients of B_1 and B_2. The different temperature dependences of B_1 and B_2 are most obvious at high temperatures, where B_2 approaches zero much faster than B_1, and in the near-saturation region, where B_1 becomes constant faster than B_2. The high temperature region is least accurate because there the anisotropies are small. Thus to use this method one requires an accurate knowledge of the sample temperature in the range where the anisotropy is changing rapidly with temperature. Clearly this knowledge is limited by the effects mentioned above, besides which the statistical accuracy of the data taken in the temperature dependent region is poor because the sample temperature is not in this region for long and because the temperature is changing fairly rapidly in this region. (To be sure, these points apply only to the characteristics of the apparatus used in these particular experiments and to the particular isotopes studied. In many cases, use of temperature dependence curves is desirable or

necessary. Isotopes for which the nuclear orientation is saturated at temperatures conveniently available are exceptional.) Furthermore, measurements made in the saturation region are insensitive to temperature and H_{hf} inhomogeneities in the sample as long as they are not rather large. Thus no attempt was made to separate A_1 and A_2 using temperature dependence. As pointed out in the previous section, the use of two particle detectors at different angles and of two field directions gives an internal cross-check on the geometrical separation of the anisotropy coefficients.

Decay Corrections

All of the isotopes used in this work have fairly short half-lives and so corrections must be applied to the data for decay of the sources during the experiments. The values of the half-lives used were: ^{186}Re, 90.0 hrs; ^{188}Re, 16.7 hrs; ^{194}Ir, 17.4 hrs.[61] The corrections were made by multiplying the data from each count by a factor $\exp[0.693\ t/t_{1/2}]$ where t is the elapsed time from the beginning of the experiment to the middle of the count in question. This was done by the computer program which interpreted the magnetic tapes containing the experimental data.

In the course of a long experiment the change in counting rate due to decay was greater than that due to the anisotropy being measured, especially in the cases of ^{188}Re and ^{194}Ir and for the gamma ray measurements. For this reason several short experiments were performed, in which counting was continued for only about an hour after demagnetization and the sample was then warmed by admitting exchange gas. In these experiments the decay corrections were small and errors due to variation of efficiency of the counting systems with counting rate were minimized. (Such variations of

counter efficiency with count rate, if present, would manifest themselves in exactly the same way as a systematic error in the decay correction and could be detected by observing the decay of the source for several half-lives and plotting the log of the count rate vs. time to check for linearity. This was done in some cases; see below. Because of the close connection between decay corrections and possible counter efficiency variations, the two topics are discussed together henceforth.) To check for counter efficiency effects, decay curves were constructed using the warm counts from several consecutive experiments. The beta counters were found to give linear plots and values of the half-life in good agreement with the known values, while the gamma counters gave somewhat high values (e.g. 20 hrs. instead of 16.7 hrs. for ^{188}Re). For this reason the gamma anisotropy data from some of the long runs with the shorter-lived isotopes were not used.

Background Corrections

Several potential sources of background radiations exist. The most constant one is the natural background in the laboratory, which is mostly due to ^{40}K. This isotope emits both electrons and positrons, which do not, of course, penetrate the cryostat or the gamma counter shields and are thus not themselves a problem. It also emits a gamma ray at 1.46 Mev. which gives rise to a backscatter peak near 150 kev. (See Chap. V, p. 47). In the analysis of the gamma ray anisotropy data, a trapezoidal background is subtracted from under the photopeaks to correct for this and other background radiations. (See Fig. 20.) The room background is isotropic and usually less than 10% of the photopeak area so the correction is not

a major source of error.

A second source of background radiation is the activation of the iron host foils and their impurities. The principal impurity in the foils used was copper, which gives 12.8 hr. ^{64}Cu on activation. This isotope emits $\beta^{\pm}$ particles at energies below 640 kev., and gamma rays at 1.34 and 0.511 Mev. The electron and positron endpoints are below most of the particle energies for which data were anlayzed in these experiments and thus these activities present no background problem. The 1.34 Mev. gamma ray might give a background under the ^{186}Re beta spectrum due to Compton events in the beta detectors but its intensity is estimated to be at most only 0.01% of the ^{186}Re beta spectrum intensity so no correction was made. The 511 kev. annihilation radiation from this isotope could be seen in the gamma ray spectrum of freshly irradiated sources but had disappeared by the time the samples had been worked up and mounted in the apparatus. As mentioned earlier, the only observable activity from the iron itself was 45 day ^{59}Fe. This isotope is produced by neutron capture from ^{58}Fe, which is only 0.3% abundant in natural iron and has a neutron capture cross section of 1.2 barns (compared to about 100 barns for the Re and Ir solutes). The decay rate ratio of the isotopes studied to ^{59}Fe was at least 500:1 immediately after irradiation (gamma counting showed 700:1 in the case of source #4, for example). In any case, the highest energy radiation of any intensity from ^{59}Fe is the 1.29 Mev. gamma ray and so no background problem occurs with ^{188}Re or ^{194}Ir. Some background from Compton electrons from the ^{59}Fe 1.09 and 1.29 Mev. gamma rays might be present under the ^{186}Re beta spectrum and the maximum size of such a

background is shown in Fig. 18. Sources #3 and #6 differed by a factor of two in ^{185}Re concentration (and hence in relative ^{59}Fe background size) and a comparison of the data from these two sources gives an indication of the importance of the background for the ^{186}Re data. In fact, the values of A_1 and A_2 derived from Run 5 (source #3) do seem to be systematically lower at high energies than those derived from runs with source #6; however, the statistics are poor at the high energy end of the beta spectrum, so the effect may not be significant. An estimate of the probable attenuation of the measured A_1 from source #3 due to this background indicates about 10% in the highest-energy interval, 5% in the next interval, and decreasing amounts in lower intervals. The attenuation would be approximately half as great in source #6, which was weighted more heavily in determining the final average values of the A's.

A third source of background radiation is the additional activity resulting from the lack of 100% enrichment of the separated isotopes used in source preparation. In the case of the ^{188}Re and ^{194}Ir sources, the impurity activities were ^{186}Re and ^{192}Ir, respectively. The former offers no interference with ^{188}Re since all of its radiations are below the lowest energies used in the data analysis for that isotope. The highest energy of intense radiations from ^{192}Ir is 1.06 Mev.; all gamma and beta transitions above this energy are less than 0.1% of the total decay strength. Thus there is no background problem for the ^{194}Ir measurements from this source. In the case of the ^{186}Re sources, a few percent of ^{188}Re was produced because of incomplete enrichment of the ^{185}Re used. None of the sources was actually used until at least 36 hrs. after irradiation, so

that the ^{188}Re strength was down to less than 1% of the ^{186}Re strength. Also, the ^{188}Re beta angular distribution is similar in shape and sign to that of ^{186}Re and the energy dependence of the anisotropies is not too great, so the size of the background correction to the ^{186}Re angular distribution is small.

Finally, there are interfering radiations within the decay scheme of a given source isotope. In the case of ^{186}Re this is no problem, since the only radiations other than the beta transitions of interest are the 137 kev. gamma ray, a weak (1.5% of total decay) gamma ray at 123 kev. from the electron capture decay to ^{186}W, and weak gamma and beta transitions (0.1%) associated with the 767 kev. level in ^{186}Os. The 123 kev. gamma ray is unresolved from the 137 kev. line, but it has only 1/14 of the intensity and about the same anisotropy as the latter line, and therefore does not give rise to a large error. (If the electron capture decay were pure L = 1, the anisotropy of the two lines together would be about two percent greater than for the 137 kev. line alone, assuming the mixing ratio found for the beta decay to the 137 kev level. In fact, because of the method of analysis, the 123 kev. line was probably mostly excluded from the data.)

In the case of ^{188}Re, there are numerous beta branches below 1.5 Mev. and gamma rays from 0.297 to 2.03 Mev. but the beta branches total only 2% of the decay and the gamma rays above 1 Mev. total about 0.6% so again, no serious background problem arises.

The ^{194}Ir decay has beta branches from 1.6 Mev. down which total 6% of the decay (1.2% at 1.62 Mev., the rest below 1.3 Mev.) which cause

no interference. The gamma spectrum is complex: most of the gamma ray intensity is below 1.49 Mev. (0.4% above this level) and causes no significant background correction to the angular distribution data from the 2.24 and 1.91 Mev. beta branches. However, the complex of gamma rays near 300 kev. (293 kev.,1%; 301 kev., 0.15%; 328 kev., 5%) is unresolved by the NaI gamma counters used to measure the 328 kev. gamma ray anisotropy, and thus the anisotropy data must be corrected for the other two lines. Assuming the 301 kev. line to be E2 + 17%M1[62] and taking the 293 kev. line to be E2 + 1%M1,[62] and correcting for differences in absorption in the cryostat walls and in detection efficiencies, one finds the anisotropy of the 328 kev. line to be attenuated by a factor of 0.83±.13. The errors allow for the uncertainties in the 293 and 301 kev. mixing ratios and intensities. The Li-Ge detectors used by Reid et al[59] were able to resolve the three lines in the 300 kev. group and thus their value for the 328 kev. anisotropy lacks the large uncertainties caused by the background correction in the present case.

Magnetic Deflection of the Beta Particles

The effect of the polarizing field H_o should be considered. Electrons moving in a plane perpendicular to a magnetic field move in circular orbits whose radius is given by:[63]

Eq. 19 $$\rho = 1.708\frac{\sqrt{E^2 + 2E}}{H}$$

where ρ is in cm., E is the electron's kinetic energy in mc^2 units, and H is in koe. The curvature of the electron paths has two effects in the present experiments: first, due to the use of collimators and to

the geometry of the detectors, and the effect of H_o on the effective solid angle, the intensities of the electron spectra depend on the applied field. In particular, the intensity in the axial counter is reduced slightly for both signs of the field, while in the equatorial counter it is increased somewhat for positive fields and reduced for negative fields because the source is slightly off-center with respect to the counter. (See Fig. 10.) This effect is unimportant for the measurement of anisotropies, however, which involves taking only ratios of cold/warm counting rates at constant H_o.

The second effect of the magnetic field is to bend the electrons emitted in the direction of a counter away, and to bend others into the counter. This angular effect is potentially serious since it creates an error in the measured detector angles. It will be considered in more detail for each detector.

The electrons emitted towards the equatorial counter are primarily in a plane perpendicular to H_o. Simple geometrical considerations show that while the electrons move through a distance Z they are deflected by the field through an angle α whose cosine is given by

$$\cos(\alpha) = [1/2 + (\underline{1 - Z^2/\rho^2})^{\frac{1}{2}}]^{\frac{1}{2}}.$$
$$2$$

For small deflections, i.e. $\rho >> Z$, this formula is given to a good approximation by

Eq. 20 $$\cos(\alpha) = 1 - Z^2/8\rho^2.$$

In the case of the equatorial counter, the deflection is in the plane perpendicular to the quantization axis and is thus a variation in the angle ϕ ; but the angular distribution is invariant with respect to rotations

about ϕ (axial symmetry) and therefore the magnetic deflection produces no error in the measured anisotropy in the equatorial counter.

In the axial counter the situation is more complex. If the counter were exactly at zero degrees there would be no deflection since the electrons emitted to the counter would have no component of velocity perpendicular to the magnetic field. In practice the counter is offset from zero degrees to avoid scattering in the source foil and in any case it subtends a finite solid angle so there is some deflection of the electrons emitted in its direction. The distance Z traveled by the electrons is proportional to the component of velocity parallel to the magnetic field while the deflection is proportional to the perpendicular component of velocity. The resulting deflection is given by a formula similar to Eq. 20 (in the approximation $\rho^2 >> Z^2\sin^4(\theta_o)$):

Eq. 21 $$\cos(\alpha) = 1 - Z^2 \sin^4(\theta_o)/8\rho^2$$

where θ_o is the apparent emission angle for the electrons. (The geometry is shown in Fig. 17.) As expected, this formula reduces to Eq. 20 for $\theta_o = \pi/2$, and gives $\alpha = 0$ for $\theta_o = 0$. Substituting Eq. 19 for ρ into Eq. 21 gives

Eq. 22 $$\cos(\alpha) = 1 - H^2Z^2\sin^4(\theta_o)/23.4(E^2 + 2E).$$

In the present experiments, the maximum deflection occurs in the case of the low energy electrons from ^{186}Re. The minimum energy used in the analysis of the anisotropy was about 500 kev. ($E \tilde{=} 1$). The maximum value of H_o used in this case was 1.6 koe., and the maximum value of Z (source-detector distance) was 1.5 cm. The maximum value of θ_o was about 30° (at the bottom of the axial counter collimator). Inserting these values in

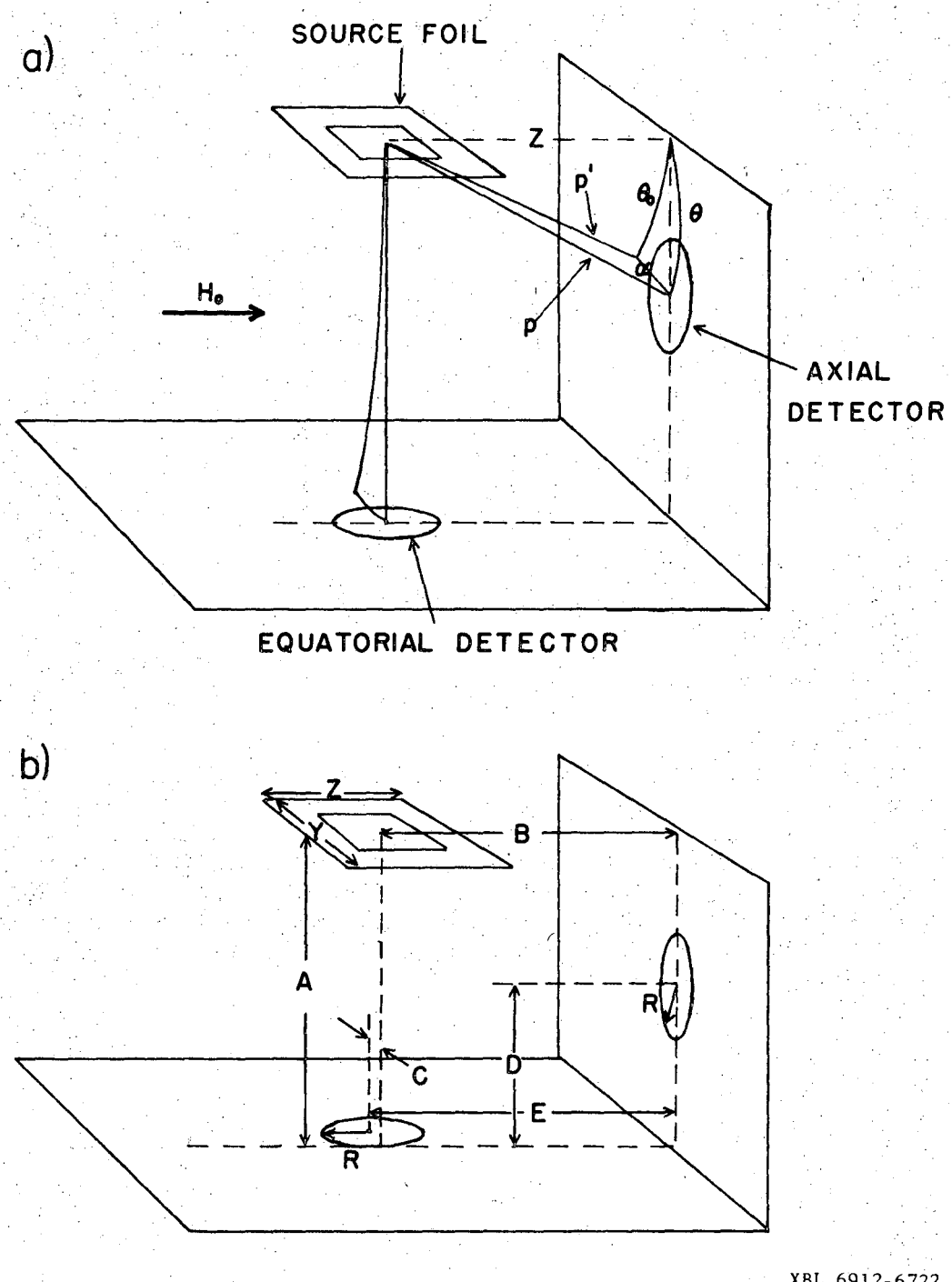

XBL 6912-6722

Fig. 17. Sketches of source and beta detector geometry. 17a): Geometry used in magnetic deflection calculation. Line p is an electron's path in zero field; p' is its path with the field on as shown, with deflection through angle α. Angle θ is the true emission angle, and θ_o is the apparent emission angle with H_o on. Angles α, θ, and θ_o form a right spherical triangle for which $\cos\theta = \cos\alpha \cdot \cos\theta_o$. 17b): Geometrical quantities used in the solid angle and scattering calculations.

Eq. 22 gives $\cos(\alpha) = 0.996$. From Fig. 17 using the law of cosines for a spherical triangle, one gets $\cos(\theta) = \cos(\alpha) \cdot \cos(\theta_o)$ where θ is the true emission angle, θ_o is the apparent emission angle, and α is the deflection angle. Thus the maximum error in the observed angle of emission is about 0.4%. The average errors are at least twice this small, even for ^{186}Re. This is considerably less than the estimated errors in measurement of the geometry of the counters; hence errors due to the field H_o will not be considered in the treatment of data from either the axial or the equatorial beta counter.

Solid Angle Corrections

Because the radiation detectors subtend finite solid angles rather than being geometrical points, a correction must be applied to the angular distribution for the range of angles θ seen by each detector. If the center of the detector is at an angle θ_o to the quantization axis, then the detector will see an average value of the kth Legendre polynomial:

$$\overline{P}_k = P_k(\cos\theta_o) \frac{\int\int_{\theta_1}^{\theta_2} P_k(\cos\theta)\, d\theta \sin\theta\, d\phi}{\int\int_{\theta_1}^{\theta_2} \sin\theta\, d\theta\, d\phi}$$

where θ_1 and θ_2 are the limits of θ subtended by the detector, referred to the center of the detector. If the source is not a point, further averaging over the source area must be carried out. In the case of cylindrical NaI counters, the solid angle correction coefficients Q_k defined so that $\overline{P}_k = Q_k P_k(\cos\theta_o)$ are tabulated.[13] In the case of the beta particle detectors the tabulated coefficients are not sufficient since the

source is of large size compared to the counter area and source-counter distance, and since it is off-axis with respect to the "axial" counter. A computer program was used to calculate values of $\overline{P}_k$ for k = 1 and 2 and for the geometry measured in each experimental setup. The program used numerical integration to calculate $\overline{P}_k$ from each point on a grid of 100 points on the source area (the source was assumed to be planar), and then averaged over the entire source with proper weighting for the activity of each point as determined from autoradiographs. (See Source Preparation, page 71, and Fig. 16.) An allowance was also made for scattering of the beta particles as described in the next section. The second half of Table II gives the calculated values of $\overline{P}_1$ and $\overline{P}_2$ for each detector and each experimental setup. Note that the calculation of $\overline{P}_k$ assumes that the beta detector efficiency is independent of entrance angle of the particles. The geometry of the source and counters is shown in Figs. 10 and 17.

Scattering

In any measurement involving beta-particle spectroscopy, scattering is a potential source of error. In a low temperature nuclear orientation experiment it is particularly difficult to use a "mass free" source and source mounting or to have a large experimental chamber made of light materials to minimize scattering. Thus some consideration needs to be given to possible errors introduced by scattering of the electrons before they are detected. Three types of scattering may be distinguished and will be considered separately.

First, there is energy loss due to penetration of the source foil and

the detector windows. The sources were all 2.5 mg/cm^2 or thinner, and the windows were 1 mg/cm^2. The maximum projected thickness traversed by the electrons was 10 and 1.1 mg/cm^2, respectively. These thicknesses correspond to energy losses of 13 kev. and 2.1 kev.[64] Most of the electrons (especially those detected by the equatorial counter) traverse much smaller foil thicknesses and the average energy loss in the foil is about 4 kev. for the equatorial counter and 7 kev. for the axial counter. An average adjustment of 7.5 kev. was made in the quoted energies to compensate for this error.

It should be noted that the difference in energy loss by electrons detected by the two counters is a potential source of systematic errors: when data from the two counters (and nominally the same energy) are combined, the difference in actual energies produces a shift in the resulting values of A_1 and A_2. No correction was made for this effect for two reasons: 1) the maximum energy difference is about 5 kev. which is the same order of magnitude as the energy discrimination in the spectra (5 kev./channel); and 2) the maximum slope of a plot of anisotropy W vs. energy (Fig. 21, Chap. VIII) is about .0005/kev., leading to a maximum error in W due to the energy shift of about 0.0025 or about 0.3%. (This will be a decrease in the axial anisotropy with respect to the equatorial anisotropy.) Referring to Table IV in Chapter VIII, one can see that such an error in W will give a maximum error in the calculated A_1 of about 0.3% and that the error in A_2 will tend to cancel among the four calculation cases. The errors are for the most part smaller, especially at low energies where the statistical errors are also smaller. Thus it was felt that in view of the large

uncertainties from other sources (e.g. the measurement of the experimental geometry) and of the somewhat larger statistical errors, no correction was justified.

The second type of scattering is angular scattering by the source foil and the detector windows. A beam of electrons passing through a foil is broadened into an angular distribution whose width depends on the electron energy and the nature of the scattering foil. Angular scattering in the detector windows is not a serious effect for two reasons: 1) The windows are thin and made of light material so the scattering angles are small; and 2) the windows are behind the collimators, so that any electrons which reach them are already selected for detection. Since the windows are also rather close to the detectors, small angle scattering will not prevent transmitted electrons from being detected and this effect thus produces no experimental errors.

Angular scattering in the source foil is more serious. Electrons initially emitted towards the detector may be scattered away from it, while those emitted outside the solid angle of a detector (especially near the plane of the source foil where the projected foil thickness[and thus the scattering angles] is large) may be scattered into the detector and be detected spuriously. Thus the effect of angular scattering is to smear out the observed angular distribution by mixing in electrons emitted at the wrong angles; this effect is similar to the smearing of the distribution by the finite solid angles of the counters. Consequently, a calculation of the angular scattering effect was combined with the solid angle calculation. Williams[65] has given expressions for the angular scattering of

electrons by thin foils normal to the direction of the electron beam, and his theory has been experimentally verified.[66] According to this treatment, the scattered electron beam is described by a gaussian function with "wings" added at large scattering angles. The width of the gaussian is related to $[\ln M]^{\frac{1}{2}}$ where M is proportional to the thickness of material traversed. For electrons emitted to the equatorial counter this expression should be directly applicable. In the case of the axial counter, the electrons are not emitted normal to the plane of the foil and thus pass through an asymmetric arrangement of scattering material; therefore one would expect the resulting angular distribution to be asymmetric. Accordingly, provision was made in the calculation to skew the gaussian as the angle of emission approached the plane of the foil. The widths of the distributions and the scattered intensities on each side of the emission direction could be independently skewed.

The quadrant containing the detector (angles θ) was divided into 90 subintervals of one degree each, and the distribution of electrons produced by scattering at each angle was calculated according to Williams' formula with skewing. The fraction of the electron intensity scattered into the detector (or the fraction scattered out if the subinterval in question was within the solid angle of the detector) was then determined and used as a weighting factor for the Legendre polynomials P_1 and P_2 calculated at the center of the subinterval. The weighted P_k's were then averaged over the entire quadrant to give an average P_k seen by the detector allowing for scattering and geometry effects. (The P_k's were also averaged over the area of the source foil and the detector solid angle as

described in the previous section.) The resulting values are summarized in Table II for several sets of assumptions concerning the scattered distribution.

Explanation of Table II

The first part of Table II shows the calculated average geometry coefficients $\overline{P}_k$ for an idealized geometry but including angular scattering in the source foil. (A) means axial detector and (E) means equatorial; the signs shown correspond to the - field direction. The geometry (Fig. 17) used was: A,B, and C as shown in mm; D = 11.5 mm; E = 11.2 mm; and Z = Y = 3.0 mm. The last column gives the electron energy in Mev. The Roman numerals in col. 2 denote various assumptions about scattering, as follows: I = no scattering. II = Williams' theory with no skewing. III = Williams' theory with the width of the scattered distribution broadened 10% on the side away from the foil and narrowed correspondingly on the foil side. IV = same as III but the scattered intensity as well as the width was skewed. V = same as IV but the skewing was increased to 50% (i.e. the width at angle-θ-emission corresponded to the calculated width at 0.5 θ on the side of the scattered beam away from the foil and to the width at 1.5 θ on the foil side of the scattered beam.) These calculations of the effect of scattering on $\overline{P}_k$, along with estimates of attenuation due to backscattering, were used to estimate the scattering corrections in Fig. 19.

The second part of the table shows calculated $\overline{P}_k$'s for the actual measured geometries, without scattering. Column 1 contains the source numbers, which correspond to those in Table I. In these cases, D = 10.0,

E = 11.0, Z = 6.0, Y = 10.0, and R = 2.0. The last three lines show the effects of errors in the measurement of A, B, and C on the calculated $\overline{P}_k$'s. The sources were assumed to contain a central active spot 3x3mm square with 3.5 times the activity of the surrounding foil. The maximum estimated errors are ±3% in $\overline{P}_1(A)$, ±10% in $\overline{P}_2(A)$, ±.06 in $\overline{P}_1(E)$, and ±2.2% in $\overline{P}_2(E)$. These assume 0.5 mm errors in measurement of all geometrical quantities and that all errors were cumulative, which is unlikely; thus they are probably overestimated. (See Error Analysis, Chap. VIII.) The $\overline{P}_k$'s from this section of the table were modified by the scattering corrections shown in Fig. 19 and used to derive $A_1(r)$ and $A_2(r)$ from the anisotropy measurements.

Table II: Solid Angle and Scattering Calculations

Source	Case	A	B	C	$\overline{P}_1(A)$	$\overline{P}_2(A)$	$\overline{P}_1(E)$	$\overline{P}_2(E)$	W
--	I	15.2	11.2	2.0	.9446	.8394	0.0	-.4899	--
	II	"	"	"	.9447	.8412	0.0	-.4838	0.5
	III	"	"	"	.9455	.8436	0.0	-.4838	"
	IV	"	"	"	.9474	.8488	-.0002	-.4834	"
	V	"	"	"	.9565	.8745	-.0022	-.4810	"
	V	"	"	"	.9560	.8724	-.0009	-.4863	1.0
	V	"	"	"	.9540	.8666	-.0005	-.4878	1.5
	V	"	"	"	.9523	.8616	-.0004	-.4886	2.0
#1	--	15.2	11.2	2.0	.9361	.8171	.0271	-.4666	--
#2		15.0	11.5	1.5	.9435	.8376	.0464	-.4638	
#3		15.3	10.0	2.0	.8686	.6370	-.0626	-.4682	
#4		15.5	11.5	2.0	.8924	.6976	.0312	-.4789	
#5		15.2	11.5	2.0	.9030	.7257	.0319	-.4815	
#6		14.7	9.5	2.0	.8897	.6920	-.0976	-.4666	
#7		14.5	11.0	2.0	.9163	.7623	0.0	-.4798	
#8		15.0	10.5	2.2	.8888	.6885	-.0321	-.4795	
Errors		±0.3	--	--	∓0.8%	∓2.5%	0.0	∓0.1%	
		--	±0.5	--	±.45%	±1.4%	∓.032	±0.5%	
		--	--	±0.5	∓.34%	∓1.1%	0.0	∓.04%	

The third type of scattering which must be considered is backscattering of the electrons from the experimental chamber walls and the detectors. Electron backscattering has been studied in detail by Bothe[67] and by Frank[68]. The relevant portions of their results may be summarized as follows:

1) The backscattering coefficient p (= the fraction of incident electrons backscattered at all angles and energies) increases with increasing scatterer Z and decreases with increasing electron primary energy. For Z = 30 (Zn) and 500 kev. it has a value near 0.30.

2) The backscattering cross section is greatest at the angle of specular reflection. For grazing angles of incidence, the angular distribution of the scattered electrons is sharply peaked, while for 180° backscatter it is broad.

3) The energy distribution of the scattered electrons is peaked at some fraction of the primary energy. The fractional energy loss at the peak is greatest for low Z materials, being about 50% for 1.75 Mev. electrons backscattered from copper. The energy distribution is more sharply peaked for small scattering angles where the energy loss on the average is smaller.

An exact calculation of the distribution of backscattered electrons inside the experimental chamber would be a formidable task, since the scattering cross section is a function of incident angle, scattering angle, primary energy, scattered energy, and scatterer Z and thickness, and since the geometry of the problem is very complicated. However, some

qualitative considerations may give an idea of the effects of backscattering on the observed angular distributions.

First one needs to consider backscattering from the detectors. Since the detectors themselves are saturation backscatterers, about 20 to 30% of the incident electrons will be scattered out without depositing their full energy in the detector. This produces a slight energy dependence in the detectors' apparent efficiency (which is unimportant for anisotropy measurements in which all counts are normalized by the warm counting rate) and gives rise to a sharply increased spectrum intensity at low energies where pulses from the backscattered electrons appear. This effect can be seen in the spectra of Fig. 18. It obviously precludes accurate spectrum shape measurements but this is not a problem for the present work. In general, the data were not analyzed much below the point at which departures from the expected spectrum shape began to appear, thus avoiding errors from backscatter counts due to higher-energy electrons.

Besides scattering by the detectors, there is backscatter from the experimental chamber walls and interior parts. Consider a source emitting at a rate N. The rate of detection of direct electrons is then $N\varepsilon\Omega$ where ε is the detector efficiency and Ω is its solid angle as seen from the source. Some fraction F of the electrons emitted by the source will strike potential backscattering surfaces (the rest will strike surfaces from which backscatter into the detector is unfavorable or impossible due to geometry). Of these electrons a fraction p will actually be backscattered at all angles and energies. They will be detected at a rate proportional to $\varepsilon\Omega'$ where Ω' is the solid angle of the detector as seen from the point of backscat-

Fig. 18. Measured beta spectra for the three isotopes used in this work. The small crosses are the experimental points; the large circles are calculated from the reported spectrum shapes and intensities (Refs. 42-44, 51). The allowed shape is assumed for ^{194}Ir. Only the ground state and first excited state transitions are included. The dashed curves are fit to the calculated points and represent the true spectrum shapes. The deviations at low energies are due to backscattering. The small arrows show the spectrum endpoints for the $1^- \rightarrow 0^+$ transitions as determined from the ^{207}Bi energy calibration. The small trapezoidal area labeled ^{59}Fe under the ^{186}Re spectrum shows the maximum size of the Compton background from ^{59}Fe activity in the sources. The vertical scales are linear and arbitrary.

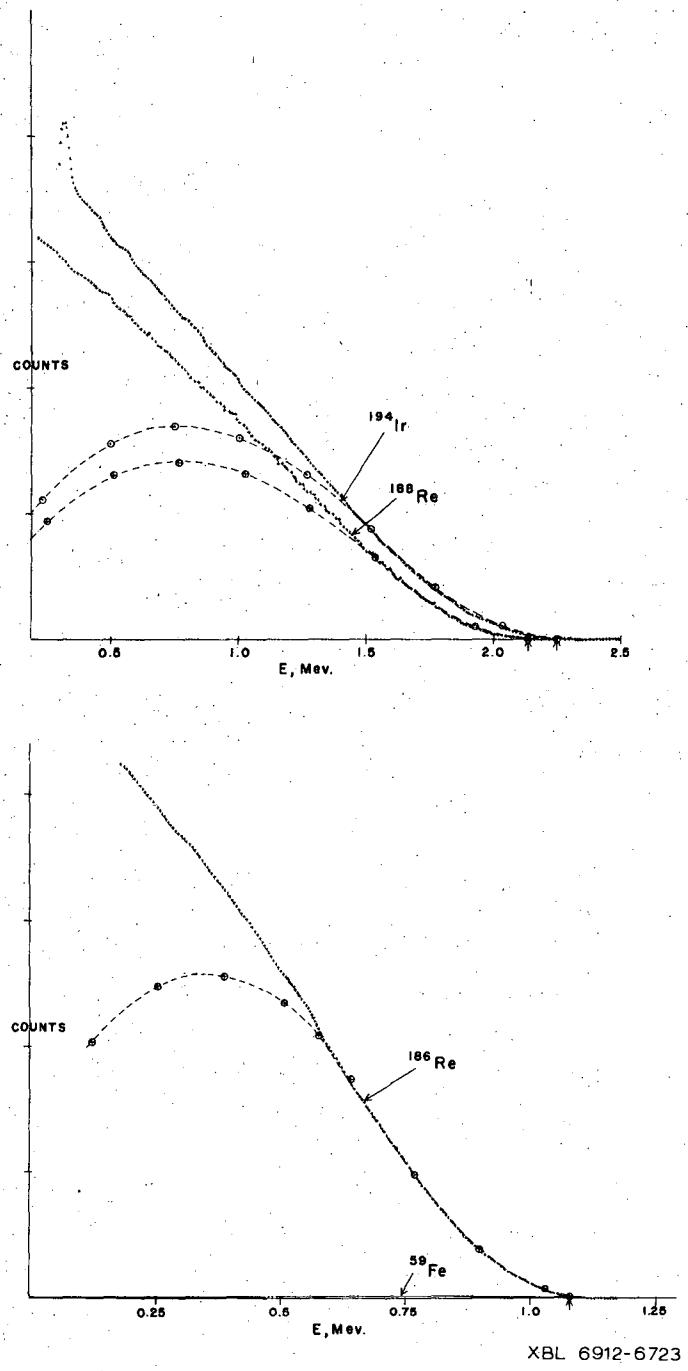
COUNTS
194Ir
188Re
0.5
1.0
1.5
2.0
2.5
E, Mev.
COUNTS
186Re
59Fe
0.25
0.5
0.75
1.0
1.25
E, Mev.
XBL 6912-6723

Fig. 18.

tering. Finally, the backscattered electrons which are detected will have been shifted downward in energy from their initial energy E to an energy E'. They will appear as background under the direct beta spectrum at energy E'; but in the upper half of the beta spectrum, the intensity at E' is greater than at any higher energy E so the backscattered electrons will be further reduced in relative intensity. It can be reasonably assumed that $E' \leq 0.9\ E$ and the intensity ratio $I(E)/I(E')$ is then ≤ 0.1 at the high energy end of the spectrum and ≤ 0.9 near the spectrum midpoint. Combining all these factors gives for the detection rate of the backscattered electrons: $N\,\Omega'\varepsilon F\,p$; and for the relative intensity of backscattered electrons to that of the directly detected electrons: $F\,p\,\frac{\Omega'}{\Omega}\,\frac{I(E)}{I(E')}$. This quantity may be estimated for the two detectors used in the present experiments.

The principal backscattering surfaces for the axial counter are the opposite experimental chamber wall and the top of the equatorial counter collimator. Referring to Fig. 10 one can estimate F for the wall to be about 0.25; p at high energies is about 0.2 and is about 0.3 at low energies. The solid angle ratio Ω'/Ω is about 0.15. For the overall intensity ratio I' we thus get a minimum of 0.002 at high energies and a maximum of 0.025 near the spectrum midpoint. The scattered electrons are emitted at angles near 180° from those of the direct electrons; this means that the P_2 part of their angular distribution will be about the same as that of the direct electrons, while the P_1 part will be opposite in sign. Then for the observed geometry coefficients with scattering we have

$$P_1' = P_1(1 - I')/(1 + I') \quad \text{and} \quad P_2' \cong P_2$$

where I' is the intensity ratio of backscattered to direct electrons estimated above. Thus from scattering into the axial counter by the

opposite wall we get an attenuation of P_1 of from 0.4% near the endpoint of the spectrum to 5% at the midpoint; and to first order no attenuation of P_2. Similar estimates may be made for other sources of scattering and the combined results for the two counters are:

$$P_1'(A) = 0.99\ P_1 \dashrightarrow 0.90\ P_1 \qquad P_2'(A) = 0.99\ P_2 \dashrightarrow 0.92\ P_2$$

$$P_1'(E) = \pm\ 0.002 \dashrightarrow 0.027 \qquad P_2'(E) = 0.99\ P_2 \dashrightarrow 0.89\ P_2$$

In each case the unprimed P_k is the value of the geometry coefficient for the given detector without scattering, and the P_k' are the corresponding values taking backscatter into account. The range of values corresponds to a minimum attenuation near the endpoint ranging to rather large attenuations at the spectrum midpoint. The absolute values of $P_1'(E)$ are given because $P_1(E)$ is nominally zero in the absence of scattering and for a correctly placed equatorial counter. The above estimates are probably pessimistic: the energies of the backscattered electrons are on the average much more than 10% below the primary energies, making the ratio $I(E)/I(E')$ smaller than was estimated above; and also, the idealized geometry assumed in the above estimate maximizes the apparent attenuation. Nevertheless, it is clear that backscattering will produce attenuations of ~ 1% in the upper third of the spectra and will make reductions of ~ 5--10% in the observed anisotropies near the midpoints of the spectra. It should be noted that backscatter, unlike angular scattering in the source foil, will tend to attenuate the observed anisotropy in all cases rather than increasing it at some angles. Fig. 19 shows corrections which were applied to the calculated $\overline{P}_k$'s from Table II to allow for both angular scattering and backscattering.

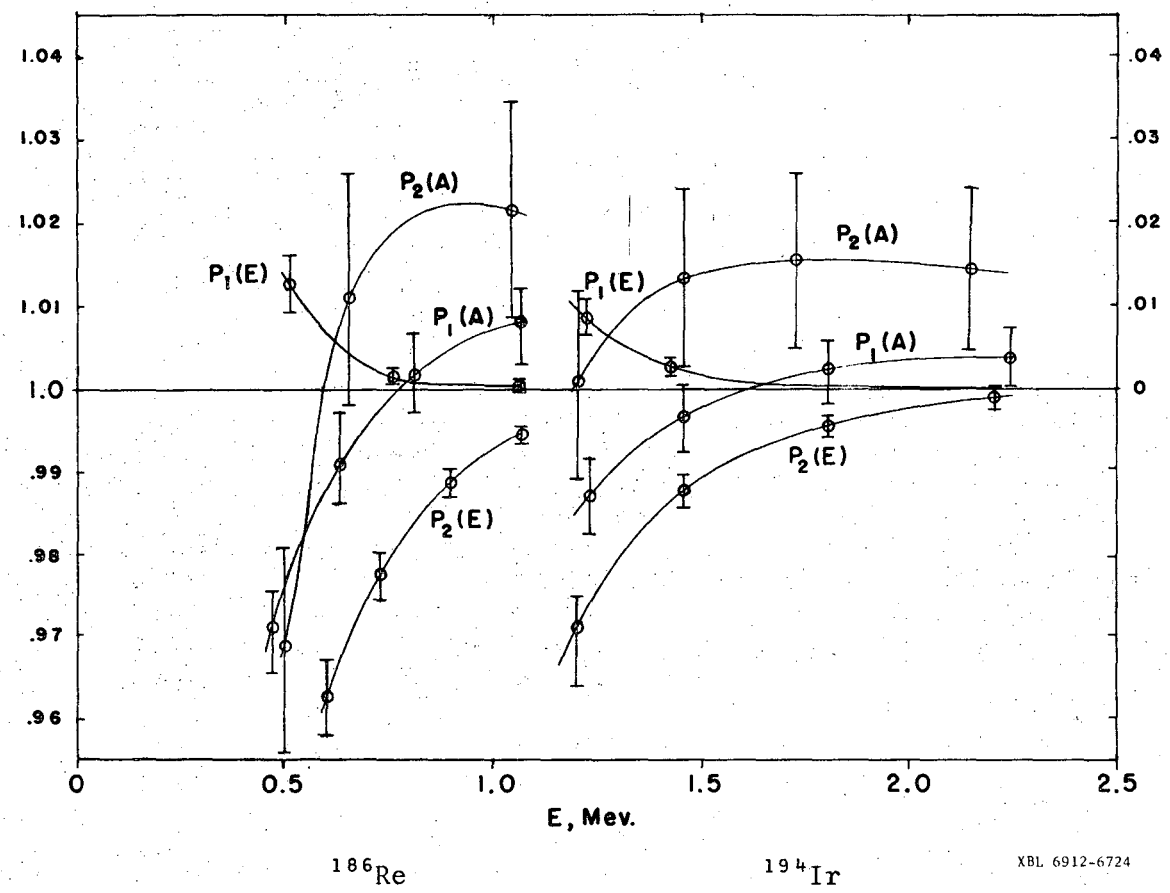

Fig. 19. Scattering correction factors for the calculated geometry coefficients for ^{186}Re and ^{194}Ir. (A) and (E) refer to axial and equatorial detectors. The values for $P_1(E)$ are absolute and are given by the right-hand scale (for - field direction). These corrections include angular scattering in the source foil (Case V; errors include Case IV. See Table II.) and estimated backscatter corrections. The correction factors for ^{188}Re are similar to those for ^{194}Ir but shifted down in energy by 80-125 kev. Backscatter predominates at low energies and angular scattering is dominant at high energies.

CHAPTER VIII

Discussion of Results and Conclusions

Experimental Data

Appendix I contains a list of all runs performed in the first forbidden beta decay experiments, as well as tabulations of the average anisotropies from each run and of the values of $A_1(r)$ and $A_2(r)$ calculated from various combinations of the anisotropies. In order to clarify the process by which the anisotropies and the A_k's were obtained, a sample calculation and description of the data analysis will be given.

Sample calculation: Runs 13 and 14 (^{186}Re, alloy #6, $H_o = \mp 1$ koe.) were chosen as a typical example. The data were recorded during the runs as 1600 channel spectra, with the axial and equatorial gamma spectra in the first two quadrants and the axial and equatorial beta spectra in the last two quadrants. A typical long run produced a tape containing about 66 spectra in all, the last 6 being warm counts. The first step in data analysis was to examine the tapes using a PDP-7 computer which could display selected spectra on a cathode ray screen. The total number of spectra was checked and any effects such as errors in recording or counter gain shifts of large magnitude were detected. The tapes were then sent to the CDC 6600 computer for detailed analysis. Each spectrum was read into the computer memory and smoothed two times by averaging adjacent points, to reduce statistical fluctuations. (This was done for the benefit of the gamma peak locating routine.) The location of the gamma peak in each of the first two quadrants was then determined and the peaks were integrated according to the method shown in Fig. 20. The integration was performed over three different widths to check for systematic errors from scattering.

After initial analysis of the gamma ray data using the three integration widths (Method I), some concern over the failure of the axial and equatorial anisotropies to give the same value for $\overline{U}_2$ arose. (See Eq. 23, Error Analysis section.) The possibility of attenuation due to scattering of the gamma rays(Haag effect) was considered to be serious, so the gamma ray data were re-analyzed, using a different set of peak integration limits (Method II). In Method II, each photopeak was divided into ten intervals, and the anisotropies were calculated for each interval. Then any energy dependence of the anisotropy due to scattering could be clearly seen in the data. The results of the Method I analysis are tabulated in Appendix IB, while the results from the Method II analysis are given in Appendix ID. It may be seen that the narrowest width used in Method I (denoted A3 in Fig. 20.) gives values for the anisotropies which agree well with the values found in the intervals near the peak maximum using Method II. Thus it is clear that although scattering is present and does produce some attenuation in the anisotropy calculated for the whole photopeak, it is avoided by using a narrow integration width (A3) which excludes the low energy scattered tail of the peak.

After the peak integration had been completed, the areas obtained were multiplied by the appropriate decay correction factor. (See Decay Corrections, Chap. VII.) Next the channel corresponding to the spectrum endpoint in each of the beta spectra was located using gain calibration data which were input parameters. Each beta spectrum was divided into twenty intervals from the endpoint down and the counts in each of the ten highest-energy intervals were summed and multiplied by the decay correction factor.

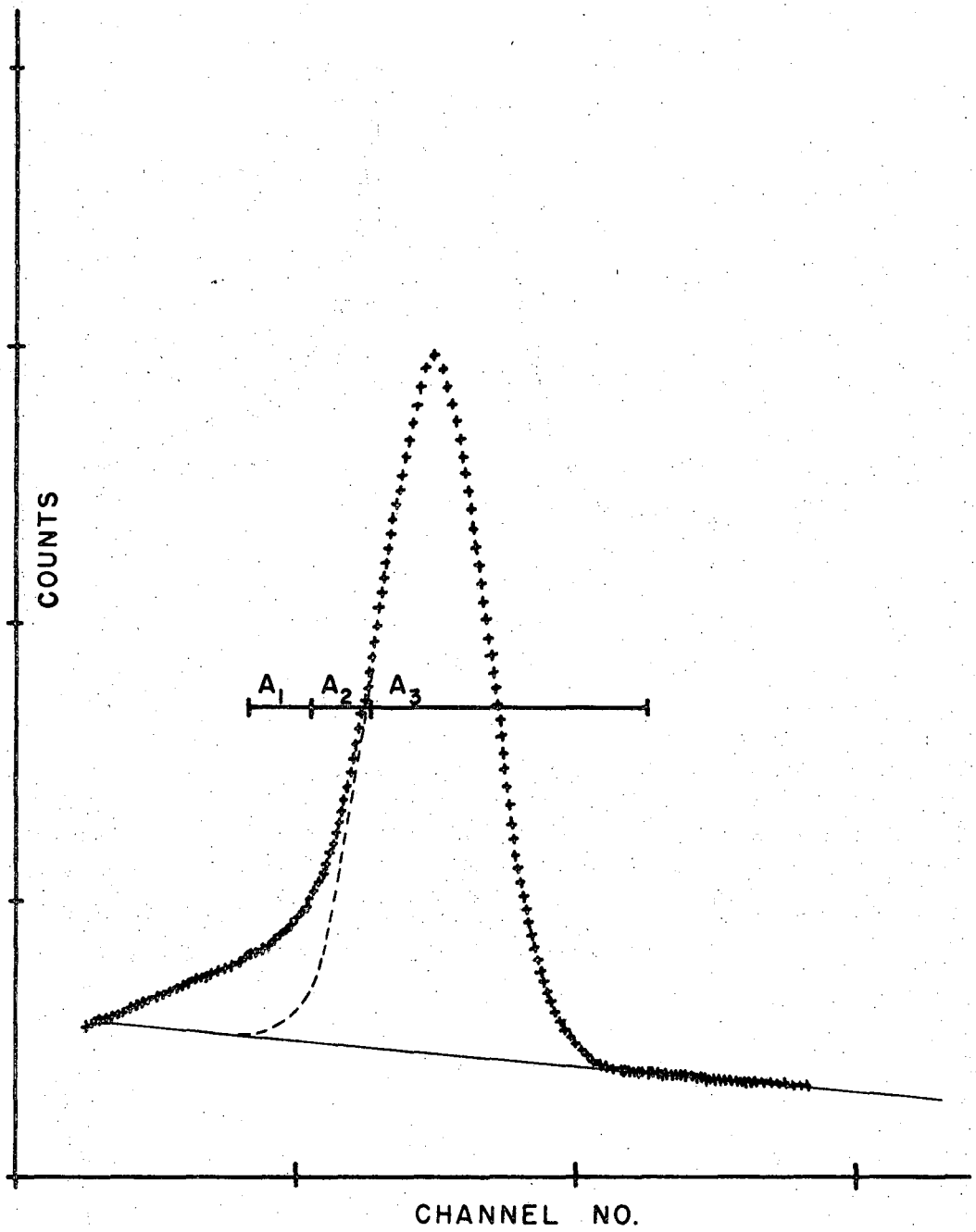

XBL 6912-6725

Fig. 20. Gamma-ray spectrum from ^{188}Re (155 kev. transition). The lower energy scale is about 40 kev./large division. The zero of energy is off scale. The straight line below the peak is the background which was subtracted in the analysis. Low energy tailing is due to scattering in the apparatus walls. The horizontal lines labeled A1, A2, and A3 show three different sets of limits of peak integration used in the data analysis to avoid errors from the scattering (Method I).

The twenty beta spectrum areas (from axial and equatorial counters) and the six gamma areas (or twenty areas in the case of Method II) were stored and the next spectrum on the tape was analyzed in a similar manner. When all spectra on the tape had been so treated, the areas from counts designated as "warm" were averaged together. Then each "cold" area was divided by the corresponding averaged "warm" area to give the anisotropy.

In the example of Run 13, the first five axial gamma areas (corrected for decay, Method I, width A1) had the values 309028, 306166, 304691, 305861, and 305447. The corresponding average warm area was 378009. The calculated anisotropies were .8175, .8099, .8060, .8091, and .8080. The program also calculated an accumulative average of each anisotropy which in the above example at the end of count five had the value .8101. Fig. 21 is a plot of the beta anisotropies at 724 kev. calculated at five-count intervals for the axial and equatorial beta counters throughout Runs 13 and 14. It is clear from Fig. 21 that the anisotropies are essentially constant for the first five hours of counting, because of the saturation of the nuclear orientation, in spite of the fact that the apparatus is continuously warming up after demagnetization. The average anisotropies of all counts up to the dotted line in Fig. 21 were accordingly used for subsequent calculations. It is these averages which are tabulated in Appendices IB and ID for all runs. Fig. 22 shows the average beta anisotropies from all runs plotted against particle energy for the three isotopes studied.

The second stage in the data analysis was the calculation of $A_1(r)$ and $A_2(r)$ from the beta anisotropy data. For this purpose the average anisot-

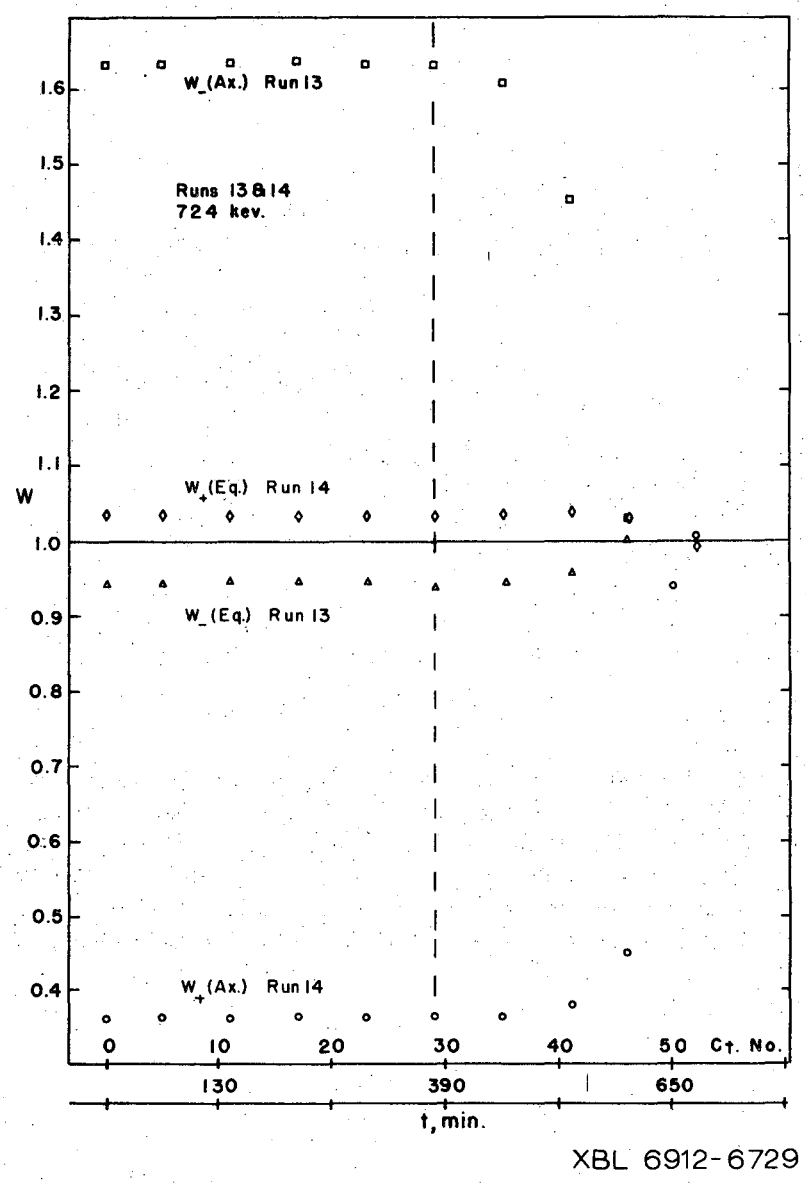

Fig. 21. Beta particle anisotropies from two ^{186}Re runs at 724 kev. as functions of count number (time). Only the anisotropies from every fifth count are shown. The anisotropies were constant for the first 5--6 hrs. of the runs because of saturation of the nuclear orientation. All anisotropies preceeding the vertical dotted line were averaged together to give final values for the two runs. The statistical errors were smaller than the plotted points.

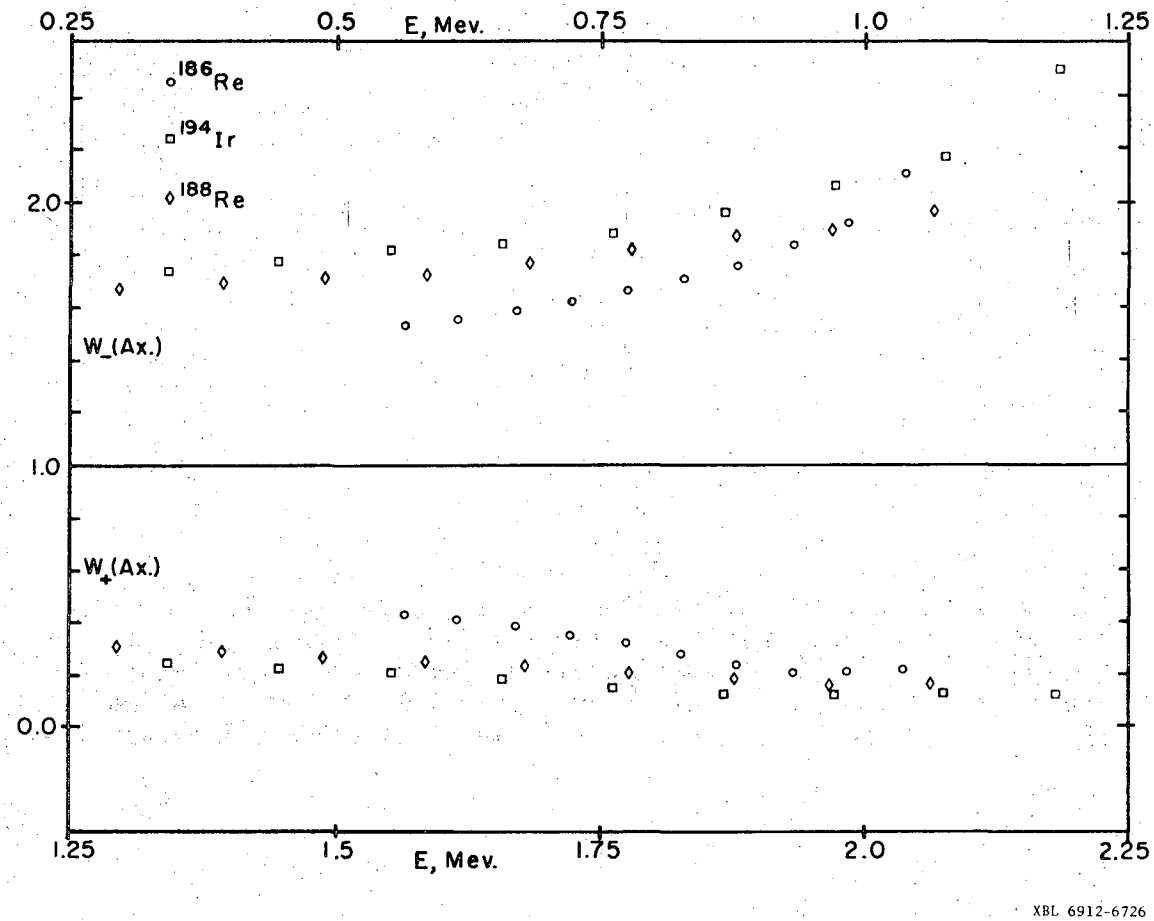

Fig. 22. Averaged beta particle anisotropy data (axial) from the three isotopes studied. The data were all taken below the saturation temperature. The lower energy scale applies to the ^{188}Re and ^{194}Ir data, while the upper scale refers to ^{186}Re. The statistical errors are in general smaller than the size of the plotted points.

ropies from a pair of runs which were comparable in all respects except for having opposite signs of the polarizing field H_o were combined and inserted into Eq. 18 in four different ways. (Cases I-IV; see first section of Chapter VII.) Runs 13 and 14 form such a pair. Consider the 724 kev. data from these runs, which were plotted in Fig. 21. The average values for all counts up to count 29 were computed and the results were: $W_+(Ax.) = .3653$; $W_-(Ax.) = 1.6380$; $W_+(Eq.) = 1.040$; and $W_-(Eq.) = .9432$. From Table II, and applying the corrections shown in Fig. 19, we get $\overline{P}_1^{\pm}(A) = \mp.8870$, $\overline{P}_2^{\pm}(A) = .7024$, $\overline{P}_1^{\pm}(E) = \pm.0956$, and $\overline{P}_2^{\pm}(E) = -.4548$. The signs refer to the field direction. The saturation values of B_1 and B_2 are 1.2247 and 0.7071, respectively, while at the warm count (LHe bath) temperature, B_1' has the value $B_1' = 0.0408$. Inserting these quantities into Eq. 18a gives (Case I):

$$A_1(r)\ \overline{P}_1^{+}(A) = C_1 = \frac{[1 + 1\ (.3653 - 1) - 1.6380]}{[.0408\ (-1.6380-.3653) + 1.2247(2)]}$$

$$= [-1.2727]/[-.0816 + 2.4494] = -.5375$$

Inserting the value of $\overline{P}_1^{+}(A)$ gives $A_1(r) = .6060$. Using other combinations of W's (Cases II--IV) one can check this value of $A_1(r)$. The results are:

Case II	$A_1(r)$	= .6057
Case III	$A_1(r)$	= .6078
Case IV	$A_1(r)$	= .6041
Average Cases I--IV	$\overline{A}_1(r)$	= .6059

By using Eq. 18b one can also calculate $A_2(r)$. In Appendix IC, the A_k's calculated with each case from various combinations of runs are listed, along with the average values from the four cases.

Finally, in order to get the final values of $A_1(r)$ and $A_2(r)$, weighted

averages of the $\overline{A}_k$'s listed in Appendix IC were calculated, with weighting according to the statistical errors in the input values of the anisotropies. The gamma anisotropies were also averaged and corrected to fit Eq. 23 where necessary (See Error Analysis section.), and were put into Eq. 16 using the calculated anisotropies for pure L=1 beta decays to give final values for R. The beta particle results are shown in Table IIIA and the gamma results are discussed further in a later section.

[Some note should be made of the fact that the calculated values of $\overline{P}_1(E)$ from Table II and Fig. 19 were not generally used in Eqs. 18 to derive the A_k's; this was because they were small and the errors in measurement and scattering corrections made them rather inaccurate. Instead, working values were obtained from the data and from the calculated $\overline{P}_1(A)$'s by using the relation

$$\overline{P}'_1(E) = \frac{[W_-(\text{Eq.}) - W_+(\text{Eq.})]}{[W_-(\text{Ax.}) - W_+(\text{Ax.})]} \overline{P}_1(A). \qquad (- \text{ field})$$

This tends to reduce the errors in the calculated A_k's as evidenced by a reduction in scatter among the four cases compared to the results using the calculated $\overline{P}_1(E)$'s. In the above example of Runs 13 and 14, the $\overline{P}'_1(E)$ obtained as above was -.0659 (- field) compared to the value from Table II and Fig. 19 of -.0956.]

Systematic Effects

Several types of systematic errors whose potential existence was mentioned in Chapter VII may now be discussed, making use of the listing of A_k's in Appendix IC. The first of these is a systematic shift with changing magnitude of H_o which might be caused by magnetic deflection of

Table IIIA: $A_1(r)$ and $A_2(r)$

^{186}Re			^{188}Re			^{194}Ir		
Energy	$A_1(r)$	$A_2(r)$	Energy	$A_1(r)$	$A_2(r)$	Energy	$A_1(r)$	$A_2(r)$
567	.5318	.0115	1199	.6318	.0518	1235	.6958	.1058
±5	±.0033	±.0016	±10	±.0049	±.0070	±10	±.0111	±.0223
619	.5544	.0122	1295	.6498	.0436	1340	.7142	.1229
±5	±.0034	±.0020	±10	±.0050	±.0115	±10	±.0114	±.0283
672	.5805	.0187	1391	.6658	.0559	1446	.7369	.1257
±5	±.0035	±.0022	±10	±.0052	±.0120	±10	±.0118	±.0295
724	.6074	.0227	1487	.6807	.0700	1551	.7516	.1082
±5	±.0036	±.0027	±10	±.0055	±.0070	±10	±.0120	±.0265
777	.6437	.0362	1583	.7028	.0730	1656	.7749	.1168
±5	±.0040	±.0030	±10	±.0056	±.0088	±10	±.0124	±.0292
830	.6809	.0371	1679	.7180	.0722	1761	.7964	.1076
±5	±.0042	±.0035	±10	±.0058	±.0145	±10	±.0128	±.0377
882	.7228	.0284	1775	.7525	.1008	1867	.8518	.1570
±5	±.0046	±.0080	±10	±.0058	±.0130	±10	±.0136	±.0565
935	.7804	.0364	1871	.7906	.0738	1972	.9015	.1433
±5	±.0048	±.0130	±10	±.0065	±.0280	±10	±.0162	±.0745
987	.8351	-.0075	1967	.8376	.0570	2077	.9505	.1971
±5	±.0053	±.0175	±10	±.0075	±.0400	±10	±.0210	±.1200
1040	.9473	-.0714	2063	.9237	-.0350	2182	1.1419	.1952
±5	±.0064	±.0200	±10	±.0097	±.0250	±10	±.0330	±.1500

Beta angular distribution coefficients $A_1(r)$ and $A_2(r)$, defined in Eqs. 13 and 14, Chapter VII. Particle energies are in kev.

the beta particles or by incomplete magnetization of the source foils. Runs were done at fields ranging from 1 koe. to 2 koe. in ^{188}Re and in ^{194}Ir, and to 1.5 koe. in the case of ^{186}Re. No systematic variation in the A_k's is attributable to the variation of H_o except the low values in Runs 9--12. The latter runs were made with a weak source and their statistics were poor, in any case. Both these pairs of runs were discarded in the calculation of the final A_k's given in Table IIIA. Since no comparable effects were found in the gamma anisotropies, it seems unlikely that incomplete magnetization was the cause; more likely the difficulty lay with the beta counters.

A second systematic effect is a shift in the values of the A_k's from different sources of the same isotope due to errors in measurement of the geometry or differences among the alloys used. The scatter observed was in fact considerably less than the estimated geometry errors on p. 98 for the case of $A_1(r)$. This was taken into consideration in obtaining the errors shown in Table IIIA. The scatter among $A_2(r)$ values from different sources was about the same as that expected from the estimated geometry errors in $\overline{P}_2(A,E)$. Thus it seems likely that any such scatter is attributable to geometry and that no systematic shifts were due to alloy preparation.

Finally, there are variations between the long and the short runs. Such shifts were expected in the gamma ray anisotropies because of the difficulties with the gamma-ray decay corrections mentioned earlier. Surprisingly, no significant differences were found except in the case of ^{194}Ir. Here the long runs 23 and 24 gave inconsistent gamma ray

anisotropies and these data were discarded. The only systematic discrepancy between long and short runs in the beta particle data was in Run 25, which gave unusually large values of the anisotropies which were constant with energy, unlike those from other runs. The energy effect suggests that the beta counter may have been at fault (the discrepancy occurs primarily in the axial anisotropies) and this is not surprising since there was difficulty with the axial counter heater at the end of the run and only four warm counts were taken. Consequently this run was not included in the averaging for the final A_k's.

Comparison with Previous Results

Both ^{186}Re and ^{188}Re have been investigated previously by nuclear orientation and other techniques. Fig. 23 shows a comparison of the ^{188}Re beta particle anisotropies from this work with those of Ref. 7, adjusted to saturation values. It can be seen that the two sets of data agree well for negative field directions (W_-(Ax.) $\equiv$ W(0)) but the Ref. 7 data are higher for positive field directions W(π) except at the lowest energies. The data from the present work are rather symmetric about the isotropy line, indicating a small A_2 term, while those of Ref. 7 are skewed upward, indication a large A_2 term. If one takes the reported values of the particle parameter ratios $[b_{1,1}^{(1)}/b_{1,1}^{(0)}]$ and $[b_{1,1}^{(2)}/b_{1,1}^{(0)}]$ from Ref. 7, along with the reported values of r, and calculates $A_1(r)$ and $A_2(r)$, the following results are obtained:

E, Mev.	$A_1(r)$		$A_2(r)$	
	This Work	Ref. 7	This Work	Ref.7
1.30	.650±.005	.64±.03	.044±.012	.12±.07
1.65	.718±.006	.76±.04	.072±.014	.27±.12

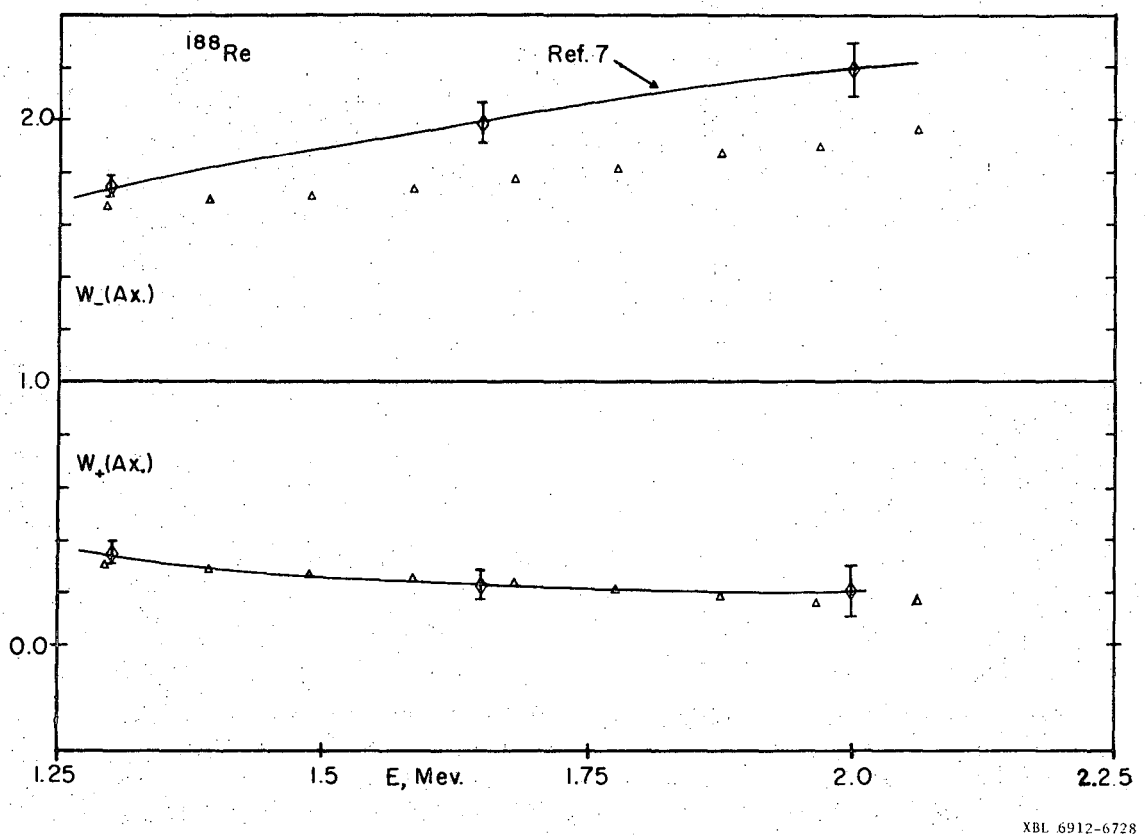

Fig. 23. Comparison of ^{188}Re beta particle anisotropies from this work with those observed in Ref. 7. The latter have been adusted to the saturation values. Errors on Ref. 7 points are statistical; statistical errors on points from this work are smaller than the plotted points.

As expected, the values of A_1 are in reasonable agreement, but the A_2's of Ref. 7 are larger, especially at high energies.

The ^{186}Re may be compared to results of Kogan et al (Ref. 48). Their results were presented in the form of measurements of the asymmetry α defined by

$$\alpha = \frac{W(0) - W(\pi)}{W(0) + W(\pi)} = A_1 B_1 / (1 + A_2 B_2)$$

which were made using alloys of ^{186}Re in iron in the high temperature region above 65 mdeg. K. (1/T = 15). In this region the B_2 term in the nuclear orientation formula is negligible within a percent or so and the B_1 term is proportional to 1/T. Ref. 48 contains a plot of α vs. 1/T for 900 kev. particle energy. Inserting the known value of B_1 gives A_1 from the above definition of α. In the second paper of Ref. 48 (Sott and Vinduska) the values of α at several other energies, 700 kev., 550 kev., and 450 kev., are also given. The comparison with the present work is as follows:

E, Mev.	$A_1(r)$	
	This Work	Ref. 48
.900	.738±.005	.78±.11
.700	.594±.004	.60
.550	.525±.003	.47

The errors for the lower energy points from Ref. 48 were not given but presumably they are comparable to those at 900 kev. Thus the two sets of data agree well.

No previous measurements of beta angular distributions from polarized

^{194}Ir exist. Both the A_1 and the A_2 found in this work for ^{194}Ir are larger than the comparable values for the Re isotopes. The fact that A_2 has a nonzero value indicates that ^{194}Ir does not obey the ξ approximation in its decay, which contradicts the early spectrum shape measurements (Ref. 51) which gave the allowed shape for the ^{194}Ir decays. It should be noted that in both the Re decays, A_2 changes sign above the $1^- \rightarrow 2^+$ transition endpoint, implying that A_2 for this transition is large and positive, while it is small and negative for the $1^- \rightarrow 0^+$ transition. This could happen as a result of the $\int B_{ij}$ term in the $1^- \rightarrow 2^+$ branch.[20] However, in the case of ^{194}Ir, A_2 increases monotonically with increasing energy.

Gamma Results

Table IIIB shows the gamma ray anisotropy results. The ^{186}Re anisotropy may be compared to that observed by Kogan et al.[59] They plot the square root of ε [$\varepsilon = (W(\pi/2) - W(0))/(\pi/2)$] against 1/T. From their plot one can derive the value of U_2F_2 for the 137 kev. gamma ray in the ^{186}Re decay, and finds $U_2F_2 = -0.27 \pm .02$. The value derived from Table IIIB is $U_2F_2 = -0.258 \pm 007$, in good agreement. Table IIIB also shows that a small but finite mixture of $\int B_{ij}$ is present in the $1^- \rightarrow 2^+$ beta decay in ^{186}Re, since the reported R is nonzero. This is in agreement with beta-gamma correlation and spectrum shape measurements.[71] It also implies that an analysis for the matrix elements which assumes no $\int B_{ij}$ term will be inadequate.

In the case of ^{188}Re, a somewhat larger value for R was found. Ref. 71 indicates that the relative sizes of the $\int B_{ij}$ matrix elements in the two decays is about the same, and thus the larger R for ^{188}Re is surprising.

Table IIIB: Gamma Ray Angular Distribution Results

Case	Quantity	^{186}Re	^{188}Re	^{194}Ir
I	W(Ax.)	.813±.017	.880±.016	-------
	R	.117±.073	.292±.062	
II	W(Ax.)	.829±.010	.893±.015	.816±.050
	R	.161±.042	.342±.063	<.044
III	W(Ax.)	.810±.024	.877±.020	-------
	R	.109±.063	.280±.077	
IV	W(Ax.)	.828±.005	.902±.016	.822±.040
	R	.158±.015	.380±.071	<.040

Values for the axial anisotropies and the [L = 2]/[L = 1] intensity ratio R are shown for the three decays using four different data analysis procedures. The cases listed in the first column are as follows:

Case I: Anisotropies determined using Method I as described in the text, and uncorrected to Eq. 23. In Method I, the anisotropy is calculated for the whole photopeak using the peak integration width A3 shown in Fig. 20. This method is potentially susceptible to errors from scattering (the Haag Effect; See Error Analysis.) and from faulty background corrections.

Case II: Similar to Case I but the anisotropies were corrected to fit Eq. 23, thus combining axial and equatorial data. This correction reduces the scatter among various runs and removes the effect of any incorrect decay correction or count-rate sensitivity in the counting systems.

Case III: Anisotropies calculated using Method II and uncorrected to Eq. 23. In Method II the photopeaks were divided into ten intervals and the anisotropies from each of the four intervals nearest the center of the peak were averaged. This method avoids errors from scattering and background corrections in the wings of the peak.

Case IV: Similar to Case III but with corrections to Eq. 23.

The errors shown were estimated from the scatter in the values from different runs; statistical errors were 5--10 times smaller. The values of the saturation anisotropies to be expected from pure L = 1 $1^- \rightarrow 2^+$ beta decays, used in calculating R, are as follows:

^{186}Re, W(Sat.,L=1) = 1. - (.3963±.0005) $\overline{U}_2$

^{188}Re, W(Sat.,L=1) = 1.0011 - (.3725±.0015) $\overline{U}_2$

^{194}Ir, W(Sat.,L=1) = $1.\left\{\begin{matrix}-.0103\\+.0285\end{matrix}\right\}$ -.2282 $\overline{U}_2$.

The large uncertainty in W(Sat.,L=1) for ^{194}Ir results from the aforementioned uncertainties in the mixing ratios and intensities of the unresolved gamma rays in the 300 kev. group. Because of these uncertainties and the rather large errors in W(Ax.) for this case, only upper limits for R are given in the table.

However, R is also dependent on the lepton functions as well as the matrix element ratios, so is is likely that the reported value does not contradict Ref. 64.

In the case of ^{194}Ir, R was found to be essentially zero. This is consistent with the fact that the A_2 term in the beta angular distribution from this isotope increased monotonically with energy, instead of decreasing sharply above the $1^- \rightarrow 2^+$ transition endpoint as did the A_2's found for the Re decays. It is also consistent with the results of Reid et al,[59] who assumed pure L = 1 for their calculation of $\overline{U}_2$ and obtained the magnetic moment of ^{194}Ir. The 328 kev. anisotropy from their work, adjusted to the low temperature saturation value, is 0.132±.019. The value from Table IIIB (Case IV) corrected for attenuation by the unresolved 293 kev. and 301 kev. gamma rays, is 0.21±.09, in agreement within the quoted errors although the latter are rather large.

Error Analysis

Errors in Anisotropies

The errors listed in Appendix I in connection with the measured beta and gamma anisotropies are statistical and were calculated by a computer program using the usual formula:

$$\Delta W = (1/NW) \cdot (\Delta NC + \Delta NW \cdot W)$$

where NC is the cold counting rate, NW is the warm counting rate, and W is the anisotropy (W = NC/NW). The errors in NC and NW were one standard deviation, i.e. $\Delta NC = \sqrt{NC}$. Allowance was also made for statistical errors in the background correction in the case of the gamma ray data.

The quoted errors in W do not contain any error due to the decay

correction. It is believed that such errors in the beta anisotropies are small, for the following reasons: 1) The values of the anisotropies from short runs, in which the decay correction was small (less than 5%) were in good agreement in general with the anisotropies from the long runs in which the decay corrections were much larger (up to 50%); 2) Decay curves made with the beta counting systems gave linear first-order plots out to four half-lives and gave values of the half-lives which were in good agreement with those listed in the Table of Isotopes (6th Ed.) and used to calculate the decay corrections; and 3) The anisotropies during the first 5 or 6 hours of the long runs, during which the nuclear orientation was constant (saturated), were constant within statistical error. (See Fig. 21.) If the decay corrections had been incorrect, the observed anisotropies would have changed with time even though the true anisotropy was constant. It is to be noted, however, that any error in the decay corrections would produce an effect similar to a B_2 term, i.e. it would shift the center of gravity of an anisotropy plot like that in Fig. 22 up or down from symmetry around the isotropy line, and thus the reported value of A_2 is particularly sensitive to such errors.

In the case of the gamma ray anisotropies, the decay correction is less reliable. As noted earlier, decay plots made with the gamma counting systems gave values of the half-lives which were about 20% high in the case of the shorter-lived isotopes. Thus the decay correction which was used in the data analysis was effectively too large, resulting in an artificial increase in the warm counting rate and a consequent enhancement of the observed axial anisotropy (where the cold count rate is less than the

warm rate) and an attenuation of the observed equatorial anisotropy (where the cold count rate is greater than the warm rate). Fortunately, there is only one temperature-dependent term in the gamma-ray anisotropy correlation function (Eq. 15) and thus a unique relation exists between W(Ax.) and W(Eq.), independently of any knowledge of the magnitudes of the individual anisotropies. This relation is the following:

$$\text{Eq. 23} \qquad 1 - W(\text{Ax.}) = 2[W(\text{Eq.}) - 1]$$

It may be seen from Appendix I that the gamma anisotropies observed in this work do not in general follow Eq. 23; W(Ax.) tends to be enhanced relative to W(Eq.), as expected from the above considerations of decay corrections. (Other possible causes of this effect are discussed at the end of this section.) Therefore, before the gamma anisotropy data were averaged together, they were corrected to obey Eq. 23, weighting the axial and the equatorial anisotropies equally. (See Table IIIB, notes). The correction was typically of the order of 4% and is included in the error limits on the quoted values of R.

Errors in Anisotropy Coefficients

The errors in the final values of the beta particle angular distribution coefficients $A_1(r)$ and $A_2(r)$ were estimated by using a set of trial input data in the computer program which calculated the coefficients from the anisotropies. Errors were introduced into the trial input values (which included four anisotropies from two counters and two field directions; three geometry coefficients $P_1(A)$, $P_2(A)$, and $P_2(E)$; and the orientation parameters $B_1(\text{sat.})$, $B_2(\text{sat.})$, and $B_1'(\text{warm})$.) The resulting errors in

the calculated average values of A_1 and A_2 were then obtained. Table IV summarizes these errors in three different energy regions.

The final errors listed in Table III contain both the statictical errors from the anisotropy measurements and also estimates of errors due to uncertainties in the orientation parameters and in the geometry coefficients. An examination of the scatter in A_1 and A_2 derived from measurements on different sources gives a check on the estimated errors. In the case of A_1, the statistical errors are typically in the range of 0.1--1.0%, the larger errors occurring at the higher energies. The scatter in A_1 from different sources is about 4--5 times smaller than the errors derived from the estimated 3% uncertainty in $\overline{P}_1(A)$; thus it is clear that the geometry errors were probably overestimated in this case, so the final errors include only a 1% uncertainty in $\overline{P}_1(A)$. In the case of A_2, the statistical errors contribute uncertainties in the range from 1%--30%, the latter value applying only to the highest-energy interval. The scatter is typically somewhat larger than indicated by the estimated geometry errors (10% in $P_2(A)$, 2.2% in $P_2(E)$) so it appears that these estimates were too small and the final errors in Table III were accordingly adjusted upward about 20%. The errors in gamma ray anisotropies in Table IIIB were arrived at by considering the scatter among various runs. The statistical errors of the uncorrected axial anisotropies (Cases I and III, Table IIIB) were only about 5% of the observed scatter. The scatter is decreased considerably when the anisotropies are adjusted to obey Eq. 23, which supports the validity of the adjustment. Probably the source of the scatter and of the deviations from Eq. 23 is a combination of decay correction

Table IV: Error Analysis for $A_1(r)$, $A_2(r)$

Input Error	Low Energy		Middle Energy		High Energy	
	$\Delta A_1(r)$	$\Delta A_2(r)$	$\Delta A_1(r)$	$\Delta A_2(r)$	$\Delta A_1(r)$	$\Delta A_2(r)$
1.0% incr. in $[1 - W_+(Ax)]$	+0.5%	-2.3%	+0.4%	-1.9%	+0.4%	-4.3%
1.0% incr. in $[W_-(Ax) - 1]$	+0.5%	+2.3%	+0.5%	+2.0%	+0.6%	+8.9%
.001--.01 incr. in W_+(Eq.)	----	-2.0%	----	-1.5%	----	-25%
.001--.002 incr. in W_-(Eq)	----	+2.2%	----	+2.2%	----	+5.5%
3.0% incr. in $\overline{P}_1(A)$	-2.7%	----	-2.7%	----	-2.7%	----
10 % incr. in $\overline{P}_2(A)$	----	-0.7%	----	-0.5%	----	-38%
2.2% incr. in $\overline{P}_2(E)$	----	-2.2%	----	-2.2%	----	-6.5%
10 % incr. in B_1'	+0.4%	+1.0%	+0.4%	+1.0%	+0.5%	+4.0%
2 % decr. in B_1(sat.)	+2.0%	+0.2%	+2.0%	+0.1%	+2.0%	+0.8%
6 % decr. in B_2(sat.)	----	+5.8%	----	+5.8%	----	+5.9%

(----) indicates that the error is less than 0.05%

(counter efficiency variation) and gain shift effects.

Some mention should be made of possible causes of the failure to obey Eq. 23 other than those mentioned above. These fall into four classes: first, there is the possibility that the source foils were incompletely magnetized, so that the axial symmetry of the nuclear orientation was not established and the angular distribution consequently had the wrong shape. This has been discussed earlier under Systematic Effects and can be ruled out. The second possibility is that the counters were not correctly located. The location of the source and the orientation of the polarizing field were checked several times, both by direct measurement when the cryostat was disassembled, and by measurement of the polarizing field outside the apparatus after assembly, using a rotating coil gaussmeter. Furthermore, the location of the gamma counters was unchanged from the Re experiments through the runs with ^{194}Ir, in which the maximum expected anisotropy was observed; thus no serious placement error could have been present.

A third possible explanation is scattering. The gamma rays were considerably scattered in emerging through the apparatus walls; this was especially true for the low energy gamma rays in the Re decays, as can be seen from the low energy tail on the peak in Fig. 20. Scattering mixes in photons emitted at the wrong angles and thus attenuates the anisotropy in both counters. This effect was previously investigated by J.N.Haag.[69] Furthermore, the photons entering the equatorial counter are more seriously scattered, since they have to pass through the polarizing magnet frame. In fact, the photopeak intensity in the equatorial gamma counter was usually

about 60% of that in the axial counter even though the two were at the same distance from the source. To check for this error, the data were analyzed by two methods, as explained previously. The data from Method I (A3) and from Method II agreed reasonably well, indicating that area A3 was sufficiently narrow to avoid scattering errors. The Haag Effect can be seen in the data from Method II in Appendix ID.

A fourth possibility to explain the discrepancy is gain shift, as mentioned above. NaI counters show considerable instability in the presence of magnetic fields and over long counting periods. Systematic gain shifts would cause errors in the calculation of the anisotropies (even though the peak maximum was re-located in the analysis of each spectrum, which to first order corrects for gain shifts). A more elaborate analysis of the data might reduce errors of this type, although it is probably not justified.

In view of the above considerations, it seems that the original explanation of decay correction--counter efficiency was the correct one, and that the adjustment of the anisotropies to fit Eq. 23 was valid.

Critique of Experiments

In the previous section, the derivation of the quoted error limits was discussed quantitatively. In this section, possible systematic errors in the measured quantities other than those already mentioned will be explored, along with potential improvements for future experiments of this type.

The quantities actually measured were the anisotropies $W(\theta)$. Using these quantities along with the orientation parameters B_k and the geometry

coefficients P_k, one can derive the desired quantities A_k and $\overline{U}_2$. The possible sources of error in the measurements of W are concerned with the counters: systematic changes in pulse height, resolution, or efficiency produced by changing count rates, magnetic fields, exchange gas addition or simply the passage of time, would produce corresponding errors in the measured W's. The beta counters used in these experiments were chosen for their stability, as well as for their large sensitive depths and good resolution. Since they were enclosed in vacuum tight holders, they were not sensitive to exchange gas. Most of the runs were done with constant magnetic fields throughout the run, and when the field was periodically reversed, care was taken to reproduce its magnitude exactly after each reversal. All runs were examined for changes in pulse-height and no systematic effects were found. One possible source of long-term changes in the beta detectors is radiation damage. A considerable literature on this subject exists and the evidence seems to indicate that lithium drifted counters are somewhat more sensitive to radiation damage than surface barrier detectors.[70] During these experiments, the most active sources used had decay rates of about 10^6/sec. and each counter subtended about 1% of the total solid angle around the source. Even assuming that a full strength source was in the cryostat at all times during the three months of the experiments, the integrated flux of electrons is less than $10^{11}/cm^2$ (and the actual value was probably a factor of 10 smaller than this number). This is about the threshold level at which damage might begin to appear. However, the pulse height and resolution were checked using ^{207}Bi before, during, and after the beta-decay experiments, and no

degradation was found. The detectors were periodically warmed to room temperature for a few minutes during the installation of each new source, which may have contributed to healing of radiation damage.

The gamma counters used were much more susceptible to drifts in pulse height with time and magnetic fields, as has been pointed out in the previous section. One improvement which could be made would be the use of Li-Ge gamma detectors. Not only are such detectors much more stable, they also have much better resolution, thereby simplifying background corrections and reducing the possibility of including scattered photons in the analysis. This type of detector is particularly important for the ^{194}Ir experiment, as has been discussed, and was used by other workers to investigate that decay.[59] The principal disadvantage of Li-Ge detectors is their relatively low efficiency, which makes the acquisition of sufficient counts to give good statistics more difficult. With an apparatus like the one used in these experiments, however, in which long runs of up to 12 hrs. are possible, this is not a serious difficulty.

Errors may also appear in the assumed values of the B_k's. This is not very important for the Re experiments, since there the B_k's were assumed to have their saturation values and the only relevant criterion was the constancy of the anisotropies, which was easily met. In the case of ^{194}Ir, owing to the analysis method used in which values of the ratio $B_1(\beta)/B_1(\text{sat.})$ were used to determine β, only knowledge of the functional form of B_1 was required and again, the results were independent of precise knowledge of μ, H_{hf}, or T. Working in the extreme low-temperature region is a great advantage since it not only eliminates the need for thermometry,

but also reduces the possibility of errors from thermal or magnetic inhomogeneities in the source foil. This in turn allows the use of thinner foils and backing materials, with a resulting reduction of scattering.

A third major source of errors is the calculation of the geometry coefficients $\overline{P}_k$. Errors in the measured geometry and errors due to scattering have already been discussed in Chapter VII. Every effort was made to reduce angular scattering in the present experiments, with some success, it is felt. Not much can be done to reduce backscatter--the only possibility seems to be the use of a rather large experimental chamber made of a light material, e.g.beryllium. Magnetic focussing might be useful in this connection but would make the interpretation of the data more difficult. Aside from measurement errors and scattering, the errors in the $\overline{P}_k$'s could arise from motion of the source after the measurement was made due to thermal contraction and expansion or to the field applied to cool the paramagnetic salt. A calculation of thermal expansion indicates that errors from this source are 0.1 mm or less, which is considerably less than the probable errors in measurement. The present apparatus was constructed with the source-heat link-salt pill assembly mounted on a tripod of graphite legs, so that if the source moved at all during installation of the cryostat into the dewar system, or during magnetization of the cooling salt, it should return to its original position after the distrubance ceased. It is apparent that the geometry measurement errors are predominant in experiments of this type, but since it is rather difficult to meet requirements for thermal isolation of the source and minimization of electron scattering and at the same time have the source

and the detectors mounted rigidly and reproducibly in a framework, it seems unlikely that major improvements can be made in this area. The use of a larger experimental chamber and larger detectors at greater distances from the source would of course reduce the precision of measurement required to give relative errors of a certain size and thus make it possible to improve the accuracy with which the geometry coefficients were known.

One can see by referring to the errors quoted in Table III that the coefficients $A_1(r)$ are by far the most accurately determined quantities from these experiments, and in fact their accuracy is a considerable improvement over earlier results. This is attributable to the use of two beta counters, to the use of very thin source foils and light source mounts to reduce scattering errors, and to the accumulation of a rather large quantity of data so that statistical errors were small. The coefficients $A_2(r)$ were not so accurately determined, although they are still an improvement over earlier results. Their relatively large errors are attributable to the aforementioned difficulties in the determination of the experimental geometry. Finally, the gamma ray anisotropies were the least accurately determined, due to the systematic effects discussed above. It is clear that the values of R labeled Case IV in Table IIIB are upper limits to the range in which the true value probably lies. Although the exact magnitudes of the values of R are not well determined, the trends are evident and the reported values can serve as a check on any future matrix element analysis for these decays. In particular, the reported values of R for ^{188}Re and ^{194}Ir are sensitive to details of the respective decay schemes.

Nuclear Matrix Element Analysis

The ultimate goal of this work is the determination of the nuclear matrix elements involved in the decays, or ratios of the matrix elements. For this purpose, the experimentally determined quantities $A_1(r)$, $A_2(r)$, and R must be subjected to an analysis procedure in combination with calculated lepton functions. Such analyses have been carried out in recent years for several first-forbidden decays.[7,48,71,72] The matrix element analysis is itself a project of considerable magnitude, usually requiring elaborate computer programs to calculate the lepton functions and determine the optimum values of the matrix elements to fit a given set of data; and always requiring a considerable knowledge of the current state of beta-decay theory. A natural division falls between the experimental determination of the observable quantities related to a decay, and the theoretical treatment of the observables to obtain the matrix elements. (Of course, it is advantageous for the analysis to be carried out by the same workers or at least in the same laboratory as the experiments.) For these reasons the present work does not extend to the analysis for the matrix elements, althcugh it is hoped that the analysis can be performed in the future.

References

Introduction

1) F. Bloch, Phys. Rev. 50, 472 (1936)

2) J.K.Knipp and G.E.Uhlenbeck, Physica 3, 425 (1936)

3) P. Morrison and L.I.Schiff, Phys. Rev. 58, 24 (1940)

4) H. Schopper and S. Galster, Nucl. Phys. 6, 125 (1958); also Phys. Rev. Lett. 4, 295 (1960)

5) R.P.Feynman and M. Gell-Mann, Phys. Rev. 109, 193 (1958)

6) C.S.Wu and S.A.Moszkowski, Beta Decay. Interscience, 1966. p. 274.

7) James E. Templeton, D.Phil thesis, Oxford, 1967 (unpublished).

8) B.N.Samoilov, V.V.Sklyarevskii, and E.P.Stepanov, JETP 9, 448, 1383 (1959); also JETP 11, 261 (1960)

Chapter I

9) D.A.Shirley in Hyperfine Structure and Nuclear Radiations, ed. E. Matthias and D.A.Shirley. North-Holland, 1968. pp. 979-984.

10) W.Brewer, D.A.Shirley, and J.E.Templeton, Phys. Lett. 27A, 81 (1968)

11) R.J.Blin-Stoyle and M.A.Grace, Handbuch der Physik, vol. 42, p.555 (1956)

12) S.R.DeGroot, H.A.Tolhoek, and W.J.Huiskamp in Alpha, Beta, and Gamma-Ray Spectroscopy, 2nd Ed., ed. K. Siegbahn. North-Holland, 1965. p.1199.

13) A.R.Rutledge, Chalk River Project report CRP-851 (1959) (unpublished)

14) H.I.West,Jr., Lawrence Radiation Laboratory report UCRL-5451 (1959) (unpublished)

Chapter II

15) E.J.Konopinski and M.E.Rose in Alpha, Beta, and Gamma-Ray Spectroscopy, 2nd Ed., ed. K. Siegbahn. North-Holland, 1965. p. 1333.

16) E.Fermi, Zeits. Phys. 88, 161 (1934)

17) E.C.G.Sudarshan and R.E.Marshak, Phys. Rev. 109, 1960 (1958)

18) J.J.Sakurai, Nuovo Cimento 7, 649 (1958)

19) K.Alder, B.Stech, and A.Winther, Phys. Rev. 107, 728 (1957)

20) H.A.Weidenmüller, Revs. Mod. Phys. 33, 574 (1961)

21) S.F.Timashev and V.A.Kaminskii, JETP 38, 284 (1960)

22) Y.Koh, D.Miyatake, and Y.Watanabe, Nucl. Phys. 32, 246 (1962)

23) P.C.Martin and R.J.Glauber, Phys. Rev. 109, 1307 (1958)

24) J.-I. Fujita, Phys. Rev. 126, 202 (1962)

25) J. Eichler, Zeits. Phys. 171, 463 (1962)

26) A.F.J.Siegert, Phys Rev. 52, 787 (1937)

27) T. Ahrens and E. Feenberg, Phys. Rev. 86, 64 (1952)

28) J. Damgaard and A. Winther, Phys. Lett. 23, 345 (1966)

29) M. Morita and R.S. Morita, Phys. Rev. 109, 2048 (1958); See also W. Bühring, Nucl.Phys. 40, 472 (1963) and Nucl. Phys. 61, 110 (1965)

Chapter III

30) G.A.Westenbarger and D.A.Shirley, Phys. Rev. 138, A161 (1965)

Chapter IV

31) J.L.Olsen, L.G.Mann, and M.Lindner, Phys. Rev. 106, 985 (1957)

32) C.M.Davisson in Alpha, Beta, and Gamma-Ray Spectroscopy, 2nd Ed. ed. K. Siegbahn. North-Holland, 1965. p. 49.

Chapter V

33) J.A.Barclay, W.Brewer, E.Matthias, and D.A.Shirley in Hyperfine Structure and Nuclear Radiations, ed. E. Matthias and D.A.Shirley. North-Holland, 1968. p. 902.

34) B.N.Samoilov, V.N.Agureev, V.D.Gorobchenko, V.V.Sklyarevskii, and O.A.Chilashvili, Proc. IX Intl. Conf. on Low Temperature Physics, Columbus, 1964. Plenum Press, 1965. p. 925.

35) M. Kontani and I. Itoh, J. Phys. Soc. Japan 22, 345 (1967)

36) G.J.Garrett, A.D.Jackson,Jr., and E.H.Rogers, Bull.Am. Phys. Soc. II 12, 509 (1967)

37) S.R.DeGroot et al, op. cit., p. 1258.

38) M. Vinduska and F.Janouch, Proc. 3rd Regional Conf. on Physics and Techniques of Low Temperatures, Prague, 1963

39) W.Brewer and D.A.Shirley, Phys. Rev. Lett. 20, 885 (1968)

Chapter VI

40) A.V.Pohm, W.E.Lewis, J.H.Talboy,Jr., and E.N.Jensen, Phys. Rev. 95, 1523 (1954)

41) H. Daniel, Nucl. Phys. 31, 293 (1962)

42) K.O.Nielsen and O.B.Nielsen, Nucl. Phys. 5, 319 (1958); E. Bashandy and M.S.El-Nesr, Nuovo Cimento 29, 1169 (1963).

43) F.T.Porter, M.S.Freeman, T.B.Novey, and F.Wagner,Jr. Phys Rev. 103, 921 (1956)

44) S. André and P. Liaud, J. Physique 29, 395 (1968); Compt. Rend. Ser.A, B 268, 270 (1969); S.Y.Vander Werf, H.DeWaard, and H.Beekhuis, Nucl. Phys. A134, 215 (1969)

45) H. Dulaney, C.H.Braden, E.T.Patronis, and L.D.Wyly, Phys. Rev. 129, 283 (1963); T.B.Novey, M.S.Freeman, F.T.Porter, and F.Wagner,Jr., Phys. Rev. 103, 942 (1956)

46) L.Grenacs, R.Hess, and F.C.Röhmer, Helv. Phys. Acta 38, 374 (1965); E.E.Habib and H . Ogata, Proc. Intl. Conf. on Properties of Nuclear States, Montreal, 1969.; M. Trundel, E.E.Habib, and H. Ogata, Phys. Rev. (to be published); L.D.Wyly, C.H.Braden, and H.Dulaney, Phys. Rev. 129, 315 (1963)

47) M. Delabaye, J. Deutsch, and P. Lipnik, Ann. de la Soc. Scient. de Bruxelles, 75 III, 171 (1962); F. Gygax and R. Hess, Helv. Phys. Acta 39, 209 (1966)

48) A.V.Kogan, V.D.Kul'kov, L.P.Nikitin, N.M.Reinov, M.S.Stel'makh and M. Sott, JEPT 16, 586 (1963); M. Sott and M.Vinduska, Nucl. Phys. 66, 144 (1965)

49) M. Sott, N.J.Stone, J.E.Templeton, and M. Vinduska, Phys. Lett. (to be published); see also Ref. 7.

50) A.I.Alikhanov, G.P.Eliseev, and V.A.Liubimov, JETP 34, 723 (1958); R. Löhken, H. Rebel, and G. Schatz, Zeits. Phys. 181, 396 (1964); D.M.Kaminker, G.I.Kharkevich, V.M.Lobashov, V.A.Nazarenko, L.F.Sayenko, and A.I.Yegorov, Nucl. Phys. 65, 43 (1965)

51) M.W.Johns and S.V.Nablo, Phys. Rev. 96, 1599 (1954)

52) J.D.Deutsch, L.Grenacs, and J. Lehmann, Kolloquium über Beta-Zerfall und schwache Wechselwirkungen, Heidelberg, 1965. p. 257.

53) J.A.Barclay, PhD thesis, Berkeley, 1969. (UCRL-18986, unpublished)

54) D.R.Bundrit and S.K.Sen, Nucl. Instr. and Meth. 34, 225 (1965)

55) E.M.Pell, Nat. Acad. Sci. Report NAS-NSS 32 Pub. 871, 139 (1961)

56) F.S.Goulding and D.Landis, Instr. Tech. in Nucl. Pulse Analysis, NAS-NRC Pub. 1184, II-18

57) M. Martini and T.A.McMath, to be published in Nucl. Instr. and Meth.; also E.Sakai and H.L.Malm, Appl. Phys. Lett. 10, 268 (1967)

Chapter VII

58) See, for example, T.Yamazaki, J. Sato, Y. Yokoyama, S. Baba, H. Ikegami and M. Sakai, UCRL-16996 (unpublished); Proc. Intl. Conf. on Nucl. Phys., Gatlinburg, Tenn., 1966.

59) The anisotropy of the 137 kev. gamma ray from polarized ^{186}Re was previously measured by A.V.Kogan, V.D.Kul'kov, L.P.Nikitin, I.A.Solokov, and M.S.Stel'makh, JEPT 13, 78 (1961). The anisotropy of the 328 kev. gamma from polarized ^{194}Ir was observed by P.G.E.Reid, M. Sott, and N.J.Stone, Nucl. Phys. A129, 273 (1969).

60) V.S.Shirley in Hyperfine Structure and Nuclear Radiations, ed. E. Matthias and D.A.Shirley. North-Holland, 1968. p. 985.

61) Table of Isotopes, 6th Ed., by C.M.Lederer, J.M.Hollander, and I. Perlman. J. Wiley and Sons, 1967

62) S.Alwyn and D.K.Butt, Nucl. Phys. A100, 177 (1967)

63) A.H.Wapstra, G.J.Nijgh, and R. VanLieshout, Nuclear Spectroscopy Tables. North-Holland, 1959. p. 31

64) A.T.Nelms, Energy Loss and Range of Electrons and Positrons. NBS Circular 577 (Supp.), 1958

65) E.J.Williams, Phys. Rev. 58, 292 (1940)

66) L.A.Kulchitsky and G.P.Latyshev, Phys. Rev. 61, 254 (1942)

67) W. Bothe, Z. Naturforschg. 4a, 542 (1949)

68) H. Frank, Z. Naturforschg. 14a, 247 (1959)

Chapter VIII

69) J.N.Haag, D.A.Shirley, and D.H.Templeton, Phys. Rev. 129, 1601 (1963); See also J.N.Haag, "Measurement of Plane Polarization of Gamma Radiation" UCRL-10880 (unpublished).

70) W.M.Gibson, G.L.Miller, and P.F.Donovan, in Alpha, Beta, and Gamma-Ray Spectroscopy, 2nd Ed. ed. K. Siegbahn. North-Holland, 1965. p. 345

71) S. André and P. Liaud, Nucl. Phys. A121, 337 (1968)

72) J.P.Deutsch and P. Lipnik, Nucl. Phys. 61, 97 (1965)

APPENDIX I

Tabulations of Experimental Results from First Forbidden Beta Decay Experiments

Appendix I A.: List of Experiments

Run #	Source	Polarizing Field	Length of Run
1[a]	^{186}Re alloy #1	± 1500 oe.	8 hrs.
2[a]	" " "	"	8 hrs.
3[a]	^{186} Re alloy #2	"	6 hrs.
4[b]	^{186} Re alloy #3	"	8 hrs.
5	" " "	"	12 hrs.
6[c]	" " "	"	10 hrs.
7	^{188} Re alloy #4	+ 2000 oe.	14 hrs.
8	" " "	- 2000 oe.	14 hrs.
9[d]	" " "	- 1500 oe.	12 hrs.
10[d]	" " "	+ 1500 oe.	11 hrs.
11[d]	^{188} Re alloy #5	+ 1000 oe.	12 hrs.
12[d]	" " "	- 1000 oe.	12 hrs.
13	^{186} Re alloy #6	- 1000 oe.	14 hrs.
14	" " "	+ 1000 oe.	13 hrs.
15	" " "	+ 1500 oe.	2 hrs.
16	" " "	+ 1500 oe.	12 hrs.
17	" " "	- 1500 oe.	13 hrs.
18	^{188} Re alloy #7	- 1500 oe.	2 hrs.
19	" " "	+ 1500 oe.	14 hrs.
20	" " "	- 1000 oe.	13 hrs.
21	" " "	+ 1000 oe.	14 hrs.
22	^{194} Ir alloy #8	+ 1500 oe.	2 hrs.
23	" " "	- 1500 oe.	14 hrs.
24	" " "	+ 1500 oe.	15 hrs.
25[e]	" " "	- 1500 oe.	2 hrs.

Footnotes to Appendix I A.:

a) Not used because of difficulties with apparatus and/or electronics.
b) Calibration run with additional ^{60}Co:Fe source.
c) First half of run lost because of faulty tape recording.
d) Beta angular distribution data not included in final averages.
e) Beta angular distribution data not used because of faulty axial counter.

Appendix I B.: Tabulation of Anisotropy Data(Gamma Analysis Method I)

The beta-particle and gamma-ray anisotropies for two counters are tabulated for each run (grouped by isotope studied) along with their statistical errors. The values listed are averages of the anisotropies recorded in all counts up to the point where temperature dependence began to appear (usually this included about 30 ten-minute counts for the beta anisotropies and 20--25 counts for the gamma anisotropies.). The anisotropies are defined by

$$W(Ax.) = \frac{\text{Cold Ct. Rate in Axial Counter}}{\text{Warm Ct. Rate in Axial Counter}} \quad \text{[corrected for decay]}$$

W(Eq.) = as above for equatorial counter.

The beta anisotropies are listed first, along with the corresponding particle energies. The second table on each page contains the gamma anisotropies for each of the three peak integration limits A1, A2, and A3, used in Method I. (See Chap. VII.)

RUN NUMBER 5 HO = 1600 OE.

ENERGY	W(AX.)	ERR.	W(EQ.)	ERR.
566.775	.46040	.00106	.99740	.00208
619.325	.43160	.00111	1.00250	.00233
671.875	.40300	.00119	.99910	.00264
724.425	.36830	.00127	.99450	.00307
776.975	.32980	.00140	1.00080	.00375
829.525	.28970	.00157	.99950	.00480
882.075	.25050	.00186	1.00060	.00643
934.625	.20840	.00229	.99150	.00936
987.175	.20630	.00356	.99190	.01555
1039.725	.22080	.00737	.87900	.03033

GAMMA ANISOTROPIES

A(I)	W(AX.)	ERR.	W(EQ.)	ERR.
A(1)	.82440	.00208	1.06640	.00507
A(2)	.81840	.00204	1.06110	.00496
A(3)	.81910	.00212	1.06070	.00540

RUN NUMBER 5 HC = -1600 OE.

ENERGY	W(AX.)	ERR.	W(EQ.)	ERR.
566.775	1.52540	.00190	.97030	.00506
619.325	1.55220	.00211	.96620	.00516
671.875	1.58170	.00238	.97530	.00571
724.425	1.61250	.00275	.96740	.00646
776.975	1.65390	.00329	.95510	.00733
829.525	1.69700	.00408	.97130	.00934
882.075	1.72390	.00525	.97330	.01233
934.625	1.82310	.00763	1.01270	.01865
987.175	1.80810	.01151	.83870	.02440
1039.725	1.84170	.02223	.79720	.05453

GAMMA ANISOTROPIES

A(I)	W(AX.)	ERR.	W(EQ.)	ERR.
A(1)	.81800	.00203	1.05700	.00466
A(2)	.81040	.00181	1.05300	.00434
A(3)	.80760	.00197	1.06400	.00483

RUN NUMBER 13 HO = -1000 OE.

ENERGY	W(AX.)	ERR.	W(EQ.)	ERR.
566.775	1.53400	.00059	.94940	.00102
619.325	1.56500	.00065	.94850	.00112
671.875	1.60100	.00074	.94320	.00124
724.425	1.63800	.00085	.94140	.00143
776.975	1.68500	.00101	.93590	.00169
829.525	1.74300	.00126	.93700	.00210
882.075	1.82400	.00164	.93830	.00275
934.625	1.91500	.00227	.93940	.00385
987.175	2.05600	.00339	1.01800	.00651
1039.725	2.31200	.00539	1.14700	.01143

GAMMA ANISOTROPIES

A(I)	W(AX.)	ERR.	W(EQ.)	ERR.
A(1)	.81130	.00054	1.02300	.00086
A(2)	.80030	.00055	1.03500	.00089
A(3)	.79190	.00059	1.05600	.00102

RUN NUMBER 14 HO = 1000 OE.

ENERGY	W(AX.)	ERR.	W(EQ.)	ERR.
566.775	.44290	.00028	1.03900	.00070
619.325	.41830	.00030	1.04200	.00078
671.875	.39230	.00032	1.04000	.00088
724.425	.36530	.00035	1.03600	.00102
776.975	.33290	.00039	1.04100	.00124
829.525	.29730	.00045	1.04000	.00155
882.075	.26370	.00054	1.05000	.00208
934.625	.24050	.00069	1.04900	.00294
987.175	.24000	.00100	1.06700	.00461
1039.725	.24890	.00160	1.09600	.00752

GAMMA ANISOTROPIES

A(I)	W(AX.)	ERR.	W(EQ.)	ERR.
A(1)	.84900	.00059	1.06600	.00092
A(2)	.83960	.00060	1.07300	.00096
A(3)	.83650	.00065	1.08400	.00107

RUN NUMBER 15 HO = 1500 OE.

ENERGY	W(AX.)	ERR.	W(EQ.)	ERR.
566.775	.43810	.00070	1.04100	.00167
619.325	.41110	.00074	1.04400	.00186
671.875	.37980	.00079	1.04600	.00211
724.425	.34860	.00086	1.04600	.00245
776.975	.31580	.00093	1.04400	.00294
829.525	.27860	.00109	1.04600	.00371
882.075	.23960	.00128	1.05100	.00495
934.625	.21370	.00164	1.04700	.00705
987.175	.20860	.00240	1.05000	.01130
1039.725	.20970	.00383	1.05500	.01891

GAMMA ANISOTROPIES

A(I)	W(AX.)	ERR.	W(EQ.)	ERR.
A(1)	.85080	.00144	1.07300	.00223
A(2)	.84030	.00147	1.08500	.00232
A(3)	.83090	.00158	1.10200	.00262

RUN NUMBER 16 HC = 1500 OE.

ENERGY	W(AX.)	ERR.	W(EQ.)	ERR.
566.775	.43350	.00033	1.03500	.00081
619.325	.40540	.00035	1.03600	.00090
671.875	.37730	.00038	1.03500	.00102
724.425	.34560	.00041	1.03800	.00120
776.975	.31120	.00045	1.03300	.00143
829.525	.27360	.00051	1.03400	.00180
882.075	.23460	.00060	1.04000	.00241
934.625	.21040	.00077	1.04800	.00348
987.175	.20720	.00115	1.05700	.00566
1039.725	.21140	.00191	1.09600	.01011

GAMMA ANISOTROPIES

A(I)	W(AX.)	ERR.	W(EQ.)	ERR.
A(1)	.81370	.00067	1.04900	.00107
A(2)	.80180	.00068	1.05600	.00111
A(3)	.79640	.00073	1.06700	.00125

RUN NUMBER 17 HO = -1500 OE.

ENERGY	W(AX.)	ERR.	W(EQ.)	ERR.
566.775	1.53600	.00067	.96880	.00150
619.325	1.56300	.00073	.95680	.00160
671.875	1.59400	.00082	.95040	.00176
724.425	1.62400	.00095	.94680	.00199
776.975	1.66600	.00113	.93920	.00232
829.525	1.71400	.00141	.92710	.00283
882.075	1.76200	.00184	.93700	.00377
934.625	1.81700	.00258	.92750	.00535
987.175	1.90500	.00407	.96000	.00938
1039.725	2.20500	.00791	1.08600	.02327

GAMMA ANISOTROPIES

A(I)	W(AX.)	ERR.	W(EQ.)	ERR.
A(1)	.79670	.00057	1.01400	.00094
A(2)	.78440	.00058	1.01800	.00097
A(3)	.77870	.00062	1.02300	.00109

RUN NUMBER 7 HO = 2000 OE.

ENERGY	W(AX.)	ERR.	W(EQ.)	ERR.
1199.475	1.63700	.00158	.93830	.00139
1295.425	1.66300	.00175	.93850	.00154
1391.375	1.69600	.00197	.92780	.00173
1487.325	1.71400	.00226	.93620	.00199
1583.275	1.73900	.00268	.92850	.00235
1679.225	1.75300	.00331	.91510	.00289
1775.175	1.83200	.00446	.91390	.00377
1871.125	1.84800	.00628	.91290	.00528
1967.075	1.96900	.01063	.90780	.00840
2063.025	2.15200	.02177	.93450	.01614

GAMMA ANISOTROPIES

A(I)	W(AX.)	ERR.	W(EQ.)	ERR.
A(1)	.87180	.00107	1.02200	.00185
A(2)	.86840	.00105	1.02000	.00187
A(3)	.87150	.00111	1.02000	.00204

RUN NUMBER 8 HO = -2000 DE.

ENERGY	W(AX.)	ERR.	W(EQ.)	ERR.
1199.475	.33370	.00063	1.01300	.00298
1295.425	.31330	.00067	1.01200	.00315
1391.375	.29590	.00074	1.01500	.00346
1487.325	.27760	.00081	1.00600	.00383
1583.275	.25980	.00093	1.01200	.00450
1679.225	.24170	.00109	1.01800	.00534
1775.175	.21570	.00139	1.01700	.00706
1871.125	.18840	.00187	1.01800	.00989
1967.075	.17130	.00306	1.05000	.01610
2063.025	.20040	.00708	1.10300	.03319

GAMMA ANISOTROPIES

A(I)	W(AX.)	ERR.	W(EQ.)	ERR.
A(1)	.89550	.00128	1.01500	.00229
A(2)	.89210	.00124	1.02000	.00231
A(3)	.89410	.00133	1.02900	.00252

RUN NUMBER 9 HO = -1500 OE.

ENERGY	W(AX.)	ERR.	W(EQ.)	ERR.
1199.475	1.62400	.00276	.93940	.00433
1295.425	1.65300	.00307	.93160	.00479
1391.375	1.66800	.00345	.91700	.00528
1487.325	1.71700	.00405	.92720	.00609
1583.275	1.69300	.00466	.91660	.00735
1679.225	1.72800	.00581	.90550	.00901
1775.175	1.77600	.00775	.87550	.01203
1871.125	1.81200	.01120	.88140	.01658
1967.075	1.73600	.01762	.83880	.02528
2063.025	1.69000	.03648	1.01700	.05616

GAMMA ANISOTROPIES

A(I)	W(AX.)	ERR.	W(EQ.)	ERR.
A(1)	.88500	.00226	1.01900	.00439
A(2)	.88460	.00221	1.03600	.00435
A(3)	.89610	.00236	1.06900	.00488

RUN NUMBER 10 HO = 1500 OE.

ENERGY	W(AX.)	ERR.	W(EQ.)	ERR.
1174.775	.36080	.00173	1.00800	.00411
1273.325	.34210	.00183	1.01100	.00456
1371.875	.31500	.00193	1.03100	.00523
1470.425	.29550	.00209	1.00900	.00586
1568.975	.27810	.00233	1.02600	.00702
1667.525	.26040	.00271	1.02400	.00848
1766.075	.23250	.00316	.99570	.01051
1864.625	.20730	.00394	.99220	.01434
1963.175	.18020	.00551	1.06100	.02332
2061.725	.15310	.00848	.97780	.03619

GAMMA ANISOTROPIES

A(I)	W(AX.)	ERR.	W(EQ.)	ERR.
A(1)	.84970	.00393	1.26300	.01300
A(2)	.83110	.00369	1.10000	.00980
A(3)	.82530	.00397	1.04900	.00986

RUN NUMBER 11 HC = 1000 OE.

ENERGY	W(AX.)	ERR.	W(EQ.)	ERR.
1174.775	.35970	.00172	.97770	.00416
1273.325	.34550	.00183	.96030	.00452
1371.875	.32140	.00187	.97010	.00515
1470.425	.30050	.00207	.96330	.00586
1568.975	.28370	.00231	.97020	.00699
1667.525	.27090	.00269	.98350	.00866
1766.075	.24120	.00308	.93230	.01043
1864.625	.22480	.00398	.94420	.01468
1963.175	.18970	.00528	1.00400	.02383
2061.725	.18180	.00854	1.02800	.04328

GAMMA ANISOTROPIES

A(I)	W(AX.)	ERR.	W(EQ.)	ERR.
A(1)	.90450	.00496	1.16900	.01336
A(2)	.89410	.00470	1.10900	.01115
A(3)	.88630	.00490	1.09700	.01141

RUN NUMBER 12 HO = -1000 OE.

ENERGY	W(AX.)	ERR.	W(EQ.)	ERR.
1199.475	1.62800	.00631	.97150	.00800
1295.425	1.62600	.00687	.95970	.00875
1391.375	1.67500	.00792	.96500	.00989
1487.325	1.65400	.00883	.95910	.01127
1583.275	1.67600	.01054	.97740	.01361
1679.225	1.74300	.01342	.96120	.01643
1775.175	1.80000	.01795	.93050	.02091
1871.125	1.87400	.02640	.89730	.02842
1967.075	1.73400	.03978	.92880	.04595
2063.025	1.32700	.06220	1.37600	.12663

GAMMA ANISOTROPIES

A(I)	W(AX.)	ERR.	W(EQ.)	ERR.
A(1)	1.00700	.01451	1.28000	.03865
A(2)	.91170	.01079	1.11000	.02633
A(3)	.89190	.01067	1.06200	.02507

RUN NUMBER 18 HO = -1500 OE.

ENERGY	W(AX.)	ERR.	W(EQ.)	ERR.
1199.475	1.68200	.00279	.99130	.00412
1295.425	1.70900	.00307	.99840	.00456
1391.375	1.73300	.00346	.99440	.00508
1487.325	1.75700	.00397	.98860	.00581
1583.275	1.78000	.00472	.98650	.00687
1679.225	1.80600	.00586	.98550	.00851
1775.175	1.86000	.00786	.97910	.01110
1871.125	1.92300	.01157	.99270	.01631
1967.075	2.04700	.01980	1.00100	.02779
2063.025	2.52100	.04323	.93630	.05595

GAMMA ANISOTROPIES

A(I)	W(AX.)	ERR.	W(EQ.)	ERR.
A(1)	.90060	.00240	1.02600	.00356
A(2)	.89710	.00239	1.02800	.00365
A(3)	.89410	.00252	1.02900	.00401

RUN NUMBER 19 HO = 1500 OE.

ENERGY	W(AX.)	ERR.	W(EQ.)	ERR.
1199.475	.29260	.00056	.96660	.00165
1295.425	.27520	.00059	.96290	.00183
1391.375	.25770	.00064	.96300	.00208
1487.325	.23850	.00069	.95590	.00240
1583.275	.22370	.00079	.96360	.00289
1679.225	.19940	.00091	.95870	.00360
1775.175	.17500	.00112	.94480	.00470
1871.125	.14360	.00147	.97060	.00711
1967.075	.12540	.00236	.95600	.01196
2063.025	.15730	.00612	1.07720	.02847

GAMMA ANISOTROPIES

A(I)	W(AX.)	ERR.	W(EQ.)	ERR.
A(1)	.90120	.00152	1.03400	.00217
A(2)	.89670	.00151	1.02500	.00220
A(3)	.89400	.00159	1.01700	.00239

RUN NUMBER 20 HO = -1000 OE.

ENERGY	W(AX.)	ERR.	W(EQ.)	ERR.
1199.475	1.66500	.00194	.99390	.00256
1295.425	1.69400	.00214	.99860	.00284
1391.375	1.70800	.00240	.98560	.00315
1487.325	1.73000	.00276	.98610	.00363
1583.275	1.76700	.00331	.97700	.00428
1679.225	1.78400	.00410	.98800	.00537
1775.175	1.81500	.00545	.97900	.00708
1871.125	1.89600	.00826	1.00100	.01055
1967.075	1.93900	.01436	1.01900	.01865
2063.025	2.13800	.03613	1.10800	.04822

GAMMA ANISOTROPIES

A(I)	W(AX.)	ERR.	W(EQ.)	ERR.
A(1)	.88480	.00190	1.02300	.00289
A(2)	.88320	.00191	1.02400	.00294
A(3)	.88870	.00203	1.03700	.00328

RUN NUMBER 21 HO = 1000 OE.

ENERGY	W(AX.)	ERR.	W(EQ.)	ERR.
1174.775	.31650	.00120	.96730	.00348
1273.325	.29870	.00126	.99960	.00401
1371.875	.27820	.00132	.98860	.00445
1470.425	.25690	.00141	.96000	.00497
1568.975	.24480	.00160	.96590	.00589
1667.525	.22650	.00183	.97850	.00731
1766.075	.20340	.00216	.93790	.00904
1864.625	.17790	.00272	.97150	.01300
1963.175	.14010	.00362	1.00800	.02184
2061.725	.14050	.00711	1.08400	.04844

GAMMA ANISOTROPIES

A(I)	W(AX.)	ERR.	W(EQ.)	ERR.
A(1)	.84200	.00382	1.00900	.00622
A(2)	.83510	.00377	.98510	.00606
A(3)	.84060	.00409	.98420	.00665

RUN NUMBER 22 HO = 1500 OE.

ENERGY	W(AX.)	ERR.	W(EQ.)	ERR.
1235.125	.28930	.00134	.98570	.00375
1340.375	.26940	.00141	.98700	.00423
1445.625	.24930	.00151	.97370	.00481
1550.875	.22630	.00165	.98890	.00576
1656.125	.20090	.00182	.98030	.00698
1761.375	.17510	.00208	.99660	.00905
1866.625	.14180	.00240	1.00100	.01232
1971.875	.13900	.00335	1.00100	.01872
2077.125	.13980	.00555	.97770	.03375
2182.375	.13530	.01151	.97430	.07471

GAMMA ANISOTROPIES

A(I)	W(AX.)	ERR.	W(EQ.)	ERR.
A(1)	.85400	.00144	1.05900	.00193
A(2)	.85240	.00153	1.06300	.00212
A(3)	.84010	.00174	1.06600	.00242

RUN NUMBER 23 HO = -1500 OE.

ENERGY	W(AX.)	ERR.	W(EQ.)	ERR.
1235.125	1.70500	.00184	.93070	.00251
1340.375	1.73900	.00206	.91180	.00273
1445.625	1.78000	.00236	.91680	.00313
1550.875	1.82100	.00276	.91890	.00368
1656.125	1.84500	.00329	.90480	.00437
1761.375	1.88700	.00410	.92210	.00568
1866.625	1.96100	.00552	.90320	.00756
1971.875	2.06700	.00821	.90660	.01150
2077.125	2.17700	.01421	.83160	.01974
2182.375	2.56700	.03552	.92770	.05271

GAMMA ANISOTROPIES

A(I)	W(AX.)	ERR.	W(EQ.)	ERR.
A(1)	.74550	.00130	.91320	.00176
A(2)	.74800	.00141	.92680	.00194
A(3)	.73700	.00162	.93550	.00195

RUN NUMBER 24 HO = 1500 OE.

ENERGY	W(AX.)	ERR.	W(EQ.)	ERR.
1235.125	.27260	.00097	.93930	.00280
1340.375	.25790	.00103	.92100	.00310
1445.625	.23610	.00110	.94290	.00367
1550.875	.21050	.00118	.93230	.00428
1656.125	.18330	.00129	.93390	.00524
1761.375	.15910	.00147	.93000	.00663
1866.625	.13490	.00174	.96130	.00941
1971.875	.12740	.00243	.88850	.01310
2077.125	.13260	.00429	.90530	.02537
2182.375	.12460	.00902	1.05000	.07463

GAMMA ANISOTROPIES

A(I)	W(AX.)	ERR.	W(EQ.)	ERR.
A(1)	.61070	.00149	.84330	.00228
A(2)	.61550	.00161	.84410	.00249
A(3)	.60000	.00180	.83760	.00282

RUN NUMBER 25 HO = -1500 OE.

ENERGY	W(AX.)	ERR.	W(EQ.)	ERR.
1235.125	2.10600	.00891	.94730	.00953
1340.375	2.17700	.01016	.93730	.01049
1445.625	2.20400	.01151	.94670	.01200
1550.875	2.24800	.01349	.94910	.01418
1656.125	2.35300	.01672	.95580	.01712
1761.375	2.38500	.02079	.94180	.02159
1866.625	2.46200	.02790	.87480	.02706
1971.875	2.54600	.04136	.94150	.04460
2077.125	2.48000	.06769	.98290	.08613
2182.375	2.44900	.15662	.86600	.18542

GAMMA ANISOTROPIES

A(I)	W(AX.)	ERR.	W(EQ.)	ERR.
A(1)	.75330	.00182	1.04800	.00285
A(2)	.76090	.00200	1.05600	.00317
A(3)	.75950	.00235	1.07200	.00374

Appendix I C.: Beta Particle Angular Distribution Coefficients

The angular distribution coefficients derived from pairs of runs with opposite signs of the polarizing field H_o are listed as functions of particle energy. The anisotropies from the two runs are combined in four different ways denoted as Cases I--IV (See Chap. VII.) to give four values for A_1 and A_2. The averages of the four values are also given in the tables. The averages were combined with weighting from appropriate runs to give the final averages shown in Table IIIA, p.114. The coefficients are defined as functions of particle parameters and the ratio r of intensities of the two beta branches [$r = I(1^- \rightarrow 2^+)/I(1^- \rightarrow 0^+)$]:

$$A_1(r) = -\frac{\{b^{(1)}_{1,1}/b^{(0)}_{1,1}\}}{[1+r]} + \frac{r}{2[1+r]} \times \frac{\{b^{(1)}_{1,1} - 3/\sqrt{5}\, b^{(1)}_{1,2} + 1/\sqrt{5}\, b^{(1)}_{2,2}\}}{[b^{(0)}_{1,1} - \sqrt{3/5}\, b^{(0)}_{2,2}]}$$

$$A_2(r) = \frac{\{b^{(2)}_{1,1}/b^{(0)}_{1,1}\}}{[1+r]} + \frac{r}{10[1+r]} \times \frac{\{b^{(2)}_{1,1} - 3\, b^{(2)}_{1,2} + \sqrt{21}\, b^{(2)}_{2,2}\}}{[b^{(0)}_{1,1} - \sqrt{3/5}\, b^{(0)}_{2,2}]}$$

For completeness we also give the definition of the parameter R, from the gamma ray attenuation data, whose values are listed in Table IIIB, p.120.:

$$R = -\sqrt{3/5}\ \{b^{(0)}_{2,2}/b^{(0)}_{1,1}\}$$

RUN NUMBERS 5 AND 5

A1 CALCULATION

ENERGY	CASE I	CASE II	CASE III	CASE IV	AVERAGES
566.8	.52692	.52676	.54701	.50606	.52669
619.3	.55121	.55107	.57082	.53081	.55098
671.9	.57700	.57690	.59063	.56279	.57683
724.4	.60658	.60638	.62946	.58267	.60627
777.0	.64363	.64332	.66780	.61829	.64326
829.5	.68260	.68242	.69255	.67216	.68243
882.1	.71323	.71323	.72533	.70049	.71307
934.6	.78131	.78094	.74321	.82154	.78175
987.2	.77407	.77163	.87102	.67143	.77204
1039.7	.78348	.77830	.95825	.59864	.77967

A2 CALCULATION

ENERGY	CASE I	CASE II	CASE III	CASE IV	AVERAGES
566.8	.00601	.05095	.05260	.05264	.04055
619.3	.00602	.04902	.05105	.05111	.03930
671.9	.00949	.03986	.04075	.04077	.03272
724.4	.00816	.05901	.06061	.06065	.04711
777.0	.01516	.06794	.07062	.07069	.05610
829.5	.02265	.04484	.04548	.04549	.03962
882.1	.01281	.03995	.04066	.04070	.03353
934.6	.08302	-.00643	-.00486	-.00474	.01675
987.2	.06365	.25750	.28749	.28789	.22413
1039.7	.11713	.49220	.52092	.52096	.41280

RUN NUMBERS 13 AND 14

A1 CALCULATION

ENERGY	CASE I	CASE II	CASE III	CASE IV	AVERAGES
566.8	.52695	.52706	.53780	.51559	.52685
619.3	.55067	.55074	.55520	.54591	.55063
671.9	.57774	.57764	.58160	.57372	.57767
724.4	.60599	.60572	.60784	.60413	.60592
777.0	.64203	.64157	.63468	.64990	.64205
829.5	.68523	.68448	.66398	.70790	.68540
882.1	.73883	.73756	.68111	.80050	.73950
934.6	.79273	.79044	.69789	.89443	.79387
987.2	.86095	.85781	.62969	1.10819	.86416
1039.7	.98202	.97662	.53601	1.45961	.98856

A2 CALCULATION

ENERGY	CASE I	CASE II	CASE III	CASE IV	AVERAGES
566.8	-.00269	.01815	.02104	.02124	.01443
619.3	.00607	.01470	.01589	.01599	.01317
671.9	.01870	.02601	.02704	.02704	.02470
724.4	.03142	.03490	.03541	.03528	.03425
777.0	.04959	.03545	.03370	.03333	.03802
829.5	.07644	.03518	.03043	.02973	.04294
882.1	.12976	.01765	.00454	.00297	.03873
934.6	.20387	.01746	-.00217	-.00468	.05362
987.2	.35292	-.13002	-.14993	-.15191	-.01973
1039.7	.63498	-.37085	-.33571	-.33240	-.10099

RUN NUMBERS 15 AND 15

A1 CALCULATION

ENERGY	CASE I	CASE II	CASE III	CASE IV	AVERAGES
566.8	0.	0.	.53960	0.	.53960
619.3	0.	0.	.55950	0.	.55950
671.9	0.	0.	.58480	0.	.58480
724.4	0.	0.	.60870	0.	.60870
777.0	0.	0.	.64740	0.	.64740
829.5	0.	0.	.67330	0.	.67330
882.1	0.	0.	.70370	0.	.70370
934.6	0.	0.	.72560	0.	.72560
987.2	0.	0.	.68400	0.	.68400
1039.7	0.	0.	.62540	0.	.62540

A2 CALCULATION

ENERGY	CASE I	CASE II	CASE III	CASE IV	AVERAGES
566.8	0.	0.	.01520	0.	.01520
619.3	0.	0.	.01080	0.	.01080
671.9	0.	0.	.00920	0.	.00920
724.4	0.	0.	.00440	0.	.00440
777.0	0.	0.	.02770	0.	.02770
829.5	0.	0.	.01400	0.	.01400
882.1	0.	0.	.00660	0.	.00660
934.6	0.	0.	.01010	0.	.01010
987.2	0.	0.	-.09310	0.	-.09310
1039.7	0.	0.	-.21770	0.	-.21770

RUN NUMBERS 16 AND 17

A1 CALCULATION

ENERGY	CASE I	CASE II	CASE III	CASE IV	AVERAGES
566.8	.53239	.53270	.53426	.53038	.53243
619.3	.55576	.55600	.56595	.54505	.55569
671.9	.58134	.58148	.59469	.56731	.58121
724.4	.60835	.60851	.62164	.59434	.60821
777.0	.64286	.64280	.66037	.62442	.64261
829.5	.68210	.68179	.70099	.66220	.68177
882.1	.72211	.72187	.72125	.72309	.72208
934.6	.75890	.75822	.74102	.77813	.75907
987.2	.80236	.80104	.70804	.90322	.80367
1039.7	.94656	.94272	.59378	1.32489	.95199

A2 CALCULATION

ENERGY	CASE I	CASE II	CASE III	CASE IV	AVERAGES
566.8	-.00992	-.00614	-.00583	-.00568	-.00689
619.3	-.00870	.01115	.01338	.01361	.00736
671.9	-.00324	.02263	.02563	.02586	.01772
724.4	-.00227	.02341	.02646	.02671	.01858
777.0	.00885	.04278	.04674	.04693	.03632
829.5	.02337	.05967	.06430	.06441	.05294
882.1	.03681	.03506	.03493	.03479	.03540
934.6	.07187	.03716	.03298	.03230	.04358
987.2	.16188	-.02624	-.04343	-.04519	.01175
1039.7	.48540	-.27770	-.28335	-.28389	-.08989

RUN NUMBERS 7 AND 8

A1 CALCULATION

ENERGY	CASE I	CASE II	CASE III	CASE IV	AVERAGES
1199.5	.62746	.62725	.66513	.58793	.62694
1295.4	.64429	.64400	.67831	.60855	.64379
1391.4	.66471	.66414	.69532	.63253	.66417
1487.3	.67969	.67911	.70912	.64872	.67916
1583.3	.69849	.69779	.72470	.67090	.69797
1679.2	.71246	.71170	.74586	.67722	.71181
1775.2	.76189	.76036	.76700	.75679	.76151
1871.1	.78153	.78011	.79099	.77176	.78110
1967.1	.84775	.84508	.77891	.92239	.84853
2063.0	.92371	.91869	.67629	1.19288	.92789

A2 CALCULATION

ENERGY	CASE I	CASE II	CASE III	CASE IV	AVERAGES
1199.5	-.00005	.07410	.08097	.08125	.05907
1295.4	.00771	.07501	.08095	.08117	.06121
1391.4	.02568	.08559	.09172	.09183	.07370
1487.3	.02711	.08617	.09077	.09084	.07372
1583.3	.03640	.08838	.09317	.09318	.07778
1679.2	.03395	.09911	.10643	.10653	.08650
1775.2	.09245	.10222	.10355	.10294	.10029
1871.1	.08363	.10205	.10422	.10372	.09841
1967.1	.19557	.06192	.04549	.04263	.08640
2063.0	.41746	-.05617	-.12171	-.13073	.02721

RUN NUMBERS 9 AND 10

A1 CALCULATION

ENERGY	CASE I	CASE II	CASE III	CASE IV	AVERAGES
1199.5	.60830	.60791	.64254	.57247	.60781
1295.4	.62597	.62541	.65777	.59266	.62545
1391.4	.64225	.64186	.67569	.60706	.64171
1487.3	.67288	.67199	.69711	.64748	.67236
1583.3	.66781	.66748	.70927	.62406	.66715
1679.2	.69178	.69108	.73311	.64818	.69104
1775.2	.72709	.72537	.80062	.64941	.72562
1871.1	.75545	.75356	.81866	.68865	.75408
1967.1	.73084	.73064	.84007	.61381	.72884
2063.0	.72106	.72294	.77578	.66361	.72085

A2 CALCULATION

ENERGY	CASE I	CASE II	CASE III	CASE IV	AVERAGES
1199.5	.01245	.08007	.08602	.08617	.06618
1295.4	.02482	.08699	.09322	.09331	.07458
1391.4	.01454	.07765	.08665	.08694	.06644
1487.3	.04726	.09508	.09964	.09954	.08538
1583.3	.00556	.08513	.09531	.09574	.07044
1679.2	.02543	.10437	.11505	.11532	.09004
1775.2	.04939	.19067	.20913	.20938	.16464
1871.1	.06349	.18688	.20103	.20105	.16311
1967.1	-.04203	.14699	.19604	.19976	.12519
2063.0	-.11604	.00765	.00341	.00290	-.02552

RUN NUMBERS 11 AND 12

A1 CALCULATION

ENERGY	CASE I	CASE II	CASE III	CASE IV	AVERAGES
1174.8	.60362	.60322	.63352	.57239	.60319
1273.3	.60403	-.00000	.66194	.54351	.45237
1371.9	.63514	.63447	.66868	.59999	.63457
1470.4	.63254	.63219	.69402	.56811	.63171
1569.0	.64930	.64916	.68899	.60767	.64878
1667.5	.68606	.68524	.70189	.66942	.68565
1766.1	.72608	.72386	.78432	.66463	.72472
1864.6	.76834	.76495	.81478	.71937	.76686
1963.2	.71702	.71713	.78445	.64557	.71604
2061.7	.52795	.53615	.48261	.57993	.53166

A2 CALCULATION

ENERGY	CASE I	CASE II	CASE III	CASE IV	AVERAGES
1174.8	.01501	.07703	.07750	.07751	.06176
1273.3	-.00025	.12081	.12090	.12090	.09059
1371.9	.02689	.09681	.09722	.09722	.07954
1470.4	-.01340	.11523	.11584	.11586	.08338
1569.0	-.00663	.07757	.07692	.07689	.05619
1667.5	.04911	.08169	.08249	.08245	.07394
1766.1	.07962	.20240	.20262	.20261	.17181
1864.6	.13967	.23341	.23791	.23753	.21213
1963.2	-.03380	.09874	.10912	.10980	.07096
2061.7	-.44959	-.59716	-.54575	-.55562	-.53703

RUN NUMBERS 18 AND 18

A1 CALCULATION

ENERGY	CASE I	CASE II	CASE III	CASE IV	AVERAGES
1199.5	0.	0.	0.	.62080	.62080
1295.4	0.	0.	0.	.64610	.64610
1391.4	0.	0.	0.	.66930	.66930
1487.3	0.	0.	0.	.67590	.67590
1583.3	0.	0.	0.	.70620	.70620
1679.2	0.	0.	0.	.71690	.71690
1775.2	0.	0.	0.	.75470	.75470
1871.1	0.	0.	0.	.83830	.83830
1967.1	0.	0.	0.	.94200	.94200
2063.0	0.	0.	0.	1.33580	1.33580

A2 CALCULATION

ENERGY	CASE I	CASE II	CASE III	CASE IV	AVERAGES
1199.5	0.	0.	0.	.06650	.06650
1295.4	0.	0.	0.	.05770	.05770
1391.4	0.	0.	0.	.05050	.05050
1487.3	0.	0.	0.	.07840	.07840
1583.3	0.	0.	0.	.06000	.06000
1679.2	0.	0.	0.	.08580	.08580
1775.2	0.	0.	0.	.11270	.11270
1871.1	0.	0.	0.	.06850	.06850
1967.1	0.	0.	0.	.10240	.10240
2063.0	0.	0.	0.	.25490	.25490

RUN NUMBERS 19 AND 20

A1 CALCULATION

ENERGY	CASE I	CASE II	CASE III	CASE IV	AVERAGES
1199.5	.64335	.64338	.67655	.60860	.64297
1295.4	.65953	.65944	.68551	.63230	.65919
1391.4	.67028	.67008	.70641	.63233	.66977
1487.3	.68708	.68676	.72524	.64694	.68651
1583.3	.70965	.70904	.73834	.67940	.70911
1679.2	.72739	.72693	.75340	.69993	.72691
1775.2	.75215	.75130	.78983	.71231	.75140
1871.1	.80375	.80281	.78355	.82512	.80381
1967.1	.83185	.83057	.79771	.86793	.83201
2063.0	.91212	.91039	.62408	1.22003	.91666

A2 CALCULATION

ENERGY	CASE I	CASE II	CASE III	CASE IV	AVERAGES
1199.5	-.00924	.06009	.05795	.05784	.04166
1295.4	.00356	.05831	.05617	.05609	.04353
1391.4	.00176	.07693	.07510	.07503	.05720
1487.3	.00622	.08641	.08388	.08380	.06508
1583.3	.02896	.08824	.08742	.08741	.07301
1679.2	.02432	.07900	.07742	.07739	.06453
1775.2	.03314	.11278	.11018	.11015	.09156
1871.1	.08443	.04196	.04304	.04321	.05316
1967.1	.11055	.03682	.04050	.04100	.05722
2063.0	.33164	-.27332	-.25902	-.25787	-.11464

RUN NUMBERS 20 AND 21

A1 CALCULATION

ENERGY	CASE I	CASE II	CASE III	CASE IV	AVERAGES
1187.1	.63241	.63219	.65499	.60877	.63209
1284.4	.64887	.64893	.63829	.65997	.64901
1381.6	.66104	.66090	.67044	.65115	.66088
1478.9	.67882	.67834	.70659	.64960	.67834
1576.1	.70020	.69937	.71845	.68096	.69975
1673.4	.71528	.71474	.71622	.71428	.71513
1770.6	.73949	.73820	.77019	.70700	.73872
1867.9	.78849	.78711	.75360	.82536	.78864
1965.1	.82531	.82457	.74658	.90903	.82637
2062.4	.91959	.91822	.63220	1.22712	.92428

A2 CALCULATION

ENERGY	CASE I	CASE II	CASE III	CASE IV	AVERAGES
1187.1	.01189	.05902	.05756	.05752	.04650
1284.4	.02412	.00273	.00270	.00270	.00806
1381.6	.01960	.03862	.03869	.03869	.03390
1478.9	.02219	.08030	.07868	.07866	.06496
1576.1	.04721	.08483	.08438	.08439	.07520
1673.4	.04772	.04967	.04964	.04966	.04917
1770.6	.05762	.12298	.12034	.12041	.10534
1867.9	.11388	.04063	.04249	.04275	.05993
1965.1	.12314	-.03987	-.03834	-.03821	.00168
2062.4	.31734	-.28335	-.27231	-.27144	-.12744

RUN NUMBERS 22 AND 25

A1 CALCULATION

ENERGY	CASE I	CASE II	CASE III	CASE IV	AVERAGES
2185.1	.86376	.86085	.70879	1.02322	.86416
2190.4	.90181	.89839	.72678	1.08228	.90231
2195.6	.91929	.91573	.74712	1.09670	.91971
2200.9	.94780	.94410	.75148	1.15041	.94845
2206.1	1.00700	1.00247	.77570	1.24597	1.00779
2211.4	1.03244	1.02777	.79152	1.28194	1.03342
2216.6	1.08334	1.07761	.85381	1.32255	1.08433
2221.9	1.12387	1.11779	.81796	1.44164	1.12531
2227.1	1.09172	1.08648	.81632	1.37664	1.09279
2232.4	1.07886	1.07303	.88719	1.27852	1.07940

A2 CALCULATION

ENERGY	CASE I	CASE II	CASE III	CASE IV	AVERAGES
2185.1	.43202	.10216	.09182	.09111	.17928
2190.4	.48252	.11380	.09953	.09850	.19859
2195.6	.48859	.11901	.11158	.11103	.20755
2200.9	.51063	.09232	.08023	.07936	.19063
2206.1	.59471	.09491	.08668	.08607	.21559
2211.4	.60273	.09128	.07262	.07119	.20945
2216.6	.65065	.18365	.14489	.14115	.28009
2221.9	.73593	.08497	.06138	.05947	.23544
2227.1	.66773	.05820	.06011	.06025	.21157
2232.4	.63113	.23562	.20795	.20498	.31992

RUN NUMBERS 23 AND 24

A1 CALCULATION

ENERGY	CASE I	CASE II	CASE III	CASE IV	AVERAGES
2185.1	.67897	.67844	.77360	.58234	.67834
2190.4	.69790	.69706	.80779	.58560	.69709
2195.6	.72378	.72296	.80610	.63959	.72311
2200.9	.75259	.75161	.83134	.67197	.75188
2206.1	.77456	.77349	.86361	.68333	.77375
2211.4	.80423	.80310	.87313	.73358	.80351
2216.6	.84948	.84806	.88709	.81095	.84890
2221.9	.90239	.89977	.93747	.86624	.90147
2227.1	.95157	.94761	.97303	.92987	.95052
2232.4	1.13977	1.13385	.79296	1.50121	1.14195

A2 CALCULATION

ENERGY	CASE I	CASE II	CASE III	CASE IV	AVERAGES
2185.1	-.00770	.19825	.20009	.20011	.14769
2190.4	.01312	.25142	.25362	.25363	.19295
2195.6	.03396	.20977	.21425	.21427	.16806
2200.9	.05103	.22160	.22372	.22372	.18002
2206.1	.04897	.23958	.24462	.24462	.19445
2211.4	.06863	.21925	.22027	.22026	.18210
2216.6	.12159	.20051	.20446	.20427	.18271
2221.9	.22443	.30292	.30180	.30192	.28277
2227.1	.34415	.38859	.39151	.39063	.37872
2232.4	.74432	.03276	-.02147	-.02579	.18245

Appendix I. D.: Tabulation of Anisotropy Data (Gamma Analysis Method II)

In this tabulation the beta particle anisotropies are identical to those listed in Appendix I.B., but the gamma ray data have been re-analyzed as desribed in the text. Axial and equatorial anisotropies are listed for each of ten intervals across the photopeak in the gamma ray spectrum. The quoted errors are statistical, including statistical errors in the background correction. The interval labeled 1 is at the high-energy side of the peak. The Haag Effect can be clearly seen: the anisotropy decreases from the leading edge of the peak (intervals 3--5) out through the low energy tail, and even reverses in some cases. The first two intervals (1 and 2) have very bad statistics and the background correction is a large fraction of the total counts for these intervals (in fact it exceeds the total in one or two cases, giving negative anisotropies) so these anisotropies are practically meaningless and no significance should be attached to their wide and random variations.

In order to obtain final values for each run, the anisotropies from intervals near the center of the peak (usually areas 4--7) were averaged. No large systematic differences are apparent between the anisotropies thus obtained and those from Method I using width A3 (Appendix I.B.). Thus it may be concluded that integration over width A3 successfully avoids the Haag Effect.

RUN NUMBER 5 HO = 1600 OE.

BETA ANISOTROPIES

ENERGY	W(AX.)	ERR.	W(EQ.)	ERR.
566.775	.46040	.00106	.99740	.00208
619.325	.43160	.00111	1.00250	.00233
671.875	.40300	.00119	.99910	.00264
724.425	.36830	.00127	.99450	.00307
776.975	.32980	.00140	1.00080	.00375
829.525	.28970	.00157	.99950	.00480
882.075	.25050	.00186	1.00060	.00643
934.625	.20840	.00229	.99150	.00936
987.175	.20630	.00356	.99190	.01555
1039.725	.22080	.00737	.87900	.03033

GAMMA ANISOTROPIES

AREA	W(AX.)	ERR.	W(EQ.)	ERR.
1	.97014	.16219	.02487	-.77356
2	.81748	.02231	1.06243	.13817
3	.82012	.00688	1.12549	.02006
4	.80886	.00356	1.07160	.00957
5	.80401	.00275	1.06519	.00670
6	.80386	.00290	1.06529	.00714
7	.80588	.00445	1.03644	.00993
8	.83973	.00757	1.02194	.01516
9	.91720	.01250	1.05782	.02465
10	.99853	.01724	1.49235	.09509

RUN NUMBER 13 HO = -1000 OE.

BETA ANISOTROPIES

ENERGY	W(AX.)	ERR.	W(EQ.)	ERR.
566.775	1.53400	.00059	.94940	.00102
619.325	1.56500	.00065	.94850	.00112
671.875	1.60100	.00074	.94320	.00124
724.425	1.63800	.00085	.94140	.00143
776.975	1.68500	.00101	.93590	.00169
829.525	1.74300	.00126	.93700	.00210
882.075	1.82400	.00164	.93830	.00275
934.625	1.91500	.00227	.93940	.00385
987.175	2.05600	.00339	1.01800	.00651
1039.725	2.31200	.00539	1.14700	.01143

GAMMA ANISOTROPIES

AREA	W(AX.)	ERR.	W(EQ.)	ERR.
1	.91263	.03856	1.15909	.10664
2	.80445	.00656	1.18781	.01638
3	.78212	.00203	1.14562	.00453
4	.78030	.00115	1.11519	.00212
5	.78495	.00088	1.06740	.00148
6	.79617	.00092	1.02189	.00143
7	.81621	.00122	.98167	.00177
8	.84477	.00178	.95237	.00222
9	.89230	.00235	.93335	.00280
10	.95705	.00297	.91988	.00363

RUN NUMBER 14 HO = 1000 OE.

BETA ANISOTROPIES

ENERGY	W(AX.)	ERR.	W(EQ.)	ERR.
566.775	.44290	.00028	1.03900	.00070
619.325	.41830	.00030	1.04200	.00078
671.875	.39230	.00032	1.04000	.00088
724.425	.36530	.00035	1.03600	.00102
776.975	.33290	.00039	1.04100	.00124
829.525	.29730	.00045	1.04000	.00155
882.075	.26370	.00054	1.05000	.00208
934.625	.24050	.00069	1.04900	.00294
987.175	.24000	.00100	1.06700	.00461
1039.725	.24890	.00160	1.09600	.00752

GAMMA ANISOTROPIES

AREA	W(AX.)	ERR.	W(EQ.)	ERR.
1	1.07018	.06836	1.17496	.14230
2	.88444	.00842	1.14283	.01581
3	.85426	.00244	1.09803	.00421
4	.84386	.00133	1.09909	.00207
5	.83423	.00097	1.09184	.00155
6	.82921	.00098	1.07666	.00159
7	.83071	.00126	1.04814	.00199
8	.85909	.00186	1.02729	.00251
9	.91307	.00253	1.00803	.00315
10	.97625	.00323	1.00448	.00409

RUN NUMBER 15 HO = 1500 OE.

BETA ANISOTROPIES

ENERGY	W(AX.)	ERR.	W(EQ.)	ERR.
566.775	.43810	.00070	1.04100	.00167
619.325	.41110	.00074	1.04400	.00186
671.875	.37980	.00079	1.04600	.00211
724.425	.34860	.00086	1.04600	.00245
776.975	.31580	.00093	1.04400	.00294
829.525	.27860	.00109	1.04600	.00371
882.075	.23960	.00128	1.05100	.00495
934.625	.21370	.00164	1.04700	.00705
987.175	.20860	.00240	1.05000	.01130
1039.725	.20970	.00383	1.05500	.01891

GAMMA ANISOTROPIES

AREA	W(AX.)	ERR.	W(EQ.)	ERR.
1	.84103	.12273	1.10892	.47032
2	.79020	.01758	1.25725	.04427
3	.80130	.00535	1.18550	.01149
4	.80781	.00306	1.14252	.00531
5	.82509	.00238	1.10565	.00379
6	.84360	.00249	1.06972	.00374
7	.86902	.00331	1.03956	.00472
8	.89695	.00482	1.01742	.00596
9	.93273	.00638	.99430	.00747
10	.98687	.00801	.97066	.00960

RUN NUMBER 16 HO = 1500 OE.

BETA ANISOTROPIES

ENERGY	W(AX.)	ERR.	W(EQ.)	ERR.
566.775	.43350	.00033	1.03500	.00081
619.325	.40540	.00035	1.03600	.00090
671.875	.37730	.00038	1.03500	.00102
724.425	.34560	.00041	1.03800	.00120
776.975	.31120	.00045	1.03300	.00143
829.525	.27360	.00051	1.03400	.00180
882.075	.23460	.00060	1.04000	.00241
934.625	.21040	.00077	1.04800	.00348
987.175	.20720	.00115	1.05700	.00566
1039.725	.21140	.00191	1.09600	.01011

GAMMA ANISOTROPIES

AREA	W(AX.)	ERR.	W(EQ.)	ERR.
1	.88175	.06706	1.66100	.38799
2	.85301	.00951	1.20992	.02287
3	.83242	.00272	1.14725	.00552
4	.81448	.00149	1.10376	.00251
5	.79130	.00110	1.06715	.00178
6	.78328	.00112	1.04048	.00178
7	.78882	.00146	1.02854	.00228
8	.83443	.00217	1.01029	.00291
9	.89748	.00293	.99938	.00370
10	.97522	.00380	.98900	.00482

RUN NUMBER 17 HO = -1500 OE.

BETA ANISOTROPIES

ENERGY	W(AX.)	ERR.	W(EQ.)	ERR.
566.775	1.53600	.00067	.96880	.00150
619.325	1.56300	.00073	.95680	.00160
671.875	1.59400	.00082	.95040	.00176
724.425	1.62400	.00095	.94680	.00199
776.975	1.66600	.00113	.93920	.00232
829.525	1.71400	.00141	.92710	.00283
882.075	1.76200	.00184	.93700	.00377
934.625	1.81700	.00258	.92750	.00535
987.175	1.90500	.00407	.96000	.00938
1039.725	2.20500	.00791	1.08600	.02327

GAMMA ANISOTROPIES

AREA	W(AX.)	ERR.	W(EQ.)	ERR.
1	.84744	.05034	2.16966	.67285
2	.87010	.00843	1.13804	.02117
3	.84506	.00253	1.06321	.00495
4	.81027	.00135	1.04466	.00225
5	.77761	.00094	1.02145	.00156
6	.75885	.00092	1.00739	.00153
7	.76382	.00122	1.00333	.00197
8	.81593	.00188	.99655	.00257
9	.89233	.00259	.98027	.00328
10	.96245	.00334	.98144	.00441

RUN NUMBER 7 HO = 2000 OE.

BETA ANISOTROPIES

ENERGY	W(AX.)	ERR.	W(EQ.)	ERR.
1199.475	.33370	.00060	1.01300	.00146
1295.425	.31330	.00063	1.01200	.00161
1391.375	.29590	.00068	1.01500	.00183
1487.325	.27760	.00075	1.00600	.00208
1583.275	.25980	.00084	1.01200	.00248
1679.225	.24170	.00099	1.01800	.00309
1775.175	.21570	.00122	1.01700	.00402
1871.125	.18840	.00158	1.01800	.00565
1967.075	.17130	.00243	1.05000	.00920
2063.025	.20040	.00513	1.10300	.01791

GAMMA ANISOTROPIES

AREA	W(AX.)	ERR.	W(EQ.)	ERR.
1	.13011	-.65569	2.60836	.97663
2	1.01454	.04995	1.15288	.04584
3	.92569	.00668	.98716	.00901
4	.86817	.00231	.96337	.00373
5	.84517	.00147	.97178	.00260
6	.84088	.00148	.99378	.00271
7	.84050	.00218	1.01393	.00383
8	.84913	.00403	1.02397	.00548
9	.89726	.00665	1.02823	.00746
10	.97369	.00982	1.09109	.01191

RUN NUMBER 8 HO = -2000 OE.

BETA ANISOTROPIES

ENERGY	W(AX.)	ERR.	W(EQ.)	ERR.
1199.475	1.63700	.00165	.93830	.00284
1295.425	1.66300	.00183	.93850	.00301
1391.375	1.69600	.00210	.92780	.00328
1487.325	1.71400	.00241	.93620	.00367
1583.275	1.73900	.00290	.92850	.00427
1679.225	1.75300	.00357	.91510	.00500
1775.175	1.83200	.00498	.91390	.00662
1871.125	1.84800	.00726	.91290	.00926
1967.075	1.96900	.01301	.90780	.01473
2063.025	2.15200	.02924	.93450	.02999

GAMMA ANISOTROPIES

AREA	W(AX.)	ERR.	W(EQ.)	ERR.
1	2.50853	4.81888	.71265	.60464
2	1.18196	.04825	.89759	.04293
3	.96376	.00716	.96445	.01012
4	.94531	.00285	.99316	.00450
5	.90183	.00184	1.00518	.00322
6	.87294	.00179	1.00672	.00333
7	.84449	.00243	.99228	.00460
8	.82655	.00409	.95365	.00621
9	.85621	.00674	.94651	.00853
10	1.01197	.01146	.91580	.01274

RUN NUMBER 9 HO = -1500 OE.

BETA ANISOTROPIES

ENERGY	W(AX.)	ERR.	W(EQ.)	ERR.
1199.475	1.62400	.00276	.93940	.00433
1295.425	1.65300	.00307	.93160	.00479
1391.375	1.66800	.00345	.91700	.00528
1487.325	1.71700	.00405	.92720	.00609
1583.275	1.69300	.00466	.91660	.00735
1679.225	1.72800	.00581	.90550	.00901
1775.175	1.77600	.00775	.87550	.01203
1871.125	1.81200	.01120	.88140	.01658
1967.075	1.73600	.01762	.83880	.02528
2063.025	1.69000	.03648	1.01700	.05616

GAMMA ANISOTROPIES

AREA	W(AX.)	ERR.	W(EQ.)	ERR.
1	-1.76330	.48785	-.13131	.18405
2	.95890	.07331	.59849	.06033
3	.94553	.01202	.88879	.01858
4	.92089	.00470	.98931	.00848
5	.89533	.00321	1.01096	.00594
6	.88305	.00332	1.00932	.00615
7	.85774	.00470	.97823	.00836
8	.82252	.00763	.91879	.01146
9	.85886	.01362	.94147	.01904
10	1.17726	.03987	1.02407	.05971

RUN NUMBER 10 HO = 1500 OE.

BETA ANISOTROPIES

ENERGY	W(AX.)	ERR.	W(EQ.)	ERR.
1174.775	.36080	.00173	1.00800	.00411
1273.325	.34210	.00183	1.01100	.00456
1371.875	.31500	.00193	1.03100	.00523
1470.425	.29550	.00209	1.00900	.00586
1568.975	.27810	.00233	1.02600	.00702
1667.525	.26040	.00271	1.02400	.00848
1766.075	.23250	.00316	.99570	.01051
1864.625	.20730	.00394	.99220	.01434
1963.175	.18020	.00551	1.06100	.02332
2061.725	.15310	.00848	.97780	.03619

GAMMA ANISOTROPIES

AREA	W(AX.)	ERR.	W(EQ.)	ERR.
1	.48758	.34299	*2.08794	*64.006
2	.67940	.05314	2.19994	.76237
3	.66973	.01306	1.10027	.04824
4	.74614	.00659	1.05410	.01823
5	.82660	.00530	1.01925	.01233
6	.90394	.00600	1.04376	.01343
7	.89246	.00813	1.08667	.01981
8	.84531	.01129	1.45874	.04652
9	1.01402	.02341	-1.43924	-.04789
10	2.31192	.16958	.29812	-.02018

RUN NUMBER 11 HO = 1000 OE.

BETA ANISOTROPIES

ENERGY	W(AX.)	ERR.	W(EQ.)	ERR.
1174.775	.35970	.00172	.97770	.00416
1273.325	.34550	.00183	.96030	.00452
1371.875	.32140	.00187	.97010	.00515
1470.425	.30050	.00207	.96330	.00586
1568.975	.28370	.00231	.97020	.00699
1667.525	.27090	.00269	.98350	.00866
1766.075	.24120	.00308	.93230	.01043
1864.625	.22480	.00398	.94420	.01468
1963.175	.18970	.00528	1.00400	.02383
2061.725	.18180	.00854	1.02800	.04328

GAMMA ANISOTROPIES

AREA	W(AX.)	ERR.	W(EQ.)	ERR.
1	.07486	.10362	1.11996	1.93930
2	.66031	.05557	-6.31427	2.68571
3	.85254	.01893	1.06585	.06017
4	.87706	.00876	.96806	.01842
5	.89068	.00637	.98927	.01243
6	.88676	.00652	1.18056	.01632
7	.84694	.00908	1.28253	.02710
8	.88237	.01651	1.62633	.06897
9	.82021	.02758	-1.18175	-.06433
10	.85798	.07841	.40711	-.02351

RUN NUMBER 12 HO = -1000 OE.

BETA ANISOTROPIES

ENERGY	W(AX.)	ERR.	W(EQ.)	ERR.
1199.475	1.62800	.00631	.97150	.00800
1295.425	1.62600	.00687	.95970	.00875
1391.375	1.67500	.00792	.96500	.00989
1487.325	1.65400	.00883	.95910	.01127
1583.275	1.67600	.01054	.97740	.01361
1679.225	1.74300	.01342	.96120	.01643
1775.175	1.80000	.01795	.93050	.02091
1871.125	1.87400	.02640	.89730	.02842
1967.075	1.73400	.03978	.92880	.04595
2063.025	1.32700	.06220	1.37600	.12663

GAMMA ANISOTROPIES

AREA	W(AX.)	ERR.	W(EQ.)	ERR.
1	.36040	.45002	.69305	.79572
2	.55275	.21415	1.04910	.26092
3	.70429	.04453	1.36941	.10550
4	.82953	.01838	1.12495	.04769
5	.90997	.01306	1.03440	.03201
6	.95855	.01451	1.00314	.03345
7	.97837	.02335	1.07798	.05695
8	1.07231	.05977	1.74764	.19691
9	.13826	-.05611	.17868	-.20163
10	.53360	-.02106	.56013	-.03821

RUN NUMBER 18 HO = -1500 OE.

BETA ANISOTROPIES

ENERGY	W(AX.)	ERR.	W(EQ.)	ERR.
1199.475	1.68200	.00279	.99130	.00412
1295.425	1.70900	.00307	.99840	.00456
1391.375	1.73300	.00346	.99440	.00508
1487.325	1.75700	.00397	.98860	.00581
1583.275	1.78000	.00472	.98650	.00687
1679.225	1.80600	.00586	.98550	.00851
1775.175	1.86000	.00786	.97910	.01110
1871.125	1.92300	.01157	.99270	.01631
1967.075	2.04700	.01980	1.00100	.02779
2063.025	2.52100	.04323	.93630	.05595

GAMMA ANISOTROPIES

AREA	W(AX.)	ERR.	W(EQ.)	ERR.
1	.76031	.21270	1.42828	.38208
2	.86496	.02631	1.04874	.04487
3	.88346	.00871	1.01866	.01336
4	.89183	.00462	1.02534	.00757
5	.89584	.00354	1.02488	.00575
6	.89723	.00373	1.03279	.00598
7	.90736	.00558	1.03360	.00777
8	.91650	.00899	1.02528	.01065
9	.93648	.01293	1.00307	.01338
10	.95961	.01631	1.01292	.01793

RUN NUMBER 19 HO = 1500 OE.

BETA ANISOTROPIES

ENERGY	W(AX.)	ERR.	W(EQ.)	ERR.
1199.475	.29260	.00056	.96660	.00165
1295.425	.27520	.00059	.96290	.00183
1391.375	.25770	.00064	.96300	.00208
1487.325	.23850	.00069	.95590	.00240
1583.275	.22370	.00079	.96360	.00289
1679.225	.19940	.00091	.95870	.00360
1775.175	.17500	.00112	.94480	.00470
1871.125	.14360	.00147	.97060	.00711
1967.075	.12540	.00236	.95600	.01196
2063.025	.15730	.00612	1.07720	.02847

GAMMA ANISOTROPIES

AREA	W(AX.)	ERR.	W(EQ.)	ERR.
1	1.02496	.37280	1.83565	.38319
2	1.01627	.02539	1.14436	.03170
3	.93126	.00634	1.00208	.00826
4	.88323	.00296	.98963	.00456
5	.88119	.00218	.99836	.00343
6	.89182	.00227	1.02787	.00360
7	.91382	.00345	1.04862	.00474
8	.91126	.00559	1.06450	.00675
9	.93594	.00827	1.07975	.00879
10	.98865	.01153	1.16913	.01336

RUN NUMBER 20 HO = -1000 OE.

BETA ANISOTROPIES

ENERGY	W(AX.)	ERR.	W(EQ.)	ERR.
1199.475	1.66500	.00194	.99390	.00256
1295.425	1.69400	.00214	.99860	.00284
1391.375	1.70800	.00240	.98560	.00315
1487.325	1.73000	.00276	.98610	.00363
1583.275	1.76700	.00331	.97700	.00428
1679.225	1.78400	.00410	.98800	.00537
1775.175	1.81500	.00545	.97900	.00708
1871.125	1.89600	.00826	1.00100	.01055
1967.075	1.93900	.01436	1.01900	.01865
2063.025	2.13800	.03613	1.10800	.04822

GAMMA ANISOTROPIES

AREA	W(AX.)	ERR.	W(EQ.)	ERR.
1	.78393	.24570	1.21790	.32355
2	.92667	.02418	1.29603	.05487
3	.88854	.00686	1.19236	.01388
4	.90000	.00359	1.09428	.00674
5	.88620	.00273	1.03189	.00457
6	.88891	.00291	.98969	.00444
7	.86818	.00415	.96556	.00555
8	.85039	.00622	.96757	.00771
9	.85868	.00898	.97723	.01026
10	.98186	.01417	1.04330	.01631

RUN NUMBER 21 HO = 1000 OE.

BETA ANISOTROPIES

ENERGY	W(AX.)	ERR.	W(EQ.)	ERR.
1174.775	.31650	.00120	.96730	.00348
1273.325	.29870	.00126	.99960	.00401
1371.875	.27820	.00132	.98860	.00445
1470.425	.25690	.00141	.96000	.00497
1568.975	.24480	.00160	.96590	.00589
1667.525	.22650	.00183	.97850	.00731
1766.075	.20340	.00216	.93790	.00904
1864.625	.17790	.00272	.97150	.01300
1963.175	.14010	.00362	1.00800	.02184
2061.725	.14050	.00711	1.08400	.04844

GAMMA ANISOTROPIES

AREA	W(AX.)	ERR.	W(EQ.)	ERR.
1	2.13940	.88093	1.95980	1.33616
2	1.05460	.05739	1.23405	.10714
3	.88506	.01457	1.15800	.02792
4	.84162	.00782	1.02120	.01308
5	.81468	.00563	.95997	.00900
6	.82277	.00580	.93412	.00967
7	.84475	.00799	.94524	.01212
8	.79659	.01136	1.00263	.01826
9	.84554	.01757	1.10801	.02994
10	1.05400	.03798	2.14160	.14357

RUN NUMBER 22 HO = 1500 OE.

BETA ANISOTROPIES

ENERGY	W(AX.)	ERR.	W(EQ.)	ERR.
1235.125	.28930	.00134	.98570	.00375
1340.375	.26940	.00141	.98700	.00423
1445.625	.24930	.00151	.97370	.00481
1550.875	.22630	.00165	.98890	.00576
1656.125	.20090	.00182	.98030	.00698
1761.375	.17510	.00208	.99660	.00905
1866.625	.14180	.00240	1.00100	.01232
1971.875	.13900	.00335	1.00100	.01872
2077.125	.13980	.00555	.97770	.03375
2182.375	.13530	.01151	.97430	.07471

GAMMA ANISOTROPIES

AREA	W(AX.)	ERR.	W(EQ.)	ERR.
1	.44656	.11645	1.10889	.13967
2	.67140	.04609	.98996	.02768
3	.83216	.00980	1.02064	.00937
4	.83822	.00392	1.05245	.00454
5	.83891	.00250	1.07221	.00362
6	.83995	.00248	1.07853	.00368
7	.87159	.00307	1.07439	.00431
8	.89856	.00383	1.05003	.00483
9	.87644	.00455	1.04101	.00551
10	.86445	.00503	1.04134	.00585

RUN NUMBER 25 HC = -1500 OE.

BETA ANISOTROPIES

ENERGY	W(AX.)	ERR.	W(EQ.)	ERR.
1235.125	2.10600	.00891	.94730	.00953
1340.375	2.17700	.01016	.93730	.01049
1445.625	2.20400	.01151	.94670	.01200
1550.875	2.24800	.01349	.94910	.01418
1656.125	2.35300	.01672	.95580	.01712
1761.375	2.38500	.02079	.94180	.02159
1866.625	2.46200	.02790	.87480	.02706
1971.875	2.54600	.04136	.94150	.04460
2077.125	2.48000	.06769	.98290	.08613
2182.375	2.44900	.15662	.86600	.18542

GAMMA ANISOTROPIES

AREA	W(AX.)	ERR.	W(EQ.)	ERR.
1	.46040	.06584	1.06000	.11188
2	.59210	.03195	1.13400	.04245
3	.74450	.01142	1.12300	.01742
4	.77720	.00549	1.10000	.00701
5	.76730	.00358	1.06900	.00579
6	.76020	.00333	1.04900	.00524
7	.78140	.00379	1.02800	.00553
8	.76070	.00442	1.00500	.00603
9	.72200	.00498	1.00600	.00669
10	.71100	.00516	1.00400	.00672

APPENDIX II

Dirac Matrices

The Dirac matrices are four-by-four matrices which are the operators in the Dirac hamiltonian:

$\underset{\sim}{\alpha}$ = velocity operator (Cartesian 3-vector) β = fourth component of velocity four-vector

$\alpha_j^2 = \beta^2 = 1$ $\underset{\sim}{\sigma}$ = spin operator $= \underset{\sim}{\alpha} \times \underset{\sim}{\alpha}/2i$

An alternative representation of the Dirac matrices is the set of γ matrices:

$$\gamma_\alpha(-i\beta\underset{\sim}{\alpha}, \beta) = (\underset{\sim}{\gamma}, \gamma_4) \quad \text{i.e. } \gamma_4 = \beta \text{ and } \underset{\sim}{\gamma} = -i\beta\underset{\sim}{\alpha}$$

Thus $\underset{\sim}{\gamma} = -i\beta\underset{\sim}{\alpha} \rightarrow \gamma_4\underset{\sim}{\gamma} = -i\underset{\sim}{\alpha}$. (This is the opposite sign convention for $\underset{\sim}{\alpha}$ from the one originally used by Dirac.)

Define $\gamma_5 = \gamma_1\gamma_2\gamma_3\gamma_4$. The γ's obey the commutation relations:

$$\gamma_i\gamma_j = -\gamma_j\gamma_i \qquad i,j = 1,5$$

Using the above definitions, we have:

$$\underset{\sim}{\sigma} = -i/2[i\gamma_4\underset{\sim}{\gamma} \times i\gamma_4\underset{\sim}{\gamma}]$$

$$= -i/2[\underset{\sim}{\gamma} \times \underset{\sim}{\gamma}]$$

$$= -i[\gamma_2\gamma_3\hat{i} + \gamma_3\gamma_1\hat{j} + \gamma_1\gamma_2\hat{k}]$$

or $\underset{\sim}{\sigma} = -i\gamma_4\underset{\sim}{\gamma}\gamma_5 = -\underset{\sim}{\alpha}\gamma_5$ or $\gamma_5 = -\alpha_i\sigma_i$

Also, $\gamma_4\gamma_\alpha = (-i\underset{\sim}{\alpha}, 1)$

$$\gamma_4\gamma_\alpha\gamma_5 = (i\underset{\sim}{\sigma}, \gamma_5)$$

and $\gamma_\alpha\left(\frac{1+\gamma_5}{2}\right) + \gamma_\alpha\gamma_5\left(\frac{1+\gamma_5}{2}\right) = \gamma_\alpha/2 + \gamma_\alpha\gamma_5/2 + \gamma_\alpha\gamma_5/2 + \gamma_\alpha/2 = \gamma_\alpha[1+\gamma_5]$

This last relationship was used to simplify the expressions in Eq. 4, Chap. II.

APPENDIX III

Notes on Apparatus Construction

In the course of the time during which the foregoing work was carried out, the demagnetization cryostats in use in this laboratory evolved from the small, simple chrome-alum apparatus described in Chap. III to the large and rather complex CMN cryostat described in Chap. VI. During this development several false starts were made and variations of the apparatus designs were tried. Since the process of development will doubtless continue in the coming years, it seems only reasonable to pass on as much as possible of the rationale behind the current apparatus design as a starting point for those who will carry on the work. Accordingly in this appendix I have compiled some notes based on the experience of myself and my contemporaries in attempting to improve or adapt cryostat designs. Of course, much of this information is available in the published literature; the following has to recommend it only the fact that it is based upon experience in this laboratory with materials and apparatus available here and thus is particularly applicable as a basis for continued work at LRL. The notes are for the most part of a general nature and should serve as a complement to the more specific apparatus descriptions in Chap. VI and in the PhD thesis of J. A. Barclay.

It often seems to be the case that information of this sort is passed on within a laboratory by word of mouth and becomes a kind of folklore, which, like other sorts of folklore, suffers not only from inaccuracies and incompleteness, but also from a gradual distortion with repetition and the passage of time. While I make no claims for the accuracy, and certainly not for the completeness, of the following notes, I can at least be certain that being in semipermanent form they will not alter in content with each new generation of students.

III.1 Salt Pill and Sample Assembly

Slurries

The usual recipe for chrome alum(CA) slurry is one part glycerin to one part saturated CA solution mixed with powdered CA to the desired con-

sistency. The same recipe works for CMN with the omission of the saturated solution. Attempts to use Octoil-S as the suspension medium were generally unsuccessful. Ethanol works but not as well as glycerin. Finer powdering of the salt seems to improve cooling down to about 50 mesh; further grinding seems to do no more good. It seems likely that very fine powdering hastens deterioration of the slurry. Powdering of the CMN is greatly facilitated by drying the powder on a piece of filter paper for about 20 min. before each stage of seiving after grinding in the ball mill; this prevents clumping of wet particles. Drying is unnecessary with CA.

Definite deterioration of the slurries occurs with time. The chief contributing factors seem to be allowing the slurry to stand for long times (more than 12 hrs.) at room temperature and pumping on an imperfectly cooled slurry. The slurry temperature must be below -90° C. to prevent sublimation of water and this may require more than two hrs. of cooling in LN in the case of pills of 200 cc. or more volume when they are mounted in the cryostat.

Slurry Containers

These have been made either of glass or of copper sheet bonded with a mylar or fibreglass joint. The chief problem is preventing leakage. The obvious solution is to "can" the slurry, e.g. in stainless steel cans with soldered tops; such a can would allow pumping even at room temperature and would facilitate leak testing, as well as preventing leakage. This was tried by J.A.Barclay but failed due to overfilling of the can and the use of Bi-Cd solder in the top seal, which broke under pressure from the slurry. Such a can should of course be equipped with a break seal to prevent an explosion in the event of leakage and condensation of liquified air or helium inside the can. Another problem is sealing the heat link where it emerges from the can.

The copper sheet containers have generally been fitted with fibreglass bottoms attached with screws and/or epoxy. After extended use the epoxy cracks, allowing leakage. (While fibreglass is easily machineable and does not seriously adsorb exchange gas, it probably has a fairly large heat capacity in the LN-LHe temperature range and thus slows cooling of the pill during LHe transfer, so it should ont be overused.) In general

the best rule for avoiding slurry leakage is not to overfill the containers; 80% full seems about right. Also, attempts to squeeze in more slurry by making dimensional tolerances tight are likely to result in much frustration with little gain in cooling capacity.

Support Systems

Ideally, a support system should be simple, easily assembled, vibration-free, strong, and have very low heat conductivity. The material that seems to fit these requirements best is pitch-bonded graphite. Union Carbide grade ATJ is a stock item at LRL and is easily machined. (Most published references seem to be to grade AGOT but the differences are apparently minor.) Pieces 1/4" in diameter and as short as 1/2" have been used as support legs successfully; no difficulty with adsorption of exchange gas seems to occur. Graphite is, however, brittle and breaks easily, especially under shear stress. Attachment of the legs has usually been by means of sockets made of stainless steel, nylon, or fibreglass. These should be at least 1/2" deep to insure lateral stability. Metal clamps have been used elsewhere and epoxy works well at first but eventually breaks. Our attempts to use threaded graphite rods or screws into the graphite were not encouraging.

A second type of support is the telescoped stainless steel tube. These are made from .005" thick sheet or tubing and may be slitted longitudinally to avoid eddy current heating during demagnetization although this is probably not necessary and reduces strength. The telescoped sections may be hard-soldered together at the ends but this is a weak point, since the joint usually corrodes in two in a year or so. These legs are less rigid than the graphite supports and therefore more subject to vibration. They are, however, less susceptible to breakage, especially when used in tension rather than compression.

Nylon or stainless steel filaments may be used for light supports. they are subject to vibrations, especially the nylon. Their principal application in large cryostats is in tying down long heat shields and heat links to maintain rigidity and position; in this case tying them tightly is clearly of great importance. Threads are definitely inferior

to rigid mountings for supporting salt pills of greater than 50 cc. volume and also require more time in assembly.

Heat Links

We have used two types of heat links: fins and wires. Wires are in theory superior since the surface-to-volume ratio may be made much greater than with fins; however, a practical difficulty arises in getting all the wires separated and in contact with the slurry. Attachment of the sample at the other end of the heat link is also more difficult with wires. The usual procedure for making a wire heat link is to make a mandrel of circumference equal to the final desired length of the link, mount it in a lathe or crank-frame, and wind the desired number of wires onto it. Bare copper of #40 or finer diameter is used. After winding, the wires are cut to make a bundle which is then stuffed into a thin-walled stainless or glass mold tube. If the bundle is made double-length with half the desired number of wires, it may be doubled over and pulled into the mold tube by means of a loop of heavier wire inserted at the bend in the middle. More wires can be packed into the mold in this way. Maximum filling factors seem to be about 70%. Epoxy (Shell Epon 826 or equivalent) can then be sucked into the mold by vacuum to pot that part of the heat link which will be outside the slurry container. The epoxy may be warmed gently to reduce its viscosity. After curing, the tube can be broken or peeled off. A "mold release" compound is available to permit sliding off of the mold tube if desired. Care must be taken to avoid tangling the free ends of the wires which make contact with the slurry.

Fins are usually made from .005" OFHC copper and annealed as late as possible before installation. The rigid section may be soldered into a bundle or folded to form a circular stalk. If solder is used, it should not be Pb-Sn or other superconducting solder and should be in a few spots rather than all along the length of the fins. Other things being equal, fins seem to give lower sample temperatures than wires. This is probably related to the formation of a warmed layer of slurry at the slurry-heat link boundary: fins are more uniform and make better use of the slurry volume even though wires may have more surface. This warmed layer seems

to be the limiting factor in transport of heat from the sample to the cooling salt; calculations indicate that the conductivity of the slurry-metal boundary is at least 10x worse than even a superconducting solder joint. Perhaps finer powdering of the salt would be of more use in the case of a wire heat link--the experiments with slurry powdering were done using fins.

Thermal Contact

The only really effective means of thermal contact below 10 mdeg. K. seems to be metallic contact, although J.C.Wheatley has used cells containing liquid He mixtures sucessfully. We have used pressure (copper fins 0.5 cm^2 in area pressed together with a stainless steel screw) with success down to about 15 mdeg. Greases and varnishes seem to be of little help at very low temperatures but In-Ga eutectic or pure Ga, both of which are liquids near room temperature, make good solders for usually-solderable materials. The former can even be used on aluminum. Electroplating of copper over a joint for thermal contact does not seem to be significantly better than soldering, although it is difficult to get an unstrained plate and this may reduce the conductivity of such a joint below what it might ideally be. Such plated joints are necessary when magnetic fields are to be avoided in the apparatus. Conductive epoxies give thermal contact similar to copper plate or solder down to 9 mdeg. For cooling metallic samples by this method, the limiting factor is the heat link-slurry contact, as mentioned above, so the temperatures obtained are fairly insensitive to the method of attachment of the sample to the heat link as long as large heat inputs to the sample are not present. For nonmetallic samples, probably liquid He cells or conductive epoxies are the only workable methods, and these have been given only a cursory exploration here. In the case of the He cell, a major problem is the heat capacity of the He itself, which may limit the final temperature in a one-shot cooling device.

Salt Pill Configuration

The question of whether the sample should be above or below the salt pill is fairly complex. If a simple solenoid is used to polarize the sample, the latter must be below the salt pill since there is no place to

put an axial gamma counter if the sample is above the pill. The pill-above mode makes it easier to mount the sample and rf coils or particle detectors in a fixed framework since they can all be attached to the same support cage with only a can covering the tip of the experimental chamber. Conversely, in the pill-below mode, coils and detectors are usually attached to the upper part of the apparatus by their leads, while the sample is necessarily attached to the lower part by the heat link, and this makes knowledge of the relative positions of sample and detectors or coils more difficult to obtain after assembly of the apparatus. If a flux trapping ring or Helmholtz pair is used to apply the polarizing field, either configuration may in principle be used since the quantization axis is then horizontal and an axial counter may be placed with no difficulty in either mode. In general, the pill-above mode seems superior except for one limitation: whenever the pill is warmed to room temperature (as it must be for mounting a sample from which particles are to be detected; otherwise ice will form on the cold sample during assembly of the apparatus and subsequently cause scattering of the particles), if any leakage of slurry occurs, the leakage will come down the heat link and onto the sample, which of course it will not do in the pill-below mode of mounting. Also, of course, it is more difficult to get detector leads, etc., past the pill in the pill-above mode but this can be accomplished by mounting the pill off-center in the experimental chamber to leave room at one side or by using separate lead tubes outside the pill container.

III.2 Experimental Chamber Construction

Seals

Gutter seals are compact and reliable. They have two main disadvantages: 1) they are not self-aligning and one can easily make the seal with a dog-leg, requiring resoldering; and 2) they require heating of a large section of the apparatus to melt the solder. The latter objection can be alleviated by using low melting solders such as Wood's alloy and by using heat sinks made of wet asbestos cloth tape above and below the seal. Varian Conflat flanges, by contrast, are self-aligning and require no heating, but they are bulky; also, bare copper gaskets are liable to

leak in superfluid helium and must be coated on both sides with In in a smooth layer. Acid paste-type flux works well for this job. There is some controversy over the thickness of In required to prevent leakage but a layer 0.5 mm or thicker will never leak unless the two flanges were not at the same temperature during assembly. The flanges do not require tightening until they are in contact as is the case with a bare copper gasket; a firm, even contact is sufficient. They are difficult to disassemble when cold.

Flanges using knife-edges and aluminum gaskets are usable at LN temperature but probably not at LHe temperature, especially in superfluid. Gaskets made of In may be used in O-ring type flanges and are reportedly superfluid-tight although not permanent. The type of gasket which uses a smooth, rounded pressure flange and aluminum foil gaskets is reported to be unreliable even at room temperature.

Copper-glass housekeeper seals are superfluid leak tight but eventually the copper work-hardens and the seal breaks. The Kovar-glass type are more permanent but they are magnetic.

Kovar-ceramic electrical feedthroughs are often tight to superfluid. The type with two solid leads and green ceramic is especially relaible. They are somewhat fragile and sensitive to thermal shock, however, particularly through the leads, and care must be taken in soldering them.

Mylar or fibreglass to metal joints can be operated sucessfully at low temperatures but the epoxy layer which cements the plastic to the metal must be as thin as possible; large contact areas are also desirable. Mylar is permeable to He gas at room temperature but not below LN temperature.

Epoxies

Adiprene L-100: the MOCA catalyst must be melted at 150° C. and mixed about 1:10 by weight with the resin which is preheated to 100° C. The pot life is about 10 minutes. The resin deteriorates on prolonged storage. Curing requires 4 hrs. or more at 75° C. or at least 24 hrs. at room temperature. The cured epoxy is rubbery and not too strong, but thick layers will not crack on immersion in LHe, unlike most hard epoxies. It may peel away from a metal surface to which it was bonded, especially if

the surface was not sanded before application of the epoxy. This epoxy is most useful for sealing applications.

Epon 826: This resin should be mixed about 1:1 by volume with the Versamid hardener. It may be warmed to about 100° C. to decrease viscosity with some reduction in pot life, which is at least 1/2 hr. at room temperature. Curing takes at least 2 hrs. at 75° C. This is a hard epoxy which is useful structurally in thin layers for applications such as joining plastics to metal. Layers more than about .005" thick will crack on being cooled to LHe temperature.

Fast setting epoxies, Minitgrip and Epoweld: These are generally not good for cryogenic structural applications since they crack on being cooled; they are useful for temporary setups and for potting coils, etc. Minitgrip actually takes some time to set and is best cured at elevated temperature (75° C.), while Epoweld really does set in 3--4 minutes and speed is necessary in applying it.

Conductive epoxies, Dynaloy and Tra-Con: These both cure best overnight at 60° C. or higher. Dynaloy will often be slightly tacky after removal from the curing oven until it cools. It is mixed 1:1 with the hardener; both components contain silver powder. Tra-Con is a stock item and contains silver in the resin only. Both give joints with less than a few ohms resistance although they are no-good for low-noise connections. Both will stand cryogenic temperatures although Tra-Con is more reliable.

Epibond and Stycast: These are used by J.C.Wheatley for sealing and structural purposes. Epibond 100A can be cast and machined and is apparently stable and leak-tight at LHe temperature. Epibond 121 and Stycast are used for sealing leads, etc. Apparently some experience is necessary to get good results.

Radiation Baffles

The baffle designed by G.A.Westenbarger which has several overlapping fins and fits in the central pumping tube is in general use in the current apparatus. It seems to work well: a sample directly exposed to a baffle of this type could be cooled to 5 mdeg. Such a baffle must be thermally anchored to be effective, however, and if a large heat load is placed on it, it may prove necessary to use a copper braid in contact with the LHe

to carry the heat away from the baffle. It is quite possible for parts inside a cryostat to be at 40° K. even when the chamber is surrounded by 1° LHe and care must be taken to anchor everything that is expected to remain cold in the absence of exchange gas. For small lead tubes, copper streamline tees make good radiation traps: the lead tube is soldered into one arm of the tee, the leads enter the main experimental chamber through the sidearm, and the remaining arm is plugged and the interior blackened with aquadag to absorb radiation. For greater efficiency, two tees may be soldered together to make an H-shaped trap with the leads entering in one arm of the H and leaving through the other. Needless to say, such traps should be directly in the LHe bath for good thermal anchoring, especially if the leads are anchored to a binding post on the inside. Attachment of several side tubes with such traps to the main experimental chamber, and sharing its vacuum, is quite feasible, but will increase the pumpout time for exchange gas.

Materials and Solders

A few random notes on cryostat construction:

Brass is often porous, especially large diameter rods which are strained during extrusion. Parts should be made from plate to avoid superfluid leaks.

Thinwall stainless tube is stronger than the engineering tables seem to indicate. We have found that a sleeve 4-1/2" in diameter and .020" thk. will support one atmosphere from outside if it is supported at 8" intervals. On the other hand, .010" tube of the same diameter buckles even if supported at 4" intervals.

One important materials consideration which is sometimes neglected is differential expansion. Cryostat parts are subjected to large temperature differences and mutual length changes over a 4 foot length from top to bottom may be rather large if materials are mismatched. Welded and hard soldered joints are liable to crack if subjected to this sort of strain over long periods.

Needless to say, parts emerging from liquid helium and going to room temperature must be made of low-conductivity materials and must be as thin

as possible. Frequent thermal anchoring is desirable. Pumping tubes may decrease in size at low temperatures without decreasing throughput. Styrofoam is a good gas trap and radiation shield but bores made through a layer of styrofoam should be lined with stainless steel or fibreglass tubing to prevent crumbling.

The soft solders which we have used include various lead-tin alloys, Wood's alloy, Bi-Cd eutectic, indium and indalloy solders, gallium, and indium-gallium eutectic. Lead-tin is a good general purpose solder and tins most common metals but it melts at fairly high temperatures, (M.P. of 50-50 is 220° C.) and its critical field is probably as large as 800 oe. Stainless steel parts should be pretinned using phosphoric acid flux and then washed carefully.

Wood's alloy has a much lower melting point (70° C.) but tinning must be carried out well above the melting point. Its critical field is probably lower than that of Pb-Sn solder. Wood's alloy is fairly brittle and not too strong but will work in most gutter seals. Both Wood's alloy and Pb-Sn make reliable leak tight joints if carefully done.

This is in contrast to Bi-Cd eutectic, which often contains superleaks, no matter how carefully the joint is made. This solder seems to be extremely sensitive to composition and it is probably best to purchase it if a supplier can be found. It tends to corrode on standing and pockets of corrosion are trapped in the metal when it is melted. Sometimes rapid cooling of the joint with water improves the chances for a leak-tight result. Tinning with Bi-Cd is difficult, especially on stainless steel. Bi-Cd gutter seal joints will often crack under thermal shock, e.g. when liquid helium is transferred onto them. The principal advantage of this solder is its low critical field (ca. 35 oe.) which makes it useful where magnetic fields are to be avoided; this seldom seems to outweigh its drawbacks, especially for making vacuum seals. Its melting point is about 150° C.

Indium solder is useful for making superconducting leads and for coating copper gaskets as mentioned above. It is poisonous and care sould be taken not to breathe the yellow fumes of $InCl_2$ which vaporize

from the work when acid fluxes are used. A more generally useful set of solders is contained in the Indalloy solder kit available from the Indium Corp. of America. The kit contains solders and fluxes for special applications such as soldering aluminum (which it does quite well, at least for electrical leads). It has some low melting (35° C.) solders which may be used on Kovar seals to avoid breakage. The use of Ga and In-Ga for attaching samples has already been mentioned. These solders are especially useful for thin or heat-sensitive foils. The critical field of Ga is about 50 oe.

Magnetic Shields

Superconducting magnets can seldom be reduced to zero field, because of flux trapping in the wire. We have found 1/16" thick mu-metal around ths salt pill container to be effective in reducing the trapped field to a tolerable level. A large mu-metal cylinder around the outer dewar may also be used to decrease fringing fields on field-sensitive photomultipliers in NaI counters. These shields were cut and cold-rolled without welding the seam and without annealing.

III.3.: Leads

Magnet Leads

Superconducting magnet leads should be carefully designed to minimize heat leaks into the helium bath. For large magnets, leads made of copper refrigeration tubing, with the bath boiloff vented through the tube, and with superconducting copper coated wire soldered to the lower half, seem to work reasonably well. For 100 amp. or less, 1/4" dia. will do, while for much larger currents 3/8" dia. is required. These leads represent a brute force approach to the problem, however, and considerable improvement should be possible. The use of large horizontal copper fins soldered to alternate leads and interleaved with styrofoam blocks offers some hope of more efficient gas cooling of the leads. Stainless steel copper plated leads also may be an improvement. We have used 1/4" dia. x .020" wall stainless tubing with a .005" copper plate to carry 30 amps. with some improvement over 1/8" dia. refrigeration tubing; in that case the leads

were in a pumped helium bath so gas cooling was small. The presence of the leads raised the bath pressure from 60 microns to 500 microns, and little change was noticed with current flowing, so the copper layer was undoubtedly still too thick.

For 15 amp. or less (in a 1° He bath) we have used the following leads: top of cryostat to top of styrofoam shielding, two strands #20 copper wire; thermal anchor; one strand #20 wire to maximum liquid helium level; thermal anchor; one foot of double strands of #28 copper wire; thermal anchor; and one strand #28 copper plus two strands Nb-Ti wire to the magnet. The thermal anchors were brass spools coated with GE #7031 varnish and wrapped with the wire to be anchored, which was then potted in epoxy or varnish. If Formvar insulated wire is used, care must be taken not to disturb the wire while the varnish is setting, since the solvent of the varnish dissolves Formvar. The brass spools were soldered to horizontal copper fins attached to the central pumping tube of the apparatus. These leads showed thermal runaway at 15 amps. but at 12 amps. they permitted the bath to be pumped as low as 70 microns.

RF Leads

The primary consideration in constructing rf leads is impedance matching. The major impedance is usually capacitive and can be controlled by varying the ratio of inner and outer lead size, assuming coaxial construction. Leads made from 3/8" dia. x .012" wall outer tube and 1/8" dia. x .010" wall inner tube (stainless steel), spaced with nylon triangles, have about 50 ohms impedance near 100 MHz per four feet of length. Smaller combinations of diameters can also be used. The leads may go down the central pumping tube although ours were outside with their own radiation traps. Ideally one would have a tank circuit for tuning the leads to the frequency range in use, although power input is not usually a problem in NMR/ON experiments, since only small heating rates can be tolerated. Use of a pickup coil and monitoring of the power in the input coils is essential to detect coil resonances and power losses in the leads.

Detector Leads

In designing detector leads one wishes to minimize stray capacitance which attenuates the pulses produced by the detector. Hence the leads should be as thin as possible and far away from grounded metal parts. Since thermal anchoring is inconsistent with these requirements, they should also be made of a poorly thermal-conducting material. Constantin or Manganin may be used, but I have found .002" dia. stainless steel to be quite workable. The leads are streched tightly down the center of the lead tube (the central pumping tube is best) and anchored at the radiation baffle in Kovar-glass feedthroughs. The leads themselves will have about 5 pf. capacitance and the seal (1. cm. dia.) another 5 pf. The top vacuum seal adds about 5 pf. more and if a BNC connector is used to attach the pre-amp it will add 3--4 pf. so the total will be about 18 pf. not counting the connection from the radiation baffle to the detector. In this part of the apparatus #50 copper wire enclosed in mylar tape works well.

Thermometer, Heater, Misc. Leads

For leads in which low resistance is desirable but current capacity, and reactance are unimportant, fine Formvar insulated copper is useful. The leads can be brought down a small stainless steel side tube and thermally anchored by wrapping on a spool with GE varnish or Apiezon grease as contact agent. It is helpful to make the vacuum feedthroughs at the top removable by means of a Rad Lab or similar fitting for easy replacement of seals or wires. If good electrical isolation is important, GE varnish should not be used because of its effect on Formvar insulation; much time can be wasted with high-resistance short circuits. For a constant but somewhat larger resistance, Manganin wire can be used, in sizes in the #30--#40 range.

III.4.: Cooling the Apparatus

Liquid Helium Transfer

Transfer of liquid helium is sometning of an art which has no doubt reached its peak at laboratories where helium is a scarcer commodity than it is at Berkeley. Nevertheless, transferring has posed one of the major problems in the operation of the large CMN cryostats and so I believe a

few words on the subject are in order here. Several features of cryostat design are responsible for this situation: the use of metal dewars, the use of superconducting magnets, the volume of the salt pills, and simply the size of the whole system. These cryostats hold about 25 l. of liquid when filled and a large percentage of the liquid consumption on initial cooldown goes to cool the apparatus from 77° to 4.2° K.

Two considerations seem predominant in helium transfer to these cryostats: removal of liquid nitrogen and gas cooling. The liquid nitrogen used for precooling the dewars is usually removed by blowing out through a tube extending to the bottom of the dewar. The heat of fusion is larger than the heat of vaporization of liquid helium so it is of prime importance to remove all the LN before starting helium transfer. Secondarily, LN frozen into the coils of superconducting magnets may interfere with their operation. Three steps will insure removal of LN: 1) After liquid blowout appears to cease, shut off the blowout pressure and wait 5 minutes. This will allow LN in the magnet coils and upper parts of the dewar to run to the bottom. 2) When no more liquid comes out on reapplication of pressure, blow helium gas down the LN blowout tube for a few minutes. This will evaporate remaining liquid without seriously warming the dewar. 3) Connect the dewar to the helium bath pumpline and evacuate it. If the LN is really gone, the pressure will fall rapidly to about 100 microns. Otherwise the pressure will fall to 500--1000 microns and stop. In the latter event the LN will have frozen and helium can be transferred if not too much frozen nitrogen is in the dewar bottom.

As for gas cooling, the necessity of using the large heat capacity of the cold helium gas rather than the rather small latent heat of the liquid to cool the dewar into which helium is being transferred is well known. To do this, it is necessary to force the liquid to come out as near as possible to the bottom of the dewar by using a transfer tube extension.

Observing these precautions and not allowing any part of the apparatus to get too far out of thermal equilibrium during transfer should allow filling of both dewars from LN temperature in as little as 1-1/2 hrs. with

as little as 55 l. of liquid helium. After 24 hrs., refilling takes about 30 l. and 1/2 hr.

Exchange Gas

We have used both ^{3}He and ^{4}He for exchange gas. The former seems to pump out more readily, but it is of course more expensive. A pressure of 30 microns seems to be a sufficient amount. We have had no difficulty with Formvar insulation, spaghetti tubing or other plastics in the experimental chamber causing difficult pumpout of the exchange gas; however, long lead tubes with a common vacuum do seem to cause such difficulties. In any case, in a large apparatus with a 10 mdeg. heat shield, most of the final pumping is cryopumping by the shield on demagnetization. There is no doubt that when exchange gas is used, residual gas conduction is a major heat leak and so it is imperative to have a complete, well isolated heat shield around the main cooling salt pill, the heat link, and the sample itself if feasible.

Exchange gas may be eliminated by using a mechanical or superconducting heat switch or a liquid helium column to precool the salt and remove the heat of magnetization. Experiments in this laboratory by J.A.Barclay and J.E.Templeton have indicated that these techniques are difficult and require considerable effort in time, equipment, and expertise to apply sucessfully.

Magnetic Cooling

The following schedule has proven to be efficient for carrying out the cooling cycle, starting with equilibrium at 4.2° K.: Start bath pumpdown, keeping pumpline pressure about 1000 microns. Start magnetization. The magnet should charge in 25--35 min.; pumpdown of the 1° bath seems to require about 45 min. Exchange gas pressure may need adjustment during pumpdown. When the bath is at minimum pressure, leave the magnet on and exchange gas in for 1/2--1 hr. Exchange gas pumpout to gauge pressure of 5×10^{-6} torr. takes about 45 min. if the pump is in good order. Experiments have shown that as the time taken for the demagnetization process is increased from 15 min. to 45 min., the temperature reached decreases; but beyond 45 min. no further improvement is seen. An improvement in the

temperature reached was obtained by turning the polarizing field on before demagnetizing. Warmup rates are typically of order 1 mdeg./hr. in the absence of extra heating., with final warmup occurring when the 10 mdeg. heat shield warms and releases cryopumped exchange gas. Two useful improvements to the existing apparatus might be suggested: addition of resistance thermometers to the salt pill, allowing its temperature to be monitored during transfer of liquid helium and magnetization; and a permanent LHe level detector in the 1° bath. The above remarks apply specifically to the apparatus described in Chap. VI, but are generally applicable to any large magnetic cooling apparatus of similar design.

Acknowledgements

It is usual to find at the end of a thesis a long list of people without whose help its production would have been difficult or impossible. This work is no exception, in that a large number of people have contributed either directly or indirectly toward making it possible. It is a privilege to recognize some of them here:

First, I wish to thank my research director, Prof. D.A.Shirley, for his guidance and support through the past few years. I also acknowledge the guidance of Prof. E.Matthias, especially during 1966-67.

I would like to thank Dr. J.E.Templeton, who stimulated interest in the beta decay work, for many suggestions and discussions. Dr. R.H.Pehl offered valuable advice and assistance in obtaining workable beta counters, and I owe thanks to him and to his assistants in the Semiconductor Development Group.

Many people gave technical assistance and advice to these projects. I especially wish to mention Mrs. Winifred Heppler, who helped with the chemistry and source preparation, and who maintained a steady supply of coffee; and Mrs. G.R.Bolz, who assisted with radiochemistry and monitoring. Mr. D.N.Voronin built many parts for the apparatus described herein, and offered numerous suggestions concerning apparatus design and construction. Mrs. Penny A. Fink wrote the data acquisition program used to collect some of the ^{119}Sb data, and also the first-stage data analysis program for the beta decay work.

Of considerable importance to any laboratory is the working environment which is provided by one's colleagues. I suppose no one ever leaves Berkeley without a certain regret, and in my case this is in large

measure regret at leaving the congenial intellectual and social atmosphere of the RadLab. Many of my fellow students and post-doctoral assistants have contributed to this feeling, and I thank them not only for scientific advice and assistance, but for their friendship. I would especially like to mention Drs. J.J.Huntzicker and J.A.Barclay, who handed on some of the folklore of low temperature work; my office-mate, Arthur Soinski, who has saved me many trips to the storeroom; and my sometime-coworkers, Frederick Bacon and Jim Holliday, who have both shown humor in the face of disaster. I also have enjoyed and profited from my association with Dr. Erwin Klein, and I hope to continue it in the future.

Finally, I would like to thank my wife, Mary, for her patience with my often bizarre working hours in the face of her own full schedule of maintaining a household, raising our son, and acquiring a PhD.

This work was supported by the U.S.Atomic Energy Commission. I also acknowledge the generous personal support of the National Science Foundation graduate fellowship program over the last few years.

TECHNICAL INFORMATION DIVISION
LAWRENCE RADIATION LABORATORY
UNIVERSITY OF CALIFORNIA
BERKELEY, CALIFORNIA 94720